

Reza Eslami

**A NOVEL MICRO-MECHANICAL MODEL
FOR PREDICTION OF MULTIAXIAL
HIGH CYCLE FATIGUE AT SMALL SCALES**

SCHRIFTENREIHE DES INSTITUTS
FÜR ANGEWANDTE MATERIALIEN

BAND 64



Scientific
Publishing

Reza Eslami

**A novel micro-mechanical model for prediction
of multiaxial high cycle fatigue at small scales**

**Schriftenreihe
des Instituts für Angewandte Materialien
*Band 64***

Karlsruher Institut für Technologie (KIT)
Institut für Angewandte Materialien (IAM)

Eine Übersicht aller bisher in dieser Schriftenreihe erschienenen Bände
finden Sie am Ende des Buches.

A novel micro-mechanical model for prediction of multiaxial high cycle fatigue at small scales

by
Reza Eslami

Dissertation, Karlsruher Institut für Technologie (KIT)
Fakultät für Maschinenbau
Tag der mündlichen Prüfung: 24. Mai 2016

Impressum



Karlsruher Institut für Technologie (KIT)
KIT Scientific Publishing
Straße am Forum 2
D-76131 Karlsruhe

KIT Scientific Publishing is a registered trademark of Karlsruhe
Institute of Technology. Reprint using the book cover is not allowed.

www.ksp.kit.edu



*This document – excluding the cover, pictures and graphs – is licensed
under the Creative Commons Attribution-Share Alike 4.0 International License
(CC BY-SA 4.0): <https://creativecommons.org/licenses/by-sa/4.0/deed.en>*



*The cover page is licensed under the Creative Commons
Attribution-No Derivatives 4.0 International License (CC BY-ND 4.0):
<https://creativecommons.org/licenses/by-nd/4.0/deed.en>*

Print on Demand 2017 – Gedruckt auf FSC-zertifiziertem Papier

ISSN 2192-9963

ISBN 978-3-7315-0583-9

DOI 10.5445/KSP/1000059741

A novel micro-mechanical model for prediction of multiaxial high cycle fatigue at small scales

Zur Erlangung des akademischen Grades

Doktor der Ingenieurwissenschaften

der Fakultät für Maschinenbau

Karlsruher Institut für Technologie (KIT)

genehmigte

Dissertation

von

Reza Eslami

Tag der mündlichen Prüfung: 24.05.2016

Hauptreferent: Prof. Dr. Oliver Kraft

Korreferent: Prof. Dr. Chris Eberl

Acknowledgement

The following dissertation has been prepared in Institute for Applied Materials (IAM) of Karlsruhe Institute of Technology (KIT); an excellent place for scientific researches with expert and cooperative colleagues.

Hereby I would like to acknowledge everyone, whose support, encouragement, and remarks have helped me to finish this work.

I would like to express my sincere gratitude to my doctoral supervisor and the head of IAM, Prof. Dr. Oliver Kraft, for giving me the opportunity to work on this interesting topic at IAM, and also for his excellent scientific guidance and support throughout the entire dissertation work. The guiding discussions with him gave me the feeling of freedom and encouragement during the work.

I would like also to express my greatest thanks to my supervisor and head of the probabilistic group at IAM, Dr. Heinz Riesch-Oppermann, for his support and precious hints during the work. His expertise and provision of ZERBERUS code were very helpful specially in probabilistic considerations and parameter study in this dissertation. He reviewed the manuscripts of dissertation and papers very precisely and patiently, and gave me constructive comments on them, which I appreciate sincerely.

I would like to acknowledge Prof. Dr. Chris Eberl and his team, in particular Thomas Straub, for collaboration, performing the fatigue tests, providing with the experimental data, and fruitful discussions. Furthermore, I acknowledge Daniela Exner and Moritz Wenk for performing the EBSD measurements, SEM microscopy, and FIB analyses.

Special thanks to previous and current PhD students and colleagues of IAM for a pleasant working atmosphere and cooperation.

Last but not least I would like to thank my family, for their support during whole of my life.

Abstract

The grain microstructure and damage mechanisms at the grain level are the key factors that influence fatigue of metals at small scales. This is addressed in this thesis by establishing a new micro-mechanical model for prediction of multiaxial high cycle fatigue (HCF) at a length scale of 5-100 μm . The HCF model considers elasto-plastic behavior of metals at the grain level and micro-structural parameters, specifically the grain size and the grain orientation. The accumulated plastic shear strain is postulated as the main contributor to the initiation of micro-cracks in the grains; if it is bounded in the limits defined by the elastic shakedown theorem, then no HCF failure is expected in the grains. The HCF model can be applied either as a deterministic failure criterion for individual grains, or as a failure function in probabilistic studies on aggregates of grains, if the variables are given by stochastic distributions. This is illustrated in a parameter study beside the sensitivity analysis of the failure function with respect to different variables. For model verification, the predicted results of the failure function are compared with the observed micro-damage in individual grains of nickel micro-samples. For that the grain size and the grain orientation are measured on the surface of the samples by Electron Backscatter Diffraction (EBSD) analysis, as the main input variables of the failure function. By comparison between prediction results and observed HCF micro-damage, a classification scheme is obtained for all analyzed individual grains. The classification results show that the overall predictive power of the HCF model is fairly good. Nevertheless, some misclassifications occur as some grains are damaged, which are predicted to be safe. Post-fatigue investigations on individual grains reveal in some cases the reasons for those misclassifications. Particularly at the beginning of the micro-damage evolution, the failure function presents a very good prediction power, however by occurrence of more and severe micro-damage (at higher stress amplitudes and higher cycle numbers), the mechanical interaction between the neighboring grains increases, leading to the reduction of the prediction power. The HCF model can be applied for fatigue prediction in real small scale applications, e.g. micro electro mechanical system (MEMS), thin wires, or thin films.

Kurzzusammenfassung

Die Kornmikrostruktur und Schädigungsmechanismen auf der Kornebene sind die Schlüsselfaktoren, welche die Ermüdung der Metalle in kleinen Größenskalen beeinflussen. Dies ist in dieser Dissertation adressiert worden, indem ein neues mikromechanisches Modell zur Vorhersage der mehrachsigen hochzyklischen Ermüdung (HCF) in einer Längenskala von 5 μm bis 100 μm entwickelt worden ist. Das HCF-Modell basiert auf elasto-plastischem Verhalten der Metalle auf der Kornebene und enthält Parameter der Mikrostruktur, insbesondere die Korngröße und Kornorientierung. Die akkumulierte plastische Schubdehnung in jedem Korn ist als Hauptbeitrag zur Initiierung der Mikrorisse postuliert worden; wenn sie durch Grenzwerte definiert vom „elastic shake-down“ Theorem begrenzt ist, so wird kein HCF-Versagen in dem Korn erwartet. Das HCF-Modell kann entweder als ein deterministisches Versagenskriterium für die einzelnen Körner verwendet werden, oder als eine Versagensfunktion für die probabilistischen Betrachtungen für die Kornaggregate, wenn die Variable durch stochastische Verteilungen gegeben sind. Dies ist in einer Parameterstudie beschrieben worden, sowie die Sensitivitätsanalyse der Versagensfunktion zu unterschiedlichen Variablen. Zur Verifizierung des Modells sind die Ergebnisse aus der theoretischen Versagensvorhersage mit der beobachteten Mikroschädigung in einzelnen Körnern der Ni-Mikroproben verglichen worden. Dafür sind die Korngröße und Kornorientierung – als die Haupteingangsvariable der Versagensfunktion – auf der Probenoberfläche mittels der EBSD-Methode gemessen worden. Beim Vergleich der vorhergesagten Ergebnisse mit der beobachteten HCF-Mikroschädigung ist ein Klassifizierungsschema für alle einzelnen analysierten Körner erhalten worden. Die Klassifizierungsergebnisse zeigen, dass die allgemeine Vorhersagekraft des HCF-Modells recht gut ist. Trotzdem treten einige Missklassifizierungen auf, bei denen Körner geschädigt sind, welche als sichere Körner erwartet wurden. Die nachträglichen Untersuchungen an individuellen Körnern decken in einigen Fällen die Ursachen für solche Missklassifizierungen auf. Besonders für den Anfangsbereich der Schädigungsentwicklung zeigt die Versagensfunktion eine sehr gute Vorhersagekraft. Aber beim Auftreten von zunehmender und starker Mikroschädigung (bei höheren Spannungsamplituden und höheren Zyklenzahlen),

erhöht sich die mechanische Wechselwirkung zwischen den Nachbarkörnern, und setzt die Vorhersagegenauigkeit herab. Das HCF-Modell kann für die Ermüdungsvorhersage in den praktischen Applikationen in kleinen Größenskalen, wie z.B. mikro-elektro-mechanische Systemen (MEMS), Dünndrahtbonds oder Dünnschichten verwendet werden.

Table of contents

Acknowledgement	I
Abstract	III
Kurzzusammenfassung	V
Symbols and abbreviations.....	IX
1 Introduction	1
2 Fatigue in metal parts	7
2.1 Damage evolution in cyclic loading	8
2.2 Macroscopic, microscopic, and mesoscopic scales of material description	10
2.3 Representative volume element (RVE).....	11
2.4 Multiaxial HCF criteria	13
3 Micro-mechanical model for prediction of HCF.....	19
3.1 Plasticity theory of metal grains	20
3.2 Accumulated plastic shear strain in a slip system	26
3.3 Elastic shakedown	28
3.4 Micro-mechanical model for prediction of HCF at small scales	32
4 Parameter study	37
4.1 Deterministic study of parameters.....	37
4.2 Probabilistic study of parameters and corresponding numerical tools	42
5 HCF experiments with micro-samples.....	47
5.1 Custom-built test setup	47
5.2 Geometry design of micro-samples	50
5.3 Material selection and preparation of micro-samples	56

5.4	Measurement of grain size and grain orientation with EBSD.....	57
5.5	Analysis of surface damage.....	60
5.6	Performing of HCF experiments under bending load.....	63
6	Comparison of theoretical and experimental results.....	67
6.1	Results of sample No. Ni-107.....	70
6.1.1	Correct prediction of no damage.....	71
6.1.2	Incorrect prediction of damage.....	72
6.1.3	Correct prediction of damage.....	73
6.1.4	Incorrect prediction of no damage.....	74
6.1.5	Summary of results for sample No. Ni-107.....	76
6.2	Results of sample No. Ni-106.....	77
6.3	Results of sample No. Ni-105.....	80
6.4	Results of sample No. Ni-108.....	83
7	Summary.....	89
8	References.....	93
	Appendix A1: Euler-angles and rotation matrices.....	107
	Appendix A2: tensile triangle method.....	111

Symbols and abbreviations

σ_b	Bending stress
σ_t	Torsion stress
f_{-1}	Endurance limit in fully reversed bending
t_{-1}	Endurance limit in fully reversed torsion
J_2	Second invariant of the stress deviator tensor
σ_H	Hydrostatic stress
\underline{C}	Vector of shear stress acting on a plane
\underline{N}	Vector of normal stress acting on a plane
φ, θ, ψ	Spatial angles for description of orientation of a plane or grain
τ	Shear stress
Σ_H	Macroscopic hydrostatic stress
$\underline{\underline{\Sigma}}$	Macroscopic tensor (second-rank) of stresses
$\underline{\underline{E}}$	Macroscopic tensor (second-rank) of strains
$\underline{\underline{C}}_4$	Macroscopic tensor (fourth-rank) of stiffness
$\underline{\underline{L}}_4$	Macroscopic tensor (fourth-rank) of compliance
δ	Kronecker delta
$\underline{\underline{\sigma}}$	Mesoscopic tensor (second-rank) of stresses
$\underline{\underline{\varepsilon}}$	Mesoscopic tensor (second-rank) of strains

$\underline{\underline{\varepsilon}}^e$	Mesoscopic tensor (second-rank) of elastic strains
$\underline{\underline{\varepsilon}}^p$	Mesoscopic tensor (second-rank) of plastic strains
$\underline{\underline{C}}_4$	Mesoscopic tensor (fourth-rank) of stiffness
$\underline{\underline{l}}_4$	Mesoscopic tensor (fourth-rank) of compliance
\underline{m}	Vector of slip direction
\underline{n}	Normal vector to the slip plane
$\underline{\gamma}^p$	Vector of plastic shear strain along a slip direction
\underline{T}	Vector of macroscopic resolved shear stress
$\underline{\tau}$	Vector of mesoscopic resolved shear stress
τ_y	Yield stress
Γ	Accumulated plastic shear strain along a slip direction
Γ_c	Critical limit of accumulated plastic shear strain
d	Grain size

1 Introduction

Fatigue is the main failure mode of numerous components undergoing mechanical and thermal cyclic loadings during their life time. A lot of work has been done to understand the fatigue mechanism, and to establish criteria for prediction of fatigue life and the endurance limit. In this work, the focus is on multiaxial high cycle fatigue (HCF) of metal micro-components to understand their lifetime behavior in real applications, e.g. micro electro mechanical system (MEMS). HCF is characterized by small strain amplitudes and higher number of load cycles (between 10^6 and 10^8 cycles). In this regime, there are generally no irreversible deformations (i.e. plastic or viscous) at the macroscopic level, and the behavior of the bulk material is elastic. However, at the mesoscopic level, irreversible plastic strains occur in some unfavorably oriented grains. Such plastic strains can localize in persistent slip bands and lead consequently to initiation of micro-cracks [1-2]¹.

Initially, classical fatigue criteria and related experimental data were applicable mostly for uniaxial and simple loading conditions. However most real engineering applications are associated with multiaxial and complex loading conditions. Furthermore, many fatigue criteria (for prediction of the fatigue life or the endurance limit) considered just parameters resulting from experiments and calculations done at the macroscopic scale. However, fatigue damage initiates in the grains due to dislocation motions along slip systems. Therefore, fatigue mechanisms at mesoscopic scale, related heterogeneities, and size effects should be considered too [3-4].

To overcome the mentioned limitations of classical fatigue approaches, Dang Van [5-7] proposed for the first time a multiaxial HCF criterion from a model of physical processes at the mesoscopic scale and based on the elastic shakedown theorem. He considered the local mechanical parameters and fatigue damage initiation in the grains. According to his criterion no fatigue rupture will occur at a point of the structure, if the response of the material at all scales is

¹ In this dissertation the citation of references is given usually at the end of the sentences or paragraphs, which are written based on the work referred to (literally or with regard to content).

elastic shakedown. Fatigue cracks initiate usually in less resistant grains with their easy slip system aligned on the direction of the maximum shear stress.

For application of Dang Van's criterion at the grain scale, mesoscopic shear stresses should be known, which are not accessible conveniently. Papadopoulos proposed a similar criterion as Dang Van's theory relating mesoscopic and macroscopic mechanical fields. According to Papadopoulos, elastic shakedown is reached, if the accumulated plastic shear strain in each slip system does not exceed a critical limit [3, 8-9]. The Papadopoulos criterion provides satisfactory results in prediction of HCF fracture at macroscopic scale, but it can not predict the initiation of HCF cracks in individual grains, since it considers only the aggregates of grains with homogenous material and stress parameters.

As mentioned before, HCF damage is controlled by mechanisms at the grain level and mesoscopic parameters are governing the initiation of fatigue cracks. Therefore, in small scale applications, e.g. for MEMS, the components include just a few grains in each direction and initiation of micro-cracks in one or some grains can lead to the failure of the whole component. In such cases, each grain should be evaluated individually, and the microstructure and material parameters of each grain need to be considered for the fatigue criterion. The main parameters for describing the microstructure are grain size and grain orientation, which affect the fatigue strength as illustrated in the next sections.

The early results corresponding to the effect of grain size on the fatigue life are covered in the paper of Backofen and Thompson [10]. They studied the S-N diagram of brass, copper, and aluminum with different grain sizes at constant stress amplitude over a lifetime of 10^4 to 10^7 cycles. In brass the fatigue life was found to be proportional to the inverse of the square root of the grain size. They did not find a significant dependency of fatigue life on grain size for copper and aluminum. The difference between the behavior of brass, copper, and aluminum was attributed to the different slip characters of these materials.

Later on, Lukas and Kunz studied the grain size effect on the cyclic stress-strain response and fatigue of polycrystalline copper in HCF. They concluded that the total strain fatigue limit and the stress fatigue limit are almost grain size independent, while the plastic strain fatigue limit depends strongly on the grain size [11]. Thus the grain size can affect the plastic behavior and consequently the fatigue damage mechanism inside the grain. Hence, the grain size is included

in the numerical model, presented in this work, as a main parameter of the microstructure.

Hanlon *et al.* studied the grain size effect on the fatigue life in different material scales e.g. micro-crystalline (10 μm), ultra-fine crystalline (300 nm), and nano-crystalline (20-40 nm) nickel. It was found that the grain refinement generally leads to an increase of fatigue life under stress-controlled loading [12]. Mughrabi concluded similarly that in HCF region the total strain fatigue life for ultrafine-grained (850 nm) aluminum samples is higher than for the samples with conventional grain size (170 μm) [2].

The above mentioned work and similar approaches address only the empirical relationship between the fatigue life and the grain size but do not provide a physical model for it. The aim of the present work is to set up a physical model and to achieve experimental verification regarding the influence of the grain size on the fatigue behavior.

Weng developed a micromechanics-based theory for the effect of the grain size on the yield stress of polycrystalline metals based on the Hall-Petch equation [13]. He implemented a mixed hardening rule incorporating both isotropic and kinematic components and considering multiple slip. Weng's theory is applied in this work for developing the micro-mechanical model illustrated in the next chapters.

The next main parameter for describing the microstructure is the grain orientation, since the resolved shear stress along the slip bands is dependent on the grain orientation. There has not been much work to investigate the effects of the grain orientation on the fatigue life. Most of the work verified the effect of grain orientation on dislocation patterns in grains and slip bands [2, 15-19]. Morrissey *et al.* implemented a 2D crystal plasticity formulation for Ti-6Al-4V into the FE codes [16, 100]. They used a planar triple slip idealization to model the prismatic crystallographic slip behavior at room temperature under HCF conditions. In order to monitor the plastic strains over the cycles, this plasticity formulation should be calculated over all cycles which requires a long computation time. Beside that, the formulation implements the local mechanical parameters, e.g. shear stress and strain rate in the slip systems, which are not accessible conveniently.

This short summary on the previous work regarding the HCF criteria and related limitations in different material scales reveals that the current fatigue

criteria do not present a numerical model applicable at small scales, which considers the influence of microstructural parameters on the fatigue strength. Previous results and the mentioned limitations provided the motivation for this dissertation to develop an appropriate HCF model for prediction of the HCF failure in individual grains that considers the influence of microstructural parameters, e.g. grain size and grain orientation, on the fatigue strength.

In the first step, the principles of the HCF mechanisms and damage evolution in metal parts will be illustrated in chapter 2, while different material scales are considered and some well-known HCF criteria are reviewed too.

As a next step, the new HCF micro-mechanical model will be developed in chapter 3 after a short introduction in the plasticity theory of the metal grains. The elaborated HCF model uses the plastic shear strain accumulated in the grains as a damage variable to predict the HCF failure. Therefore two main aspects in this chapter are: 1) the evaluation of the accumulated plastic shear strain during load cycling, and 2) application of a restraint on the accumulated plastic shear strain to avoid initiation of micro-cracks in individual grains. Concerning these two aspects the elastic shakedown theorem and previous work of Dang Van and Papadopoulos in this field will be illustrated. At the end of this chapter a failure function will be introduced – based on the HCF micro-mechanical model – to describe the failure behavior of the grains in terms of different physical and geometrical variables.

In chapter 4, the sensitivity of the failure function with respect to different parameters will be analyzed. Then by means of some examples, the application of the failure function for deterministic description of the HCF failure in individual grains will be shown. After that a probabilistic approach will be introduced for assessment of HCF probability, if the stochastic distributions of parameters are given for an aggregate of the grains.

In chapter 5, the approach for HCF experiments on micro-samples is illustrated. In this regard, the test setup and design of micro-samples are discussed. At the end of this chapter, the evolution of micro-damage on the surface of the micro-samples due to HCF experiments is presented, and suitable methods for inspection of those surface damages are illustrated.

In chapter 6, the prediction results of the failure function are compared with the observed surface damage during HCF experiments. Depending on agreements or disagreements between theoretical and experimental data for each

grain, the results are classified in 4 categories. To find the reasons of misclassifications, some grains are investigated in further analyses.

In the last chapter, the summary of results gained in this dissertation is discussed and for future work an outlook is presented.

2 Fatigue in metal parts

Fatigue refers to the damage and failure of the components under cyclic loading with stresses below the static ultimate strength of the bulk material. The majority of failures in machinery and structural components are attributed to fatigue processes, which occur in different forms as: mechanical fatigue, creep-fatigue, corrosion fatigue, rolling contact fatigue, etc. [20]². Due to the impacts on the endurance life, economics, and safety aspects, fatigue has been one of the most important topics in the area of material researches in the last 150 years and still fascinating as ever, specially with increasing importance of the new materials, small-scaling and miniaturization of the components (e.g. MEMS), and requirements on longer life times [2, 21]. As an example, fatigue of railway axles was one of the main technical problems that prompted the early fatigue studies of metallic materials, since it is related to the safety and any failure includes the risk of catastrophic derailment. Beside the classical approaches that define the minimum strength requirements for axles, there has been increasing demand for the reliability assessment of these components specially considering the safe life inspection intervals and the high speed train applications. Therefore it has been one of the most recent fields of fatigue studies [22-24].

Pioneering systematic investigations on fatigue failure were performed by Wöhler between 1852 and 1869, who demonstrated fatigue life (number of load cycles before failure) in dependency on stress amplitude for so-called S-N curves. Since these curves were established just for simple uniaxial load conditions, other methods were needed to predict fatigue life in more complicated loading situations specially to consider the influence of stress ratios and mean stresses. In 1874, Gerber began developing methods for fatigue life calculations based on mean stresses, which was continued later by Goodwin in 1899. Characterization of S-N curves of metals with empirical laws was proposed by Basquin in 1910, who illustrated the log-log plot of S-N curves in a linear relationship [20, 25-26].

² The introduction and history, given on this and next page, about fatigue in metal parts, are mainly based on the reference [20]. Readers are referred to this reference for some more details on this topic.

Bauschinger recognized variation of the yield stress due to the cyclic loading in 1886, and perceived the cycling strain hardening and softening. In 1900, Ewing and Humfrey documented the cyclic damage on the surface of iron specimens due to the formation of slip bands in the grains. Those slip bands led to the initiation of cracks and consequently failure of the specimens. In 1954, Coffin and Manson mentioned plastic strains as the root-cause for cyclic damage, and established an empirical relationship between fatigue life and the amplitude of the plastic strain [27-28]. However, the mathematical framework for quantitative modeling of fatigue failure was still missing. For the first time Paris, Gomez, and Anderson established in 1961 the relationship between the increment of fatigue crack propagation (per load cycle) and the range of the stress intensity factor during constant amplitude cyclic loading [20].

The effects of various mechanical, microstructural and environmental factors on cyclic deformation, crack initiation, and crack growth in a broad spectrum of engineering materials have been the topics of many researches in the past four decades. In this period, substantial progress has been made in understanding of the cyclic deformation and crack initiation mechanisms, also related to developments in optical and electron microscopy. Significant contribution to these progresses was made by studies which identified the key microscopic features of fatigue crack initiation. In 1956, Thompson, Wadsworth and Louat demonstrated that in metals the slip bands, along which the plastic deformation was concentrated, persistently reappeared at the same locations during cycling loading and caused some markings on the surface, which were named as persistent slip bands (PSBs) [20].

2.1 Damage evolution in cyclic loading

Fatigue cracks in metals originate at internal or external surfaces, while the latter one is more common. There are regions of local inhomogeneity in the material that during cyclic loading result in local softening or surface flaws that cause local stress concentration. These factors can lead to localized plastic deformation, which under the action of cyclic stress (or strain) can produce surface markings, denoted as extrusions and intrusions (Fig. 2.1). While fatigue crack initiation can be caused by plastic strain inhomogeneities related to the

material cyclic strain behavior, it can also occur through other origins of plastic strain inhomogeneity: e.g. presence of inclusions or second-phase particles within the material, or surface flaws. Even in materials that are made as uniform as possible the localized plastic deformations is heterogeneously distributed, often in the form of persistent slip bands (PSBs). The PSBs are often associated with surface crack initiation [29]³.

Continuing with cyclic deformation, the surface markings are enhanced and gradually a micro-crack will be nucleated on the surface at the interface between the protrusions and the surrounding material. This nucleation stage is named as stage I of the fatigue fracture. This stage is dictated by plastic deformation rather than fracture mechanisms. The initial micro-crack (fatigue fracture stage I) propagates inside the grain and along the PSB in a direction dictated by the plastic deformation and not normal to the principal stress axis. By reaching the grain boundary, the micro-crack must cross over into the next grain, where the slip systems may have other orientations. So the crack propagation can be slowed down or disrupted. Thereby the propagation of many micro-cracks is stopped, so that just a few micro-cracks, which have by chance a suitable propagation orientation, can grow further. With further growth of the micro-crack, the stress at the crack tip will become so high that even slip systems with a non-proper orientation will be activated. Hence the crack alters its direction and the propagation direction becomes normal to the principal tensile stress axis. So stage II of the fatigue fracture begins, while the dominant crack behaves as a macro-crack and grows stably at a slow rate. When the macro-crack has grown to an extent that the unfractured section of the material cannot withstand the maximum applied tensile stress, then the final fracture of the material (fatigue fracture stage III) is forced in a rapid and instable manner through the remaining section [29-30].

³ Section 2.1 is written mainly based on references [29, 30]. Readers are referred to these references for some more details on this topic.

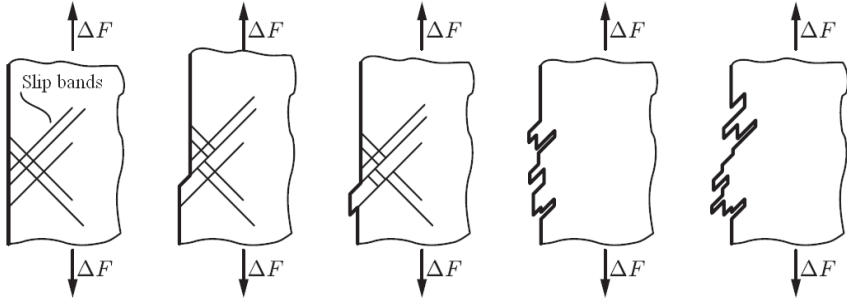


Fig. 2.1. Formation of intrusions and extrusions due to the cyclic plastic deformation along slip bands. The number of load cycles increases from the left figure to the right one [30].

The nucleation of micro-cracks and the growth rate of the macro-crack are strongly influenced by a wide range of mechanical, microstructural and environmental factors; e.g. stress amplitude, grain size, and corrosive environment. Different design approaches for prediction of fatigue life rest on how the crack initiation and the crack propagation stages of fatigue are considered and modeled quantitatively [20]. On the other hand, the fatigue behavior of materials can be investigated at different scales. For that the material behavior needs to be described at the related scale, e.g. macroscopic or mesoscopic scale, and a link between physical parameters at different scales should be established. In the next section three main scales for material description will be discussed, which help later in discussing different fatigue criteria.

2.2 Macroscopic, microscopic, and mesoscopic scales of material description

The mechanical state of a body considered as a continuous medium, is usually described with the help of macroscopic quantities (i.e. stresses and strains). The macroscopic scale is mainly used in engineering applications and determines the stresses and strains in any point of the body with the aim of analytical or numerical methods (e.g. finite element simulations). A number of fatigue criteria

have been proposed at the macroscopic scale; however, most of them provide non-satisfactory results under multiaxial non-proportional cyclic loading. Fatigue of materials can be assessed also at microscopic scale, which is the scale of dislocations, applied mainly by physicists or metallurgists. Fatigue investigations at microscopic scale correspond to considerations of dislocations and formation of PSBs [9, 14, 31, 52, 102]. Studies at the microscopic scale are essential for understanding of fatigue mechanisms related to fatigue crack initiation. However, microscopic scale approaches can not be applied in engineering design of components against fatigue failure. Finally, fatigue of materials can be explored from an intermediate scale between the microscopic and macroscopic scales named as mesoscopic scale. Within this framework the stresses and strains at the grain level, namely mesostresses and mesostrains, are taken into account. Since the mesoscopic scale quantities are not directly accessible, they must be linked to usual macroscopic quantities which are accessible in engineering applications either by calculations (e.g. FE simulations) or measurements (e.g. with strain gauges). As it will be shown in chapter 3, the passage from mesoscopic to macroscopic quantities is possible by using micro-mechanics approaches and appropriate assumptions as applied by Lin-Taylor, Sachs, or Kröner [9, 32-34]. In this regard, the concept of the representative volume element (RVE) is very helpful, which will be described in the next section.

2.3 Representative volume element (RVE)

The principal idea in micro-mechanics is to consider at least two different scales for the description of mechanical or physical relationships (Fig. 2.2). At the macroscopic scale a body is considered as a continuum mass. Looking into each point of the body at mesoscopic scale, it contains a volume of elements (e.g. grains, micro-cracks, or voids), which represents the microstructure of the material at that point. Based on the micro-mechanics approach the volume and its elements should satisfy the following properties [37]:

- a) It is assumed that the material inside the volume of elements is homogeneous at the macroscopic scale; however, heterogeneous at the mesoscopic scale, since the material parameters, size and orientation of grains are different. The

macroscopic stress Σ and strain E are constant (homogenous) at the point of consideration, but at the grain scale the mesoscopic stress σ and mesoscopic strain ε differ from one grain to the other one (Fig. 2.2).

- b) From a macroscopic point of view, the volume is so small, that the macroscopic stress gradients inside are negligible ($D \ll H, L$, see Fig. 2.2). In fact it represents the minimum size of the polycrystalline aggregate.
- c) On the other hand, the volume of elements is large enough, so that the dimensions of its elements are much smaller than the volume itself ($d \ll D$). Considering a polycrystalline aggregate of grains, the dimension d relates to the grain size. It implies that the volume contains many grains, and hence, is statistically representative.

Such a volume is denoted as representative volume element (RVE). It was applied for the first time by Hill and Hashin for modeling of heterogenic materials [35-36]. For materials used in usual engineering applications, e.g metals or ceramics, the dimension d is typically in the range of micrometer (as the size of the grain boundary or voids), while the dimension L is in the range of millimeter [37].

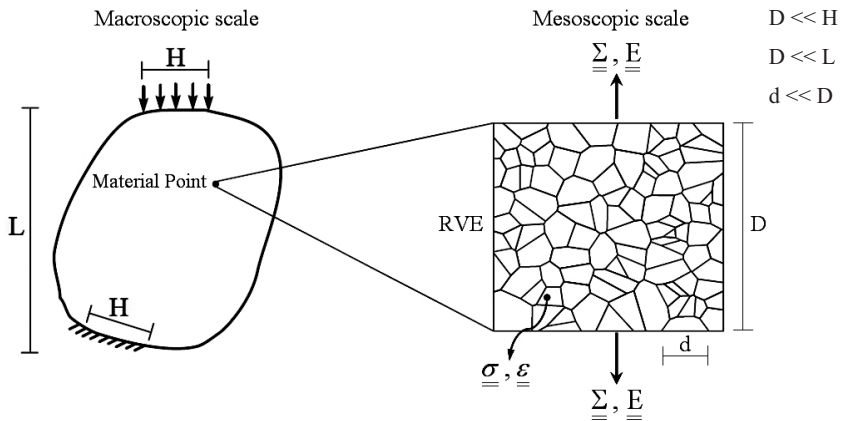


Fig. 2.2. Illustration of macroscopic and mesoscopic scales applied in micro-mechanics, with related dimensions and the concept of representative volume elements (RVE). Reference of the figure is [37], with some small modifications.

Since the mesoscopic stresses and strains inside the RVE are not directly accessible (comparing to the macroscopic ones), a link between macroscopic and mesoscopic quantities is needed, which will be described in chapter 3 with the aim of theoretical relationships.

2.4 Multiaxial HCF criteria

Results of uniaxial HCF experiments show that a number of metals possess an endurance limit (fatigue limit). If the uniaxial load oscillates in the range of the stress defined by the endurance limit, then the specimen can withstand a very high (theoretically infinite) number of load cycles, without development of any fatigue cracks [3].

Most of experimental data regarding the fatigue life of materials correspond to uniaxial loading with constant amplitude, e.g. tension-compression, rotational bending or torsion tests. However components in engineering applications undergo generally multiaxial loading, which are also frequently non-proportional. The cyclic stress-strain response under multiaxial loading, which depends on the loading path and the fatigue behavior of the materials, are complex. To generalize the endurance limit concept for multiaxial stress condition, the complex multiaxial loading needs to be reduced to an equivalent stress state, which can be compared with the experimental data of uniaxial fatigue experiments. Dealing with this matter, different multiaxial HCF criteria have been proposed, which predict if under the applied cyclic loading a fatigue crack occurs or not. The fatigue criteria are usually expressed as an inequality, which separates the stress space into two domains: the safe domain and the unsafe one. Satisfaction of this inequality implies that the stress state, induced by the multiaxial loading, remains within the safe part of the stress space [3, 38].

Up to now, many multiaxial fatigue criteria have been proposed over decades of research in this area; however there is not still a universally accepted model, which covers different types of materials and load conditions. Focusing on the HCF regime, the main multiaxial fatigue criteria can be divided in following categories depending on the parameters used to describe the fatigue life or endurance limit of the material [3, 38-40, 43]:

- a) Empirical relationships which are modifications of the Coffin-Manson equation or established from fitting of experimental results.
- b) Approaches based on the stress or strain invariants. The main parameters of these criteria are the hydrostatic stress and the second invariant of the stress deviator tensor.
- c) Critical plane approaches: first of all a spatial plane inside the component is located, on which a linear function of normal and shear stresses (depending on the criterion) reaches its maximum. If the fatigue criterion is not fulfilled on the critical plane, then a fatigue crack may initiate along this plane.
- d) Use of average quantities of stress or strain with respect to different spatial planes inside the component. The average quantities are described generally by a double integral over two spherical coordinates, which describe the orientation of the spatial planes. In this way all possible orientations of the plane are considered.
- e) Approaches based on energy parameters, e.g. plastic strain energy, as a contributing factor in fatigue damage. There have not been remarkable developments in multiaxial HCF fatigue analysis using energy concepts [38-40, 43].

For evaluation of HCF criteria two facts should be taken into account, which are established by experimental results [3]:

- 1) The fatigue limit in cyclic torsion is dependent on the amplitude of shear stress and independent of the superimposed mean torsion stress. Sines analyzed fatigue results of 27 metals and concluded that the amplitude of the shear stress sustained by a specimen in cyclic torsion is unique [41].
- 2) The fatigue limit in cyclic bending is significantly dependent on the superimposed mean normal stress. This dependency can be described by a linear relationship according to the experimental results [41-42].

Now some of the well-known HCF criteria will be reviewed and the corresponding advantages and disadvantages will be discussed [3, 38-39, 43].

Gough and Pollard proposed two relatively simple equations for combined in-phase bending and torsion, named as "ellipse quadrant" criteria and applicable for ductile and brittle materials, respectively:

$$\left(\frac{\sigma_b}{f_{-1}}\right)^2 + \left(\frac{\sigma_t}{t_{-1}}\right)^2 = 1 \quad , \quad (1)$$

$$\left(\frac{\sigma_t}{t_{-1}}\right)^2 + \left(\frac{\sigma_b}{f_{-1}}\right)^2 \left(\frac{f_{-1}}{t_{-1}} - 1\right) + \left(\frac{\sigma_b}{f_{-1}}\right) \left(2 - \frac{f_{-1}}{t_{-1}}\right) = 1 \quad , \quad (2)$$

where σ_b and σ_t represent the bending and torsion stress amplitudes, and f_{-1} and t_{-1} the endurance limits in reversed bending and torsion, respectively [43-45]. These two equations are applicable just for biaxial loading and do not consider the possible phase differences between bending and torsion stresses. The empirical equations of this type, which are sometimes practical in engineering applications, can be implemented only for stress conditions that are identical or similar to the test parameters used during their establishment [3].

One of the popular HCF criteria using stress invariants was established by Sines:

$$\sqrt{J_{2,a}} + \kappa_s \sigma_{H,m} \leq \lambda_s \quad , \quad (3)$$

where $J_{2,a}$ is the amplitude of the second invariant of the stress deviator tensor, $\sigma_{H,m}$ the mean value of the hydrostatic stress, κ_s and λ_s two material parameters, which can be determined by uniaxial repeated bending and reversed torsion fatigue tests:

$$\kappa_s = \left(\frac{3t_{-1}}{f_o}\right) - \sqrt{3} \quad , \quad \lambda_s = t_{-1} \quad , \quad (4)$$

where f_o is the endurance limit in repeated bending [3, 41].

The Sines criterion satisfies the uniqueness of the torsion fatigue limit, and presents the linear dependence on the bending limit to the mean normal stress. According to this criterion, the ratio of fatigue limit in fully reversed torsion and bending, t_{-1}/f_{-1} , is constant for all metals, which is in disagreement with experimental results. Concerning this matter, Crossland modified the Sines criterion and applied the maximum value (instead of the mean value) of the hydrostatic stress [3].

Kakuno and Kawada improved the Sines criterion and considered both mean value and amplitude of the hydrostatic stress:

$$\sqrt{J_{2,a}} + \kappa_{k1}\sigma_{H,a} + \kappa_{k2}\sigma_{H,m} \leq \lambda_k \quad , \quad (5)$$

where κ_{k1} , κ_{k2} , and λ_k are material parameters defined by uniaxial fatigue experiments [3, 46-47].

One of the first fatigue criteria related to the concept of the critical plane was proposed by Findley. This criterion establishes a linear function between the amplitude of the shear stress C_a and the maximum value of the normal stress N_{\max} on the critical plane. Accordingly, the critical plane is defined by two angles (φ_c, θ_c) in spherical coordination system, which represent the orientation of the unit vector normal to the critical plane. On the critical plane, the following linear function reaches its maximum:

$$(\varphi_c, \theta_c): \max_{(\varphi, \theta)} \{C_a(\varphi, \theta) + \kappa_f N_{\max}(\varphi, \theta)\} \quad , \quad (6)$$

and the fatigue criterion on the critical plane reads as:

$$C_a(\varphi_c, \theta_c) + \kappa_f N_{\max}(\varphi_c, \theta_c) \leq \lambda_f \quad , \quad (7)$$

where κ_f and λ_f are two material parameters defined by two uniaxial fatigue experiments [3, 48].

The Findley criterion predicts a dependency of the torsion endurance limit on the mean torsion stress, which is not correct as mentioned before. Matake solved this issue by proposing a similar criterion, but the orientation of the critical plane was given only by amplitude of the shear stress:

$$(\varphi_c, \theta_c): \max_{(\varphi, \theta)} \{C_a(\varphi, \theta)\} \quad , \quad (8)$$

and the Matake criterion reads as the Findley criterion (Eq. 7) [3, 49].

McDiarmid established a similar criterion based on the critical plane approach, taking into account whether case A, cracks growing along the surface, or case B, cracks growing inward from the surface, occurs. The criterion requires knowledge of the material shear fatigue strengths for case A and case B cracks, which makes its application complicated, since the experimental data are not differentiated in this regard [3, 50].

The above mentioned fatigue criteria are based on physical parameters at macroscopic scale, and do not capture the fatigue mechanisms at the grain level leading to the initiation of cracks. Although the material behavior at the macroscopic scale is elastic in the HCF regime, still some metal grains suffer plastic strains, and the evolution of this irreversible process is responsible for the crack initiation in the HCF regime. Therefore for modeling of HCF, the material behavior and mechanical parameters at the grain level (mesoscopic scale) need to be considered.

The first multiaxial endurance limit criterion based on a mesoscopic scale approach was proposed by Dang Van in the 1970's. His criterion is based on Lin-Taylor assumptions in order to relate the mesoscopic and macroscopic strains [32]. Referring to Orowan plasticity theory [51] and the elastic shakedown concept, he postulated that the fatigue cracks do not initiate in a grain, if an elastic shakedown state is reached within the grain. Theoretical details of the elastic shakedown theorem are illustrated in section 3.3. The Dang Van criterion is defined as a linear combination between the shear stress and hydrostatic stress at mesoscopic scale [4-7, 33]:

$$\tau_{\max} + \kappa_d \Sigma_H \leq \lambda_d \quad , \quad (9)$$

where τ_{\max} is the maximum mesoscopic shear stress (equal to Tresca stress), and Σ_H the macroscopic hydrostatic stress, accordingly. The two material parameters κ_d and λ_d are determined by uniaxial fatigue experiments. During a load cycle, the term at the left side of Eq. 9 varies depending on the load path. Hence, the maximum value of this term should be calculated over the loading period. Fig. 2.3 illustrates the application of Dang Van criterion for a known loading path. The fatigue limit domain has been divided in two regions: safe and unsafe, respectively. The safe domain belongs to the points of the load path which are below the red line, and the failure domain (unsafe domain) relates to the points above this line, for which crack initiation in the grains is predicted.

The Dang Van criterion presents good agreement between prediction made by the criterion and the HCF test results for proportional loading; however, for non-proportional loading the results are not satisfactory enough, since the von-Mises criterion is used to model the plastic behavior of metal grains. Furthermore, calculations of mesoscopic stresses used in this criterion are

generally cumbersome. To solve these two issues, Papadopoulos generalized the Dang Van criterion and applied a link between mesoscopic and macroscopic parameters [6, 8-9]. However, the Papadopoulos HCF criterion is applicable for macroscopic scale and cannot predict the crack initiation in individual grains, which is essential for fatigue assessments in small scale applications, e.g. for MEMS.

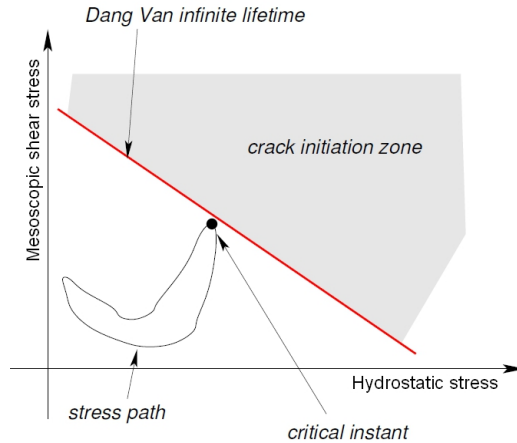


Fig. 2.3. Illustration of fatigue limit domain according to Dang Van criterion. Reference of the figure is [33], with some small modifications.

Theoretical principles of Dang Van and Papadopoulos criteria will be discussed in sections 3.1 to 3.3 and then a new HCF micro-mechanical model will be developed based on those theories, but applicable for individual grains and considering microstructure parameters, specifically grain size and grain orientation.

3 Micro-mechanical model for prediction of HCF

In this chapter, the main equations for the description of HCF damage mechanisms on the level of slip systems in individual grains are described. The equations will be utilized in developing the new HCF micro-mechanical model for small scales. After a short introduction in the plastic theory of metals grains, the approach for determination of the accumulated plastic shear strain is illustrated, as an important quantity to verify the HCF damage evolution. Then the elastic shakedown theorem will be discussed as a restraint to avoid fatigue crack initiation. In a further step, the HCF micro-mechanical model will be established for individual grains as a function of the microstructural parameters, i.e. grain size and grain orientation. The HCF model is firstly defined as a deterministic failure criterion; nevertheless, it works later as a core for the definition of a probabilistic model.

The fatigue processes in metal components originate in those grains that undergo plastic deformation in slip bands. Therefore the amplitude of mesoscopic plastic strains and corresponding accumulation rate over load cycles play a key role in initiation of fatigue micro-cracks in the grains. In this context, crack initiation is understood as the failure of the most unfavorably oriented grains, which undergo plastic deformation. To investigate the fatigue evolution in such grains, the accumulated plastic shear strain at the mesoscopic scale is considered as a damage variable in the HCF model. For the description of the material behavior and fatigue mechanisms at the mesoscopic level, the mesoscopic stresses and strains should be linked to the macroscopic stresses and strains. For this purpose, the related plasticity theories⁴ will be discussed in section 3.1.

⁴ Theories and equations presented in sections 3.1 to 3.3 are mainly based on the previous work of Dang Van and Papadopoulos. Readers are referred to [4-6, 8-9] for more details. To avoid redundancy the references are not mentioned for each equation or part of the text separately.

3.1 Plasticity theory of metal grains

In the HCF regime and at the endurance limit, the magnitude of cyclic loads is so low that the macroscopic behavior of the material can be considered as purely elastic, and therefore, the plastic strain is negligible. The macroscopic fields of stress $\underline{\underline{\Sigma}}$ and strain $\underline{\underline{E}}$ are related by Hooke's law:

$$\underline{\underline{\Sigma}} = \underline{\underline{C}} : \underline{\underline{E}} \quad , \quad (10)$$

and

$$\underline{\underline{E}} = \underline{\underline{L}} : \underline{\underline{\Sigma}} \quad , \quad (11)$$

where C and L are the macroscopic stiffness and compliance fourth-rank tensor of the material, respectively. For an isotropic and linear elastic material, the macroscopic stiffness tensor C can be written by index notation as following:

$$C_{ijkl} = \lambda \delta_{ij} \delta_{kl} + \mu (\delta_{il} \delta_{jk} + \delta_{ik} \delta_{jl}) \quad , \quad (12)$$

where λ and μ are the Lamé coefficients and δ_{ij} is the Kronecker Delta tensor, respectively.

Even if at the macroscopic scale the material behaves in an elastic manner, at the mesoscopic scale there are always some plastically less resistant grains that undergo plastic slip. The mesoscopic strain of such a grain is composed by an elastic part ε^e and a plastic part ε^p :

$$\underline{\underline{\varepsilon}} = \underline{\underline{\varepsilon}}^e + \underline{\underline{\varepsilon}}^p \quad (13)$$

The mesoscopic stress σ is related to the elastic part of the mesoscopic strain ε^e by Hooke's law:

$$\underline{\underline{\sigma}} = \underline{\underline{c}} : \underline{\underline{\varepsilon}}^e \quad , \quad (14)$$

and

$$\underline{\underline{\varepsilon}}^e = \underline{\underline{l}} : \underline{\underline{\sigma}} \quad , \quad (15)$$

where c and l are mesoscopic stiffness and compliance tensors, respectively. These tensors are not isotropic because they refer to the grains of the aggregate.

Due to the low magnitude of the stresses and strains in endurance limit of the HCF regime, just a few grains suffer plastic slip. Therefore it can be assumed that each plastically deforming grain is surrounded by grains which show elastic behavior. These surrounding grains dictate their strain to the grain undergoing plastic slips. The strain of these surrounding grains is in average equal to the macroscopic strain E . According to Lin-Taylor theorem, the plastically deformed grain is exposed to a strain equal to the macroscopic strain E :

$$\underline{\underline{E}} = \underline{\underline{\varepsilon}}^e + \underline{\underline{\varepsilon}}^p \quad (16)$$

By introducing of the inner product (scalar product) of the macroscopic stiffness tensor C (i.e. contraction with tensor C) in both sides of Eq. 16 and performing some mathematic simplifications it can be shown that:

$$\underline{\underline{\Sigma}} = \underset{4}{C} : \underset{4}{l} : \underline{\underline{\sigma}} + 2\mu \underline{\underline{\varepsilon}}^p \quad (17)$$

The inner product of the macroscopic stiffness tensor C and mesoscopic compliance tensor l presents the localization tensor, which is assumed here to be equal to the unit tensor I . As it will be verified later, this assumption leads to reasonably accurate results in this work. Therefore the Eq. 17 can be re-written as:

$$\underline{\underline{\sigma}} = \underline{\underline{\Sigma}} - 2\mu \underline{\underline{\varepsilon}}^p \quad (18)$$

The plastic strain ε^p is caused by dislocation movements along slip systems of the grain. A slip system can be defined by a slip plane and a slip direction. For that a unit vector \underline{n} , normal to the plane, and a unit vector \underline{m} , along the slip direction, are used.

Fig. 3.1 illustrates a body exposed to the macroscopic stress tensor $\underline{\underline{\Sigma}}$. Considering a slip plane Δ in a point inside of this body, the slip direction and the normal to the slip plane can be shown with vectors \underline{m} and \underline{n} , respectively. The macroscopic stress vector $\underline{\Sigma}_\Delta$ acting on the slip plane Δ has a shear stress component \underline{C} and a normal stress component \underline{N} . The projection of the vector \underline{C} on

the slip direction m is the vector \underline{T} , which demonstrates the macroscopic resolved shear stress along this slip direction, and oscillates between point A and B during a load cycle. Considering a grain, whose slip direction is located on the plane Δ , the mesoscopic stress vector acting on the slip plane of the grain is denoted as $\underline{\sigma}_\Delta$. Accordingly the mesoscopic normal and resolved shear stress (along direction m) are presented as vectors $\underline{\nu}$ and $\underline{\tau}$ (Fig. 3.2).

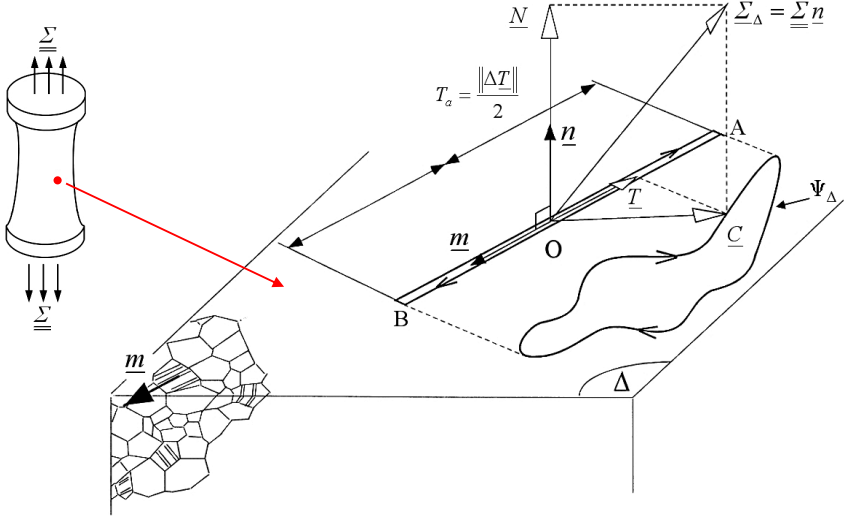


Fig. 3.1. Application of macroscopic stresses on a body (left), and resulting stress components on a slip plane Δ located inside of the body (right). Reference of the right figure is [62], with some small modifications.

The macroscopic stress vector $\underline{\underline{\Sigma}}_\Delta$ can be determined knowing the macroscopic stress tensor $\underline{\underline{\Sigma}}$:

$$\underline{\underline{\Sigma}}_\Delta = \underline{\underline{\Sigma}} \underline{n} \quad , \quad (19)$$

and in a similar way the mesoscopic stress vector $\underline{\sigma}_\Delta$ reads as:

$$\underline{\sigma}_\Delta = \underline{\sigma} \underline{n} \quad (20)$$

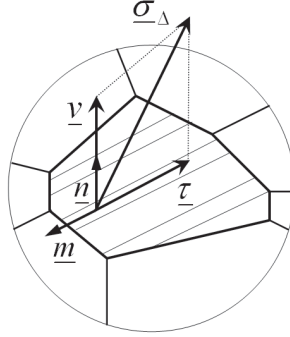


Fig. 3.2. Mesoscopic stress vector $\underline{\sigma}_\Delta$ acting on the slip plane Δ of a grain, and corresponding vectors of mesoscopic normal and resolved shear stresses. The figure is drawn based on reference [9].

The macroscopic and mesoscopic stress vectors can be linked together using Eq. 18:

$$\underline{\sigma}_\Delta = \underline{\underline{\sigma}} \underline{n} = (\underline{\underline{\Sigma}} - 2\mu \underline{\underline{\varepsilon}}^p) \underline{n} = \underline{\underline{\Sigma}}_\Delta - 2\mu \underline{\underline{\varepsilon}}^p \underline{n} = \underline{\underline{\Sigma}}_\Delta - \mu \gamma^p \underline{m} = \underline{\underline{\Sigma}}_\Delta - \mu \underline{\underline{\gamma}}^p, \quad (21)$$

where $\underline{\underline{\gamma}}^p$ is the vector of plastic shear strain along slip direction m and γ^p the magnitude of this vector. In Eq. 21, it is assumed that only one slip system in the grain is active (along direction m), which is the typical behavior of polycrystalline metals in the HCF regime (with low magnitude of cyclic loads). Therefore in the last equation of Eq. 21 the relationship $\gamma^p \underline{m} = \underline{\underline{\gamma}}^p$ has been introduced.

Accordingly, the relation between macroscopic and mesoscopic shear stresses can be derived as following:

$$\underline{\tau} = (\underline{m} \cdot \underline{\sigma}_\Delta) \underline{m} = \left[\underline{m} \cdot (\underline{\underline{\Sigma}}_\Delta - \mu \gamma^p \underline{m}) \right] \underline{m} = \underline{T} - \mu \gamma^p \underline{m} = \underline{T} - \mu \underline{\underline{\gamma}}^p, \quad (22)$$

where \underline{T} and $\underline{\tau}$ are the vectors of macroscopic and mesoscopic resolved shear stresses along the slip direction m , respectively.

The plastic slip in grains can be described by Schmid law ⁵, which is verified by many experimental results performed on single crystals in static and cyclic loading [52-56]. Accordingly the plastic slip is initiated in the grains of metals, if the resolved shear stress acting on the slip plane and along the slip direction reaches the current yield limit τ_y . In such case the plasticity criterion related to Schmid law reads as:

$$f(\underline{\tau}, \underline{b}, \tau_y) = (\underline{\tau} - \underline{b}) \cdot (\underline{\tau} - \underline{b}) - \tau_y^2 = 0 \quad , \quad (23)$$

and

$$\frac{\partial f(\underline{\tau}, \underline{b}, \tau_y)}{\partial \underline{\tau}} \cdot \underline{\tau} > 0 \quad , \quad (24)$$

where function $f(\underline{\tau}, \underline{b}, \tau_y)$ is the plastic potential, and vector \underline{b} the kinematic hardening parameter.

The plastic strain rate $\dot{\underline{\gamma}}^p$ is given by the normality rule:

$$\dot{\underline{\gamma}}^p = \dot{\lambda} \frac{\partial f}{\partial \underline{\tau}} = 2 \dot{\lambda} (\underline{\tau} - \underline{b}) \quad , \quad (25)$$

where $\dot{\lambda}$ is the plastic multiplier rate and can be determined using the consistency equation:

$$\dot{f} = 0 \Rightarrow \frac{\partial f}{\partial \underline{\tau}} \cdot \dot{\underline{\tau}} + \frac{\partial f}{\partial \underline{b}} \cdot \dot{\underline{b}} + \frac{\partial f}{\partial \tau_y} \dot{\tau}_y = 0 \quad (26)$$

Assuming that only one slip system is active in plastically deformed grains – as is the case in the HCF regime – the plastic behavior of the grain can be modeled according to a combined kinematic and isotropic hardening rule. The isotropic hardening rule is written as:

⁵ The Schmid law is accurate for fcc metals, but yields poor results for bcc metals [57-61]. It has been applied in this work, since fcc metals (e.g. nickel) have been used for fatigue experiments.

$$\dot{\underline{\tau}}_y = h\sqrt{\dot{\underline{\gamma}}^p \cdot \dot{\underline{\gamma}}^p} \quad , \quad (27)$$

where h is the isotropic hardening coefficient.

Furthermore the kinematic hardening rule reads as:

$$\dot{\underline{b}} = c\dot{\underline{\gamma}}^p \quad , \quad (28)$$

where c is a constant with positive value.

Now with the aim of the consistency equation (Eq. 26) and the hardening rules (Eq. 27 and Eq. 28) the plastic multiplier $\dot{\lambda}$ can be determined:

$$\dot{\lambda} = \frac{(\underline{\tau} - \underline{b}) \cdot \dot{\underline{\tau}}}{2(c + h)\tau_y^2} \quad (29)$$

Replacing this relationship for plastic multiplier $\dot{\lambda}$ in Eq. 25 and using the plastic criterion (Eq. 23), the rate of the plastic shear strain will be given as:

$$\dot{\underline{\gamma}}^p = \frac{\dot{\underline{\tau}}}{(c + h)} \quad (30)$$

The above equation relates the rate of the mesoscopic plastic shear strain $\dot{\underline{\gamma}}^p$ to the mesoscopic shear stress $\underline{\tau}$. Substitution of mesoscopic shear stress from Eq. 22 will result in an important relationship:

$$\dot{\underline{\gamma}}^p = \frac{\dot{\underline{T}}}{(c + h + \mu)} \quad (31)$$

So a link is established between the mesoscopic plastic shear strain $\dot{\underline{\gamma}}^p$ and the macroscopic resolved shear stress $\dot{\underline{T}}$. This relationship will be applied in section 3.2 to determine the accumulated plastic shear strain over an infinite number of load cycles, which plays the role of a damage variable in the HCF model.

3.2 Accumulated plastic shear strain in a slip system

The rate of the plastic shear strain accumulation along an active slip system of a grain, denoted as $\dot{\Gamma}$, reads as:

$$\dot{\Gamma} = \sqrt{\dot{\gamma}^p \cdot \dot{\gamma}^p} \quad , \quad (32)$$

The goal is to determine the accumulated plastic shear strain after an infinite number of load cycles, denoted as Γ_∞ :

$$\Gamma_\infty = \lim_{N \rightarrow \infty} \int_0^{NP} \dot{\Gamma} dt = \lim_{N \rightarrow \infty} \int_0^{NP} \sqrt{\dot{\gamma}^p \cdot \dot{\gamma}^p} dt = \lim_{N \rightarrow \infty} \int_0^{NP} \frac{\sqrt{\dot{T} \cdot \dot{T}}}{(c+h+\mu)} dt \quad , \quad (33)$$

where P is the time period for one load cycle and N the number of load cycles.

For the calculation of the right hand side of the above equation over an infinite number of load cycles, the accumulation rate of the plastic shear strain over each load cycle needs to be known. Considering the plastic criterion (Eq. 23) and hardening rules (Eq. 27 and Eq. 28) the plastic shear strain accumulated in each load cycle, denoted as $\delta\Gamma$, can be determined as:

$$\delta\Gamma = \Gamma_{A \rightarrow B} + \Gamma_{B \rightarrow A} = \frac{2(c+\mu)}{(c+h+\mu)^2} (\|\Delta T\| - 2\tau_y^A) \quad , \quad (34)$$

where $\Gamma_{A \rightarrow B}$ and $\Gamma_{B \rightarrow A}$ describe the accumulated plastic shear strain during load cycling between points A and B and vice versa (Fig. 3.1). The variation of the resolved shear stress vector between points A and B is denoted as $\|\Delta T\|$, which is twice of the amplitude of the resolved shear stress T_a . The flow stress of the grain at point A of the load cycle is shown as τ_y^A . Before the start of the load cycle (at point O), the initial yield stress of the grain is equal to τ_y^0 . The variation of the flow stress during each load cycle can be determined using the isotropic hardening rule (Eq. 27):

$$\Delta \tau_y = h \delta \Gamma \quad (35)$$

Using Eq. 34 and Eq. 35 the plastic shear strain accumulated in successive load cycles can be determined as:

$$\delta \Gamma^N = \eta \delta \Gamma^{N-1} \quad , \quad (36)$$

where the ratio η is given by:

$$\eta = \left(\frac{c - h + \mu}{c + h + \mu} \right)^2 \quad (37)$$

Since the material parameters in Eq. 37 have positive values, the ratio η will have a value between 0 and 1. Hence, over infinite number of load cycles the rate of plastic strain accumulation reduces to zero, and consequently the accumulated plastic shear strain converges to a specific value. Using Eq. 33 to Eq. 37, it can be shown that for constant-amplitude multiaxial loading the accumulated plastic shear strain Γ_∞ for each slip system of a grain in the endurance limit is directly proportional to the difference between the amplitude of the macroscopic shear stress T_a and the initial yield stress τ_y^o in the following manner⁶:

$$\Gamma_\infty = \frac{(T_a - \tau_y^o)}{h} \quad (38)$$

It is presumed in Eq. 38 that the grain has an unlimited capacity of isotropic hardening which implies that it tends to an elastic shakedown. At this point it is necessary to give some more details about the elastic shakedown theorem, since this concept will be used later when establishing the HCF micro-mechanical model.

⁶ For variable amplitude loading, Eq. 38 should be modified accordingly, which is out of scope of this work. Readers are referred to [62-64] for some more details on this topic.

3.3 Elastic shakedown

The behavior of the material subjected to cyclic plastic straining can differ in three forms as illustrated in Fig. 3.3: elastic shakedown, plastic shakedown (or reversed cyclic plasticity), and plastic ratcheting. Elastic shakedown corresponds to the stress or strain level, below which there is vanishing cyclic plasticity. This condition is obtained, if the plastic deformation occurs during the early load cycles and then a steady state is reached, so the response of the material is fully elastic due to the build-up of residual stresses [16]. In the HCF regime, a component exhibits an elastic behavior at the macroscopic scale and only some localized plasticity can take place in unfavorably oriented grains. At the endurance limit, it is assumed that after a certain number of cycles the tensors of the amplitudes for plastic strains and residual stresses remain constant. So, the stress tensor corresponds to a pure elastic response of the grains at all scales; the material is in elastic shakedown state at all scales.

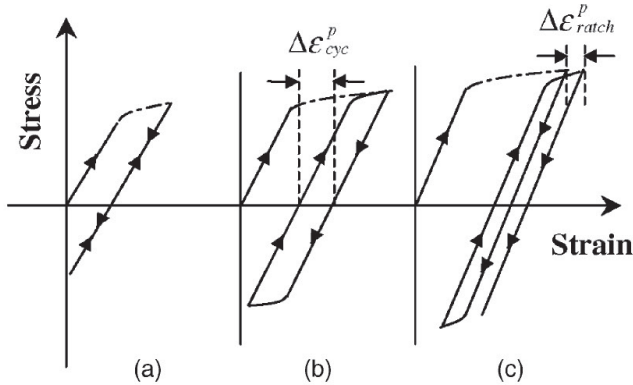


Fig. 3.3. Plastic strain behavior under cyclic loading: a) elastic shakedown, b) plastic shakedown, c) plastic ratcheting [16].

For the description of the material response in the case of elastic shakedown, different models have been proposed. The classical model for elastic perfectly-plastic materials, known as Melan's theorem, states that if for any point x in the component there are a self-equilibrated time-independent residual stress field

$\underline{\underline{\sigma}}^r(x)$ and a safety coefficient $m > 1$, such that the following plastic criterion is satisfied, then the component will shakedown elastically [65-68]:

$$\forall x, \forall t > t_0: f(m(\underline{\underline{\sigma}}^e(x,t) + \underline{\underline{\sigma}}^r(x))) \leq 0 \quad , \quad (39)$$

where f is the plastic potential (yield criterion), and σ^e the tensor of the elastic stress field, respectively. The condition, that the residual stress field must be self-equilibrated, is difficult to fulfill. Therefore, this theorem was extended later by other authors considering more realistic material behavior. Mandel *et al.* proposed another theorem for isotropic and kinematic hardening materials to estimate the elastic shakedown [66]. According to this theorem, elastic shakedown occurs if there is a time independent stress tensor σ^* for each point x in the component such that:

$$\forall x, \forall t > t_0: f(\underline{\underline{\sigma}}^e(x,t) - \underline{\underline{\sigma}}^*(x)) < k_{\max}^2(\varepsilon_{eq}^p(x)) \quad , \quad (40)$$

where k is the isotropic hardening parameter (yield radius), which increases with the accumulated equivalent plastic strain ε_{eq}^p . The maximum allowable value of the yield radius (before failure) is represented by k_{\max} . It is supposed that the plastic strains are small (as in the case of HCF regime) and the accumulated equivalent plastic strain ε_{eq}^p is defined by:

$$\varepsilon_{eq}^p = \int_0^t \sqrt{\frac{2}{3} \dot{\underline{\underline{\varepsilon}}}^p : \dot{\underline{\underline{\varepsilon}}}^p} dt \quad (41)$$

Returning back to Eq. 38, to reach an infinite life in the HCF regime and to avoid fatigue crack initiation in the grains, the accumulated plastic shear strain in each grain after a high number of load cycles must not exceed a critical limit, denoted here as Γ_c . Consequently, each grain remains in the hardening phase and necessarily elastic shakedown occurs. So after a certain number of cycles a stabilized elastic state is reached and the tensor of the plastic strain becomes constant and independent of time.

Considering an individual grain, the accumulated plastic shear strain Γ_∞ should be checked for all slip systems of the grain and compared with the critical limit Γ_c :

$$\Gamma_\infty \leq \Gamma_c \quad (42)$$

By application of Eq. 42 for an aggregate of grains (e.g. a RVE) a critical plane should be found, along which the shear stress attains its maximum value. Assuming that the distribution of grain orientation inside the considered volume is homogenous, there will be some grains so orientated that their weakest slip system coincides with this plane. Hence the criterion reads as:

$$\max_{\varphi, \theta, \chi} \{\Gamma_\infty(\varphi, \theta, \chi)\} \leq \Gamma_c \quad , \quad (43)$$

or

$$\frac{1}{h} [\max_{\varphi, \theta, \chi} T_a(\varphi, \theta, \chi) - \tau_y^o] \leq \Gamma_c \quad , \quad (44)$$

where φ and θ define the orientation of the plane on which the shear stress is maximum and χ corresponds to the direction of the resolved shear stress on this plane.

In macroscopic applications, the fatigue criterion corresponds to the creation of cracks propagating through hundreds of grains, rather than to rupture of an individual grain. In such cases it would be sufficient to verify just the average of the accumulated plastic shear strain for all grains located at the macroscopic point of consideration and having different spatial orientations. For example, Papadopoulos used the root mean square of the resolved shear stress over spatial orientations (given by angles φ , θ , χ) and developed a criterion for prediction of multiaxial HCF at macroscopic scale. Since pre-existing defects or small cracks can influence the fatigue strength, he introduced in his criterion the average of the normal stress (over angles φ and θ), which is equal to the hydrostatic stress [69].

The Papadopoulos criterion reads as [3, 8-9]:

$$\sqrt{\langle T_a^2 \rangle} + \kappa_p \Sigma_{H,\max} \leq \lambda_p \quad , \quad (45)$$

where $\Sigma_{H,\max}$ is the maximum of the hydrostatic stress in a load cycle. The two material parameters κ_p and λ_p can be obtained by uniaxial reversed bending and torsion fatigue tests. The average terms related to the resolved shear stress and normal stress over spatial angles are given by following relationships:

$$\sqrt{\langle T_a^2 \rangle} = \sqrt{\frac{5}{8\pi^2} \int_{\varphi=0}^{2\pi} \int_{\theta=0}^{\pi} \int_{\chi=0}^{2\pi} [T_a(\varphi, \theta, \chi)]^2 d\chi \sin\theta d\theta d\varphi} \quad , \quad (46)$$

and

$$\Sigma_H = \langle N \rangle = \frac{1}{4\pi} \int_{\varphi=0}^{2\pi} \int_{\theta=0}^{\pi} N(\varphi, \theta) \sin\theta d\theta d\varphi \quad (47)$$

The Papadopoulos criterion provides satisfactory results in predicting HCF fracture at macroscopic scale for proportional and non-proportional loading, but it can not predict the initiation of HCF cracks in individual grains, since it considers only the aggregates of grains with homogenous material parameters and stress distribution. In small scale applications, e.g. for micro-components, the fatigue cracks in individual grains can lead to the failure of the whole component. In such cases, HCF failure should be verified for each grain, where the microstructure and material parameters of the grain need to be considered too. In the next section a new micro-mechanical model for prediction of HCF failure at the grain level will be established, which takes into account the influence of microstructural parameters. The main parameters for describing of the microstructure are the grain size and the grain orientation, which affect the fatigue strength.

3.4 Micro-mechanical model for prediction of HCF at small scales

In the last section, it was discussed that the accumulated plastic shear strain Γ_∞ is the main contributor to the initiation of micro-cracks in the grains, and if Γ_∞ is bounded in the limits defined by the elastic shakedown theorem, then no crack initiation is expected in the grains. The aim of this section is to illustrate the dependency of the accumulated plastic shear strain on the microstructural parameters for each grain, specially grain size and grain orientation. After that, a failure function will be introduced which works as a criterion for prediction of HCF failure in individual grains.

Considering the parameters of Eq. 38, it is known that the yield limit τ_y^o is dependent on the grain size, and different relations are used to model its grain size dependency [70-71]. Here a Hall-Petch-type equation is implemented, as it was illustrated by Weng in [13], because it is easily adopted into Eq. 38, and also because of the good agreement between experimental and theoretical results:

$$\tau_y^o = \tau_y^\infty + k \cdot d^{-\frac{1}{2}}, \quad (48)$$

where τ_y^∞ is the yield stress of the slip system in a single crystal (with infinite size), d the grain size, and k a material parameter.

A further important parameter of Eq. 38, which needs to be examined, is the amplitude of the resolved shear stress, T_a . The vector of resolved shear stress \underline{T} along a slip direction can be written in terms of macroscopic stresses and vectors of the related slip system. Referring to Fig. 3.1, the vector \underline{C} represents the macroscopic shear stress component acting on the slip plane Δ . During a complete load cycle, the tip of vector \underline{C} describes a closed planar curve Ψ_Δ . The projection of the vector \underline{C} on the slip direction m gives the resolved shear stress vector \underline{T} , and the amplitude of the macroscopic shear stress T_a is equal to the half of the length generated by projection of the curve Ψ_Δ on the slip direction (between points A and B). The length of the

resolved shear stress vector \underline{T} at each moment of the load period can be described as a function of the macroscopic stress components and the vectors of slip system [8]:

$$\|\underline{T}\| = \underline{m} \cdot (\underline{\Sigma} \underline{n}) = m_x n_x \Sigma_{xx} + m_y n_y \Sigma_{yy} + m_z n_z \Sigma_{zz} + (m_x n_y + m_y n_x) \Sigma_{xy} + (m_x n_z + m_z n_x) \Sigma_{xz} + (m_y n_z + m_z n_y) \Sigma_{yz} \quad (49)$$

where Σ_{ij} are components of the macroscopic stress tensor. m_i and n_i are vector components of the slip direction and normal to the slip plane, respectively. Calculation of the amplitude of the resolved shear stress, T_a , with help of Eq. 49 is straightforward for a proportional multiaxial loading; for which the amplitude of each stress component, $\Sigma_{ij,a}$, should be applied in the equation. However for a non-proportional or out-of-phase loading it needs some more analytical calculations [3].

In face-centered-cubic (fcc) metals (e.g. nickel), the dislocation movements are on $\{111\}$ -planes with slip directions along $\langle 110 \rangle$, building totally 12 slip systems, which are listed in Table 3.1. The slip plane (111) and three slip directions located on this plane are shown in Fig. 3.4 for a fcc crystal.

Table 3.1. Slip planes and slip directions for a fcc crystal.

Slip plane	Slip direction
(1,1,1)	$\langle 1,1,0 \rangle, \langle 1,0,1 \rangle, \langle 0,1,1 \rangle$
(1,-1,1)	$\langle 1,1,0 \rangle, \langle 1,0,1 \rangle, \langle 0,1,1 \rangle$
(-1,-1,1)	$\langle 1,1,0 \rangle, \langle 1,0,1 \rangle, \langle 0,1,1 \rangle$
(-1,1,1)	$\langle 1,1,0 \rangle, \langle 1,0,1 \rangle, \langle 0,1,1 \rangle$

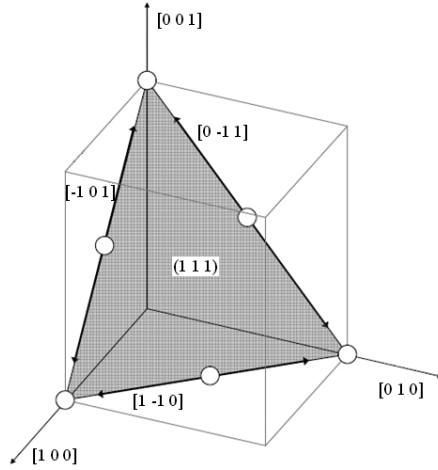


Fig. 3.4. Slip plane (111) and related slip directions for a fcc crystal. Reference of the figure is [33], with small modifications.

With respect to a global coordinate system, the slip directions are dependent on the grain orientation. Therefore, the resolved shear stress \underline{T} in Eq. 49 is implicitly a function of the grain orientation. In this work the Euler-angles⁷ are used for definition of the grain orientation [72], so that any rotation from the global coordinate system can be described using three angles (ϕ, θ, ψ) . The definition of Euler-angles and the associated mathematical relations are given in Appendix A1.

Replacing τ_y^o and T_a in Eq. 38 with the related expressions (from Eq. 48 and Eq. 49), the accumulated plastic shear strain Γ_∞ is obtained as a function of the grain size, grain orientation, and macroscopic stresses, in a form that is also suitable for probabilistic considerations of the fatigue reliability:

$$\Gamma_\infty(d, \phi, \theta, \psi, \underline{\Sigma}) = \frac{T_a(\phi, \theta, \psi, \underline{\Sigma}) - \tau_y^o - k \cdot d^{-\frac{1}{2}}}{h} \quad (50)$$

⁷ The reason for choosing of Euler method in this work was its compliance to the format of the experimental data, extracted by EBSD method for grain orientation [73-75]. See chapter 5 for details of experimental approach.

In probabilistic reliability theory, the failure behavior of a system can be described in terms of a failure function g depending on basic random variables X_i ($i=1, \dots, n$), which denote quantities of interest, e.g. applied loads and parameters of structural resistance. By convention $g(x) < 0$ implies failure, whereas no failure occurs for $g(x) > 0$. $g(x) = 0$ defines the so-called failure surface, a hyper-surface in the n -dimensional space of basic variables X_i , which separates the failure domain ($g(x) < 0$) and the safe domain ($g(x) > 0$) [76]. In our case, the failure function is formulated as $g(d, \phi, \theta, \psi, \underline{\Sigma})$ and interpreted as a criterion for prediction of the fatigue failure including all parameters of Eq. 50 as well as the critical limit Γ_c . To fulfill elastic shakedown and avoid crack initiation in grains, the accumulated plastic shear strain must be less than the critical limit Γ_c (referring to Eq. 42). Hence the failure function must have a value greater than or equal to zero for each slip system, and can be stated as:

$$g(d, \phi, \theta, \psi, \underline{\Sigma}) = \Gamma_c - \frac{T_a(\phi, \theta, \psi, \underline{\Sigma}) - \tau_y^\infty - k \cdot d^{-\frac{1}{2}}}{h} \geq 0 \quad (51)$$

The variables of the failure function in Eq. 51 can be divided into three groups related to:

- 1) microstructure parameters (grain size and grain orientations): d, ϕ, θ, ψ
- 2) material parameters: $k, h, \Gamma_c, \tau_y^\infty$
- 3) loading parameters (macroscopic stresses): $\underline{\Sigma}_{ij}$.

All these quantities will affect the failure behavior in a way that depends on the characteristic values as well as on the variability of the quantities.

In the following the function $g(d, \phi, \theta, \psi, \underline{\Sigma})$ will be used in two different ways:

- a) as a deterministic failure criterion for individual grains, when all variables of the function are known for each individual grain.
- b) as a failure function in probabilistic studies on aggregates of grains, if the variables are given by stochastic distributions. For example if grains have a preferred orientation or size distribution due to the manufacturing processes (e.g. rolling direction of the plates), then the texture of the microstructure can be estimated using data of similar samples.

The following chapter 4 provides more details and examples for both types of application of the failure function $g(d, \phi, \theta, \psi, \underline{\Sigma})$. Furthermore, the influence of different variables of $g(\cdot)$ on HCF failure will be studied.

4 Parameter study

After establishing the new failure function for prediction of HCF failure, a parameter study is performed:

- a) to verify the influence of different variables of the failure function on the occurrence of HCF damage,
- b) to investigate the sensitivity of the failure function with respect to different parameters, and
- c) to investigate the influence of parameter uncertainties on failure function predictions.

The main focus of the parameter study is on the microstructure parameters, e.g. grain size and grain orientation. In selected cases material parameters are also evaluated. By means of different examples, it is illustrated how the HCF model can be applied either as a failure criterion for deterministic prediction in individual grains, or in probabilistic studies on aggregates of grains.

4.1 Deterministic study of parameters

In a first step of the parameter study, two variables of the failure function are considered: grain size d , and resolved shear stress T_a . It is assumed that all grains have the same orientation and identical slip systems. Material parameters of nickel are applied for the parameter study; corresponding to the material of the micro-samples used for HCF experiments in this work. Material data for Ni taken from the literature are given in Table 4.1 [77-78]. The critical limit of the accumulated plastic shear strain, Γ_c , was also estimated from available data in the literature [79-81]. Fig. 4.1 depicts contour lines of the failure function $g(d, T_a)$ in dependence on the grain size d and amplitude of the resolved shear stress T_a . Each contour line is the locus of the points with equal value of failure function $g(d, T_a)$ but with varying grain size d and amplitude of resolved shear stress T_a . For grains larger than 20 μm the failure function is relatively insensitive to the grain size, while for grains smaller than 10 μm a significant dependence on the grain size is present. On the other hand the value of the failure function decreases with increasing grain size, indicating that for larger

grains the HCF failure is more probable. These two effects are typical for equations containing terms of $(1/x^{(n)})$ as in the failure function, and will be verified later by experimental results.

Table 4.1. Material parameters of Ni.

Material parameter	Value	Unit
k	160	$[MPa \cdot \mu m^{1/2}]$
h	1	$[MPa]$
τ_y^∞	22	$[MPa]$
Γ_c	100	$[-]$

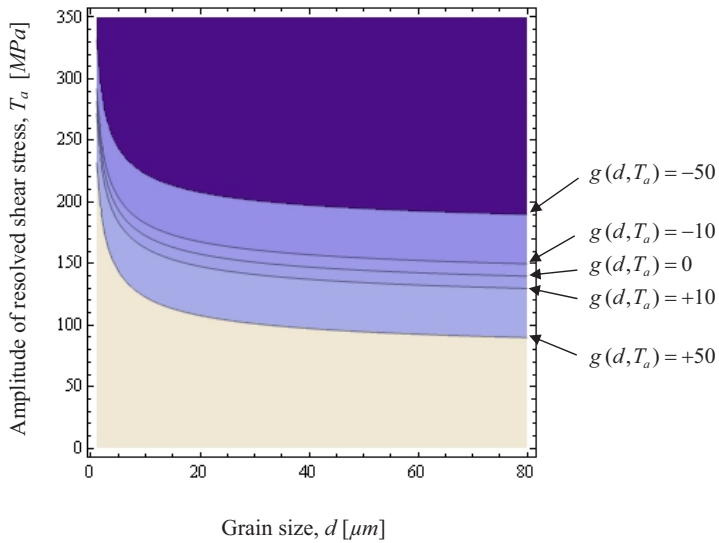


Fig. 4.1. Contour lines of failure function $g(d, T_a)$ in dependence of grain size and resolved shear stress.

After dealing with grain size and resolved shear stress, grain orientation is the other important variable in the HCF model to be considered, since it affects the resolved shear stress along each slip direction. The first and second Euler-angles, ϕ and θ , are considered as variable in the failure function, while the third Euler-angle, ψ , and the grain size, d , are held as constant and given by typical values obtained from micro-samples used in HCF experiments. Fig. 4.2 gives a surface plot of failure function $g(\phi, \theta)$ versus first and second Euler-angles for slip system (111), [110] of Ni. The graph is obtained by assuming a constant third Euler-angle ψ of 45° and a grain size d of $20 \mu\text{m}$. The surface has a periodic shape, since transformation relations between Euler-angles and slip directions include trigonometric functions based on sine and cosine terms illustrated in Appendix A1.

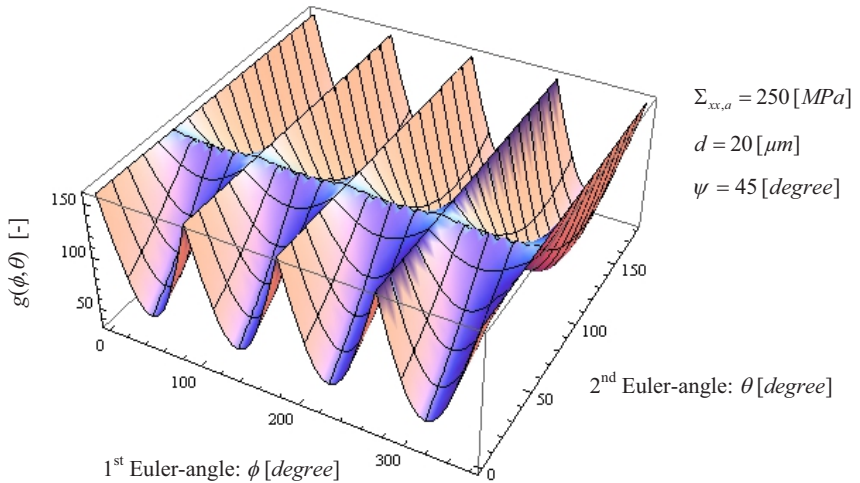


Fig. 4.2. Surface plot of $g(\phi, \theta)$ versus 1st and 2nd Euler-angle for slip system (111), [110] of Ni.

According to Fig. 4.2, certain ranges of Euler-angles lead to pronounced changes in the failure function and consequently in the probability of HCF failure, while for other Euler-angles the failure function is mostly independent on those angles. For the second Euler-angles near to 0° or 180° , the failure

function is very sensitive to the variations of the first Euler-angle, specially in periods of 90° (0° , 90° , 180° ,...). For second Euler-angles near to 55° , the failure function is essentially insensitive to the variations of the first Euler-angle.

Contour lines of failure function $g(\phi, \theta)$ versus first and second Euler-angles are shown in Fig. 4.3, corresponding to the surface plot presented in Fig. 4.2.

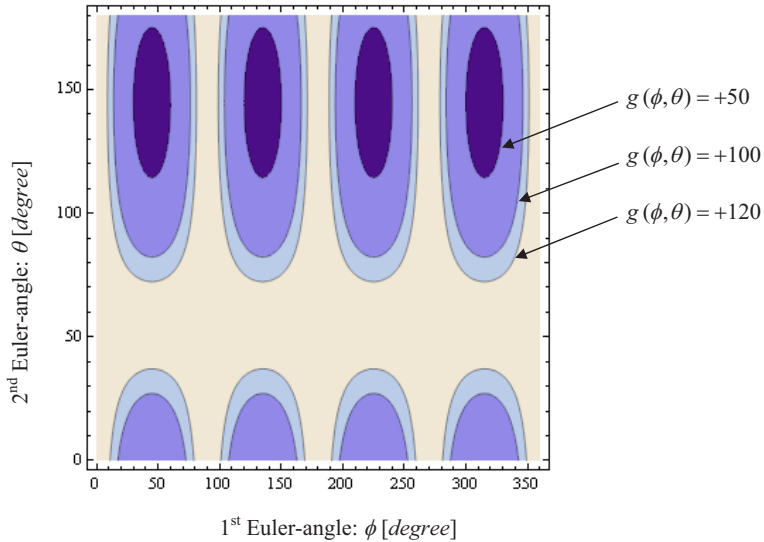


Fig. 4.3. Contour lines of $g(\phi, \theta)$ versus first and second Euler-angle. Parameter set as in Fig. 4.2.

To generalize the results of Fig. 4.2 and Fig. 4.3 to all three Euler-angles, a contour surface of the failure function $g(\phi, \theta, \psi)$ versus all three angles is illustrated in Fig. 4.4. This toroidal contour surface is the locus of the points with a failure function equal to zero but with different sets of Euler-angles. For a given set of parameters (d, Σ) the surface separates orientations on the outside of the toroidal surface, which lead to no HCF failure ($g > 0$), from unfavorable orientations represented by the interior of the toroid, where HCF failure is predicted ($g < 0$).

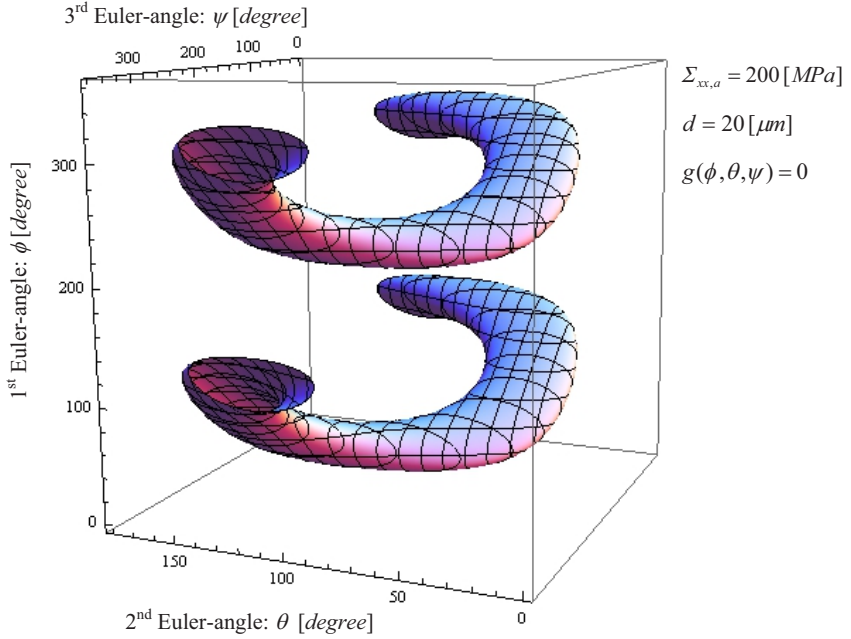


Fig. 4.4. Contour surface of failure function versus three Euler-angles for slip system (-111), [101] of Ni.

In Fig. 4.2 to Fig. 4.4, the failure function $g(\cdot)$ was analyzed just for a certain slip system. Now it turns out, if there is a specific slip system (between different slip systems), which represents the weakest slip system to HCF failure; if the minimum value of the failure function belongs always to a specific slip system, independent of load condition or Euler-angles. In Fig. 4.5 the failure function $g(\phi)$ is plotted versus the first Euler-angle ϕ for different slip systems of a fcc metal (in this case nickel) considering a certain load condition. Fig. 4.5 shows that there is no specific slip system, which leads to the minimum value of failure function $g(\phi)$ for an arbitrary load condition and over the whole range of Euler-angles. Furthermore, it was noticed that depending on the load condition, the arrangement of the curves in Fig. 4.5 (belonging to different slip systems) varies.

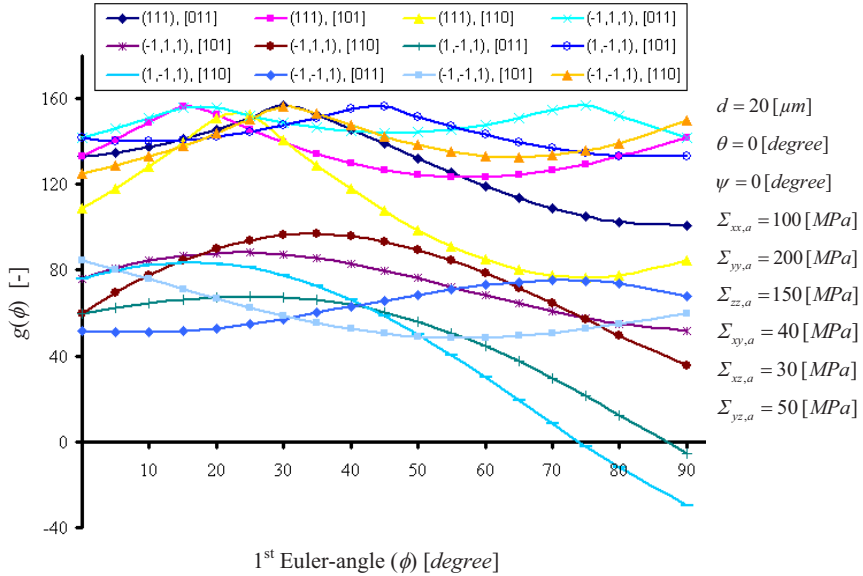


Fig. 4.5. Failure function $g(\phi)$ versus first Euler-angle for all slip systems of Ni.

4.2 Probabilistic study of parameters and corresponding numerical tools

In the previous examples the failure function was utilized for a deterministic description of the HCF failure in individual grains. However, in a random agglomerate of grains the parameters are not known for each individual grain and the failure probability is determined by equally significant contributions of several random variables. In that case, the HCF failure probability can be evaluated, if the stochastic distributions of variables are given for the aggregate of grains. The evaluation of the failure probability for random variables with given distributions is then performed by reliability methods.

Instead of the well-known Monte Carlo simulations, where a large number of random experiments are performed and the outcome leads to an estimation of the failure probability, we chose the first- and second-order reliability methods (FORM and SORM) because of their computational effectiveness, and since

they also generate sensitivity information with respect to the random input variables [76, 82].

For this work, the ZERBERUS code is utilized to calculate the HCF probability, for the cases where parameter distributions are given for the microstructure. This code includes a general-purpose core implementing the FORM and SORM in probabilistic fracture mechanics (PFM) [83]. For using the code, a deterministic user-supplied failure function, as described in Eq. 51, is needed. The variables and constants of the failure function are defined as inputs of the code. For random input variables, the distribution type (Weibull, Gaussian, exponential...) is selected and the distribution parameters are provided. From these input quantities, the code calculates the failure probability as well as sensitivity factors of the failure probability with respect to each variable. For parameter study with ZERBERUS, the grain size d , Euler-angles (ϕ, θ, ψ) , and the critical limit Γ_c of accumulated plastic shear strain are used as random variables, and material parameters k , h , and τ_y^∞ as deterministic constants of the failure function $g(d, \phi, \theta, \psi, \Gamma_c)$. The microstructure data of Ni micro-samples (which will be described in chapter 5) are applied as input of the code. For that purpose the grain size and grain orientation (3 Euler-angles) are measured on the surface of the samples with electron backscatter diffraction (EBSD) method. Subsequently these data are evaluated with Mathematica [84] to find the best-fitting type of stochastic distribution and corresponding parameters for the description of grain size and grain orientation. The distribution types and parameters for each random variable of the failure function are listed in Table 4.2. The distribution parameters for the grain size and grain orientation are obtained from a database of EBSD data for 549 surface grains of a Ni sample. The data of the grain size and grain orientation presented the best-fitting to a Weibull distribution.

The critical limit of the accumulated plastic shear strain, Γ_c , is modeled as a random variable in the range between 70 and 130. For description of this variable a Weibull distribution was chosen for convenience and only to reflect statistical uncertainty of Γ_c ; a Gaussian distribution with corresponding mean and standard deviation would have a very similar shape in the selected variable range. For the distribution parameters, a median value of 96.96 (scale parameter=100, see Table 4.1) and an assumed coefficient of variation of 10%

(i.e. a shape parameter of 11.88) are chosen. Material parameters of Ni are applied as described in Table 4.1.

By means of the ZERBERUS code, the HCF probability was evaluated for different slip systems considering a bending stress with an amplitude of 190 [MPa] acting in longitudinal direction of the sample ($\Sigma_{yy,a}$). Furthermore, the sensitivity of the failure probability with respect to each variable is calculated, as illustrated in Table 4.3. The results of sensitivity analyses are visualized in Fig. 4.6 as pie charts.

The sensitivity of the failure probability with respect to the Euler-angles (Var. 2-4), specifically with respect to the first angle (Var. 2), is significantly higher than with respect to the grain size and the critical limit of accumulated plastic strain.

However, it has to be noted, that the values of sensitivity are depending on the load condition and on the considered slip system. The low sensitivity of the failure function with respect to the grain size and also the high sensitivity with respect to the first Euler-angle are in agreement with the previous considerations about the failure function as shown in Fig. 4.1 and Fig. 4.2.

The presented results of the parameter study and also the predictive power of the failure function will be seen in chapter 6 to be in agreement with experiment results.

Table 4.2. Types and parameters of stochastic distributions for different variables of Ni sample.

Variable		Distribution type	First distribution (scale) parameter	Second distribution (shape) parameter	Lower limit of variable	Upper limit of variable
No.	Definition					
Var. 1	Grain size $d [\mu m]$	Weibull	17.21	1.98	1	100
Var. 2	First Euler-angle $\phi [^\circ]$	Weibull	204.64	1.70	0	360
Var. 3	Second Euler-angle $\theta [^\circ]$	Weibull	35.28	3.28	0	180
Var. 4	Third Euler-angle $\psi [^\circ]$	Weibull	51.83	1.83	0	360
Var. 5	Critical limit of accumulated plastic shear strain $\Gamma_c [-]$	Weibull	100	11.88	70	130

Table 4.3. Sensitivity of failure function to each variable and HCF failure probability for different slip systems of Ni.

Variable		Sensitivity to variable (%)		
No.	Definition	(-1,-1,1) [101]	(-1,1,1) [110]	(-1,-1,1) [011]
Var. 1	Grain size d [μm]	1.2	0.9	2.3
Var. 2	First Euler-angle ϕ [$^\circ$]	91.2	85.8	87.7
Var. 3	Second Euler-angle θ [$^\circ$]	1.7	0.2	3.1
Var. 4	Third Euler-angle ψ [$^\circ$]	5.2	12.4	5.7
Var. 5	Critical limit of accumulated plastic shear strain Γ_c [-]	0.7	0.6	1.2
HCF probability (%)		37.1	18.2	43.0

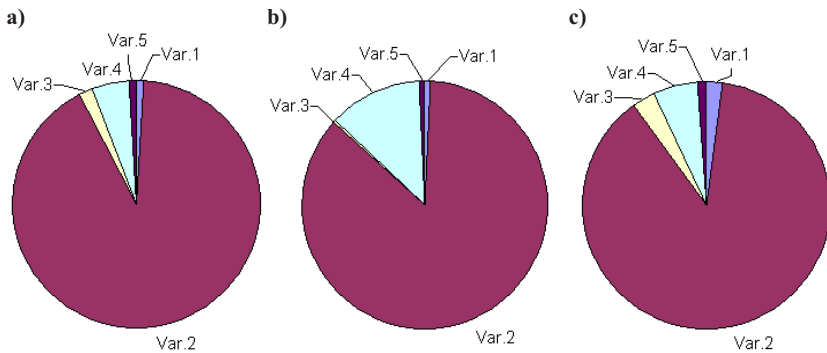


Fig. 4.6. Pie chart for sensitivity of failure function with respect to each variable, for slip systems of Ni; a) (-1,-1,1) [101], b) (-1,1,1) [110], c) (-1,-1,1) [011].

5 HCF experiments with micro-samples

To verify the predictive power of the HCF model, fatigue experiments are performed on micro-samples and the occurrence of micro-damage is compared with the prediction results obtained for each grain on the specimen surface.

The fatigue experiments on micro-samples were performed with a custom-built test setup based on resonance principle. Life times between 10^6 and 10^8 cycles were typically obtained in the experiments.

Occurrence of micro-damage (related to the HCF mechanisms) on the surface of the samples is examined during and at the end of the experiments with scanning electron microscope (SEM), focused ion beam (FIB), or optical microscope.

Grains located on the surface of the samples are analyzed with EBSD, and a mapping program is applied to measure the grain size and grain orientation (Euler-angles), as input parameters of the failure function.

In the next sections the details of the experimental approach and the analysis procedure are given.

5.1 Custom-built test setup⁸

Fatigue experiments on micro-parts are delicate due to small dimensions of the samples and more sensitivity to the handling. To avoid possible damage of the samples, their positioning and fixing should be done carefully, and physical parameters should be measured preferably with contact-less methods. Since the parts are tiny, applied mechanical forces and displacements are very small, and therefore precise methods are required to measure those parameters. A proper

⁸ The custom-built test setup for fatigue experiments and related test method were developed by T. Straub in his dissertation work [85-86]. One part of the fatigue experiments performed by him and his team had been planned for this dissertation, and the samples were used after fatigue experiments for characterization analyses and verification of the failure function in this work. Hence both dissertations could supplement each other.

method for imposing cyclic loading on micro-samples is stimulation of the parts at their resonance frequencies (e.g. with piezoelectric actuators), so that higher stress amplitudes are induced in the sample (despite low excitation displacements) and the testing time is reduced, which is an important aspect for HCF testing [87].

The working principle of the custom-built test setup, applied for HCF experiments on micro-samples, is illustrated in Fig. 5.1. One end of the sample is fixed by a clamp and the second end is free to oscillate as inertial mass. The narrow gauge section is in the middle of the sample between these two ends. The clamp side of the specimen is connected to a spring, and two independently controlled piezoelectric actuators can displace the spring, leading to the excitation of the sample at the free end. In-phase excitation of the piezoelectric actuators induces a bending load on the sample (Fig. 5.2a), an anti-phase excitation causes a torsional load (Fig. 5.2b), and out-of-phase excitation leads to multiaxial loading. Each piezoelectric actuator has a displacement range of 60 nm and a resolution of 1.2 nm (Physik Instrumente, Germany) [85, 87].

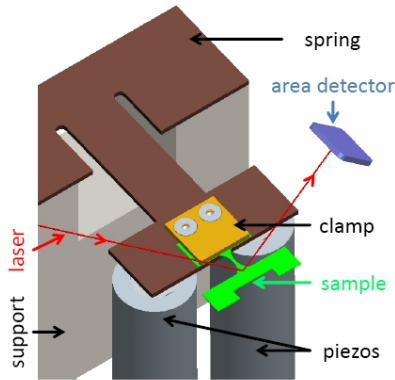


Fig. 5.1. Working principle of the test setup for HCF experiments on micro-samples [85].

Displacements of the sample due to the bending or torsion are measured via a laser beam reflected from the surface of the sample to an area detector. The area detector is a position sensitive device (PSD), with an optical resolution of $1\ \mu\text{m}$ (Fig. 5.3). The induced bending and torsion stresses in the sample can be

calculated using the measured displacements. The data acquisition and controlling of the test setup is performed by a field programmable gate array (FPGA), having analogue input channels with a sampling rate of 750×10^3 samples/s and analogue output channels with 10^6 samples/s [85].

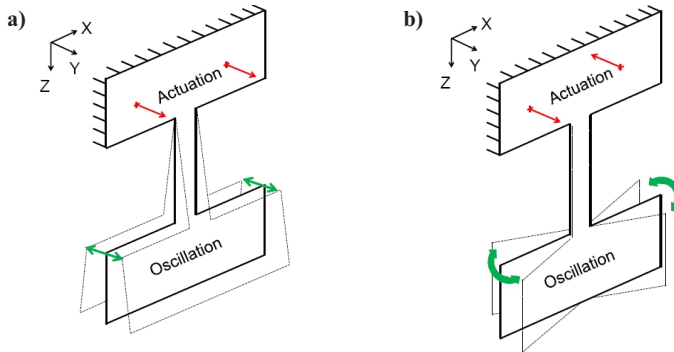


Fig. 5.2. Actuation and oscillation principle of samples at a) bending, b) torsion mode [85].

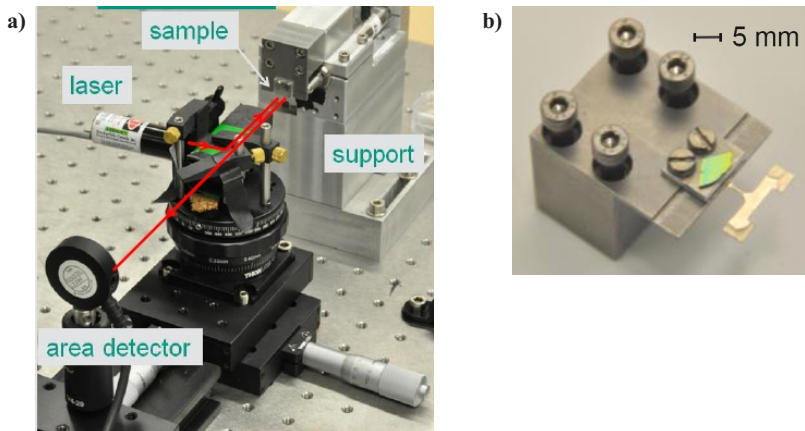


Fig. 5.3. a) Test setup for HCF experiments on micro-samples, measurement of the sample displacements via laser beam, b) micro-sample fixed in the clamp [85].

5.2 Geometry design of micro-samples⁹

Samples should be designed in a way that from one side they could be used with the illustrated resonance principle and on the other hand the results of the HCF experiments should be applicable for verification of the presented micro-mechanical model. For design of the samples and corresponding evaluation of the micro-mechanical HCF model, some aspects need to be considered:

- a) resonance frequencies of the samples in bending and torsion should be in frequency range of the test equipment.
- b) maximum stress induced by uniaxial or multiaxial loading should be located in the gauge section of the sample, where a post-test analysis of micro-damage (occurring during the fatigue experiment) is to be performed.
- c) maximum stress should occur on the surface of the sample, since only for surface grains their size and orientation can be measured with EBSD. Furthermore, occurrence of micro-damage, e.g. extrusions and intrusions related to persistent slip bands (PSBs), or micro-cracks, can be observed on the surface of the sample simply by means of non-destructive methods, as SEM or optical microscopy.
- d) sharp corners should be avoided in the samples, in order to prevent the stress concentration in those areas. Stress concentration can lead to fatigue crack initiation in the areas of the samples which are not under observation.

Taking into account the above mentioned aspects, three main regions are considered in geometry design of the samples:

- 1) the clamped side, which is used to fix the sample in the fixture of the test equipment and excite it from this side.
- 2) the gauge section, which is the narrow part in the middle of the sample with a typical length of 5 mm.

⁹ The design and optimization of samples were performed by T. Straub [85-86]. Here an introduction to the design process has been given. Furthermore some results of FE simulation carried out in this work are presented. Readers are referred to [85-86] for more details on geometry design of samples.

- 3) the oscillating inertial mass, which is located in the free end of the sample and can oscillate due to the excitation caused by piezoelectric actuators. Due to the reciprocating displacements of the inertial mass, cyclic stresses are induced in the gauge section.

The geometry of the inertial mass has significant influence on the resonance frequency and vibration mode shapes of the sample. The geometry is rectangular for uniaxial bending experiments, while for uniaxial torsion or multiaxial loading (combined bending and torsion) twin inertial masses are preferred. Initial design of a twin mass model is illustrated in Fig 5.4; two masses at both sides of the gauge section lead to higher displacements and consequently higher stresses under bending and torsional loads. Dimensions of the samples are designed with the aim of FE simulations, so that the resonance frequencies in bending and torsion modes coincide as much as possible. The specimen design in Fig. 5.4 has a resonance frequency of 734 Hz in uniaxial torsion mode and 740 Hz in uniaxial bending mode. The main disadvantage of this design is the stress concentration at sharp corners between gauge and clamped sections. Fig. 5.5 shows the bending stresses in this design (calculated by FE simulation), if the free end of the twin inertial masses is displaced 50 μm in the z-direction.

A classical method to reduce the stress concentration is to change the geometry from sharp corners to chamfers or rounded corners (e.g. fillets). Fig. 5.6 depicts the bending stress under similar load condition as in Fig. 5.5; however, shoulder fillets with a radius of 0.45 mm were added to the corners. Hence the maximum bending stress is reduced from 178 MPa to 139 MPa and moved from corners towards the gauge section. Nevertheless, this maximum stress is still in the vicinity of the notch region at the specimen shoulder, while maximum stress due to bending should occur on the upper or lower surface of the gauge section (considering it as a cantilever beam).

To solve this problem the geometry of shoulder fillets needs further optimization, in the way that the stress concentration is avoided and the maximum stress due to the bending stress occurs in the middle of the gauge section. For this purpose the tensile triangle method is used in this work [89-90]. Details of this optimization method are illustrated in Appendix A2.

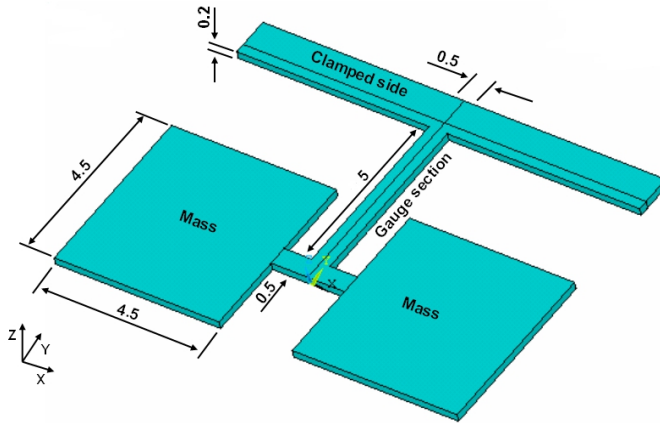
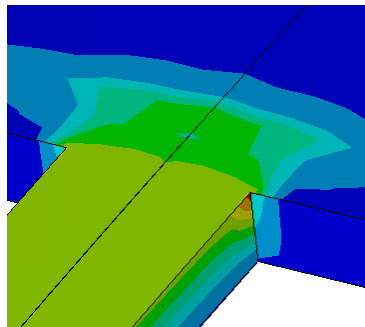


Fig. 5.4. Model of the twin inertial masses with non-optimized sharp corners (between gauge section and clamped section). Dimension unit: [mm]. Reference for the model: [88].



Material data (steel):

$$E = 210 \times 10^9 \text{ [Pa]}$$

$$\nu_{xy} = 0.33$$

$$\rho = 7800 \text{ [kg/m}^3\text{]}$$

$$\Delta z = -50 \text{ [\mu m]}$$

$$\sigma_{yy, \text{max}} = 178 \text{ [MPa]}$$

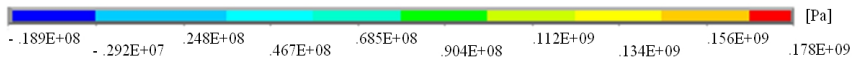


Fig. 5.5. Model with non-optimized sharp corners: bending stress at the shoulder due to a vertical displacement of 50 μm (at the free end of the twin inertial masses).

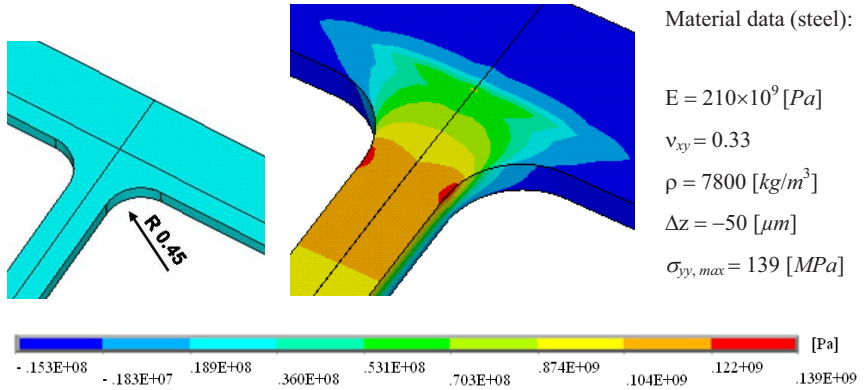


Fig. 5.6. Bending stress at the shoulder due to a vertical displacement of $50 \mu m$ (at the free end of the twin inertial masses). Model has shoulder fillets with a radius of 0.45 mm .

The previous twin mass design (Fig. 5.4) is optimized with tensile triangle method with three different sets of fillet radii as shown in Fig. 5.7, and each time the bending stress is simulated with FE under the same load condition as in Fig. 5.5. The method demonstrates considerable improvements in reduction of the stress concentration, if proper set of fillet radii is selected. With the third set of fillet radii (Fig. 5.7.c) no stress concentration is observed in the shoulders and the maximum stress is decreased significantly, down to the level of the pure bending stress. The location of maximum stress is moved from shoulder toward the midpoint of the gauge section, and it extends at a larger area at the topside of the gauge section compared to the initially localized stress concentration at the sharp corners. So the stress concentration is avoided with iterative optimizations of the fillet radii.

The next optimization on the specimen design, shown on Fig. 5.4, is to strengthen the small connecting beam between the two inertial masses to avoid the twisting of the masses around the beam. Fig. 5.8 depicts a simplified optimized geometry with two wings at the sides, which have similar function as twin inertial masses. The beam connecting the two masses has now a larger area, which prevents the twisting of the wings around the beam.

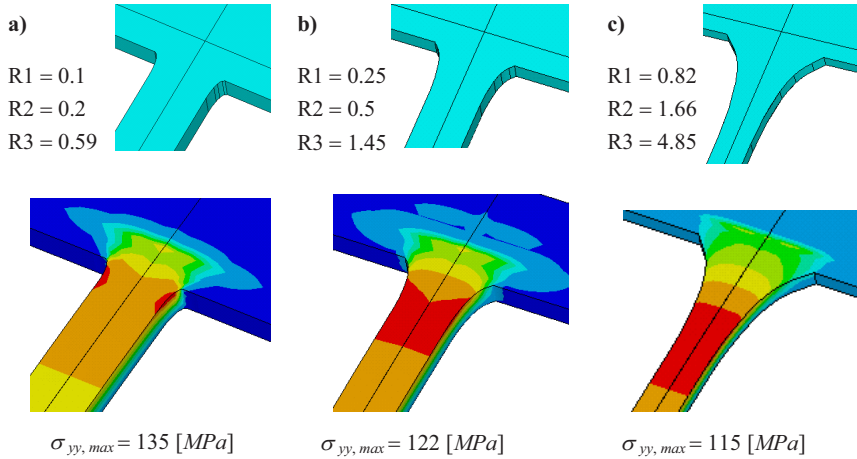


Fig. 5.7. Optimization of twin mass model with tensile triangle method, with three different sets of fillet radii (a, b, and c). Dimension unit in [mm]. Calculation of bending stress with FE simulation. Load condition and material parameters as in Fig. 5.6.

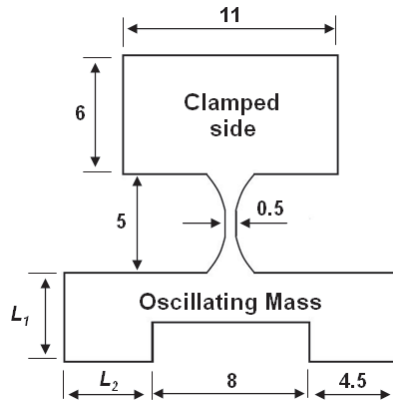


Fig. 5.8. Optimized geometry of micro-samples for multiaxial HCF tests. Dimensions are in [mm]. $L_1=L_2=4.5$ mm. References for the drawing and geometrical data of the samples are [85, 88], with some small modifications.

The last step in optimization of the specimen design is adjusting the geometry of the oscillating inertial twin masses, in the way that the resonance frequencies in uniaxial bending and torsion are close to each other. For that purpose two parameters are considered in the design: length L_1 and L_2 (Fig. 5.8). Increasing of length L_1 or L_2 leads to the reduction of the resonance frequencies in bending or torsion, respectively. The optimization of length L_1 and L_2 is performed with the aim of FE simulations. Assuming $L_1=L_2=L$, the value of L is varied in FE simulation and the corresponding resonance frequencies in bending and torsion modes are calculated. The results of those calculations are illustrated in Fig. 5.9. For small values of L , the resonance frequency in torsion is significantly higher than in bending. Towards larger values of L , the decrease in the torsional resonance frequency is more pronounced than in the bending resonance frequency. The two curves for the bending and torsion modes intersect at a resonance frequency of 460 Hz, and the corresponding length of $L=4.5$ mm was used for specimen fabrication [85].

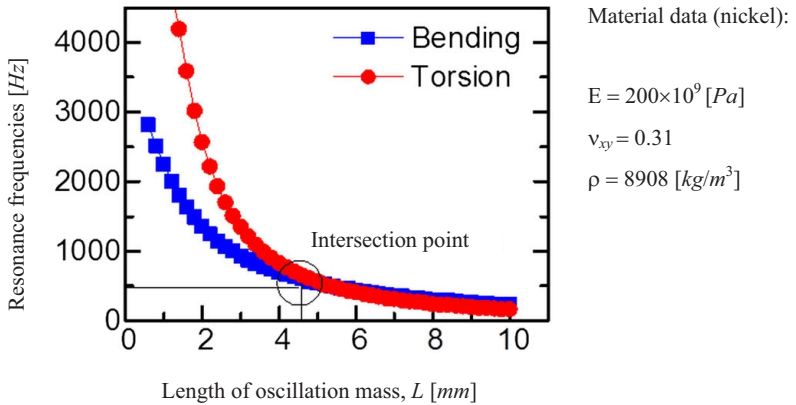


Fig. 5.9. Optimization of length L for equal resonance frequencies at bending and torsion modes. Reference of the diagram is [86], with some small modifications.

5.3 Material selection and preparation of micro-samples

Results of HCF experiments for micro-samples of nickel, copper, and aluminum were used. These materials are utilized broadly in microelectronic components and MEMS (e.g. in wire bonds, electrical terminals and leadframes), where they are exposed to thermo-mechanical stresses and vibrations, resulting in material fatigue [91-92].

Copper and aluminum specimens turned out to be not suitable for EBSD surface analysis. Due to high surface roughness of the copper samples, the surface grains could not be mapped properly in EBSD measurements. On the other hand, aluminum samples had a good surface quality for EBSD measurements; however, due to the large grain size (3-5 grains in the width of the gauge section) it was not possible to collect a reasonable amount of data from the surface grains. Therefore most of the HCF experiments were performed on nickel samples, where both surface quality and grain size were well suited for EBSD analysis purposes.

The nickel micro-samples were laser-cut from annealed foils having a thickness of 200 μm and 99.0% purity (Goodfellow, UK). The gauge section had a rectangular cross section of 500 μm by 200 μm (according to the geometry of Fig. 5.8). The nickel samples had an average grain size of 20 μm . The gauge section together with some regions of the inertial mass and clamped side near the gauge section was electro-polished. The electro-polishing improves surface reflection of the laser beam for measurement of the displacements of the sample [85]. Fig. 5.10 shows one of the Ni-samples before and after electro-polishing.

The applied methods for surface analysis of the grains after HCF experiments with respect to microstructure (e.g. grain size and grain orientation) and micro-damage are described in the following sections 5.4 and 5.5.

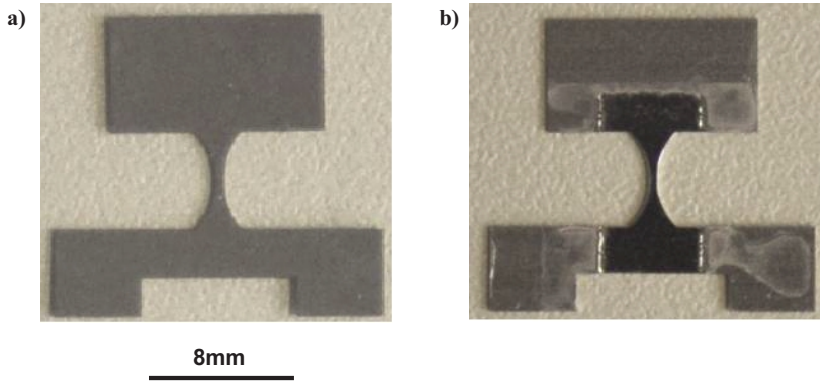


Fig. 5.10. Ni-sample: a) before electro-polishing, b) after partial electro-polishing: surface roughness reduced for better reflection of the laser beam [88].

5.4 Measurement of grain size and grain orientation with EBSD

In the definition of the failure function (Eq. 51), it was stated that the grain size and grain orientation (Euler-angles) are two important input variables of this function for describing the grain microstructure. In this work, EBSD¹⁰ is used to analyze the grains located on the surface of the sample. After the EBSD analysis, the mapping program HKL CHANNEL 5 [73] was used to map the grain size and grain orientation (Euler-angles).

According to FE simulation results in section 5.2, the maximum von-Mises stress (and also maximum bending stress) occurs at a region near the midpoint of the gauge section, where most of the micro-damage evolves during HCF test.

¹⁰ By means of the EBSD (electron backscatter diffraction), which is applied together with the scanning electron microscopy (SEM), the orientation of individual grains, local texture, and phase distributions can be determined on the surfaces of bulk polycrystals [74]. Readers are referred to [73-75] for more details on working principles, applications, and experimental setup of the EBSD analysis.

Therefore this region was analyzed with EBSD, to gain a reasonable amount of data from grains exhibiting micro-damage.

Fig. 5.11 shows the SEM micrograph of the surface of a Ni-sample (left) together with the EBSD map of the grains (right) located in the region with the most micro-damage. The dark gray color (in the left micrograph) indicates the region of the EBSD analysis. EBSD maps help to recognize the grain borders and visualize different grain orientations.

The small white spots in EBSD map (Fig. 5.11) are indicating the points, where EBSD could not successfully identify the grain orientation. The reason for that can be roughness of the sample surface, affected by material defects, the fabrication process of the foils, or micro-damage evolved during the HCF experiment. The mapping program HKL CHANNEL 5 has mapped these spots to individual grains of a very small grain size. To avoid these artifacts, grains smaller than 6 μm have not been considered in the later analysis of the grains (with failure function).

For comparison, Fig. 5.12.a shows the EBSD map of the surface grains for a copper sample. Due to the relative high roughness of the surface, the EBSD mapping could not recognize the size, orientation, and borders of the grains correctly. Even in SEM micrographs (e.g. Fig. 5.12.b) the grains can not be distinguished from each other properly.

After successful surface analysis, the data of grain size and Euler-angles obtained by EBSD mapping are introduced into Eq. 51 and the failure function for all slip systems of each grain is evaluated. In a subsequent step, the predictions of the failure function need to be compared with the observed micro-damage in the grains. The next section illustrates the procedure for the surface analysis of the micro-damage in the grains.

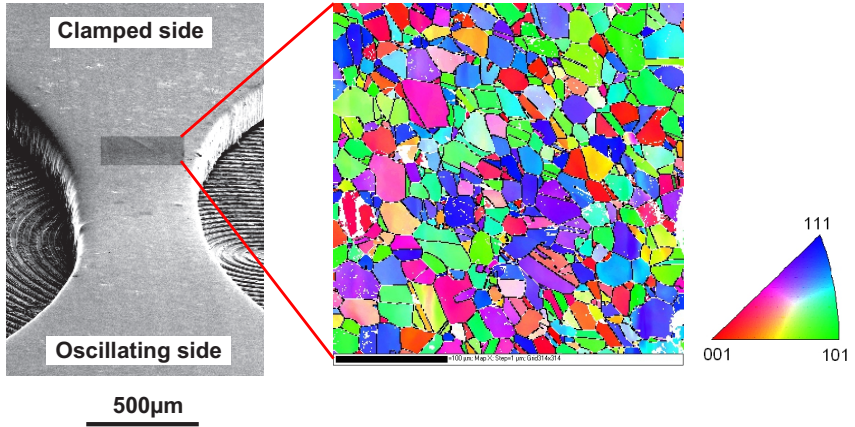


Fig. 5.11. EBSD analysis of surface grains of a Ni-sample; left: SEM micrograph of the scanned area, right: EBSD map of grains (mapping to 1st Euler-axis) and legend of IPF (inverse pole figure) coloring.

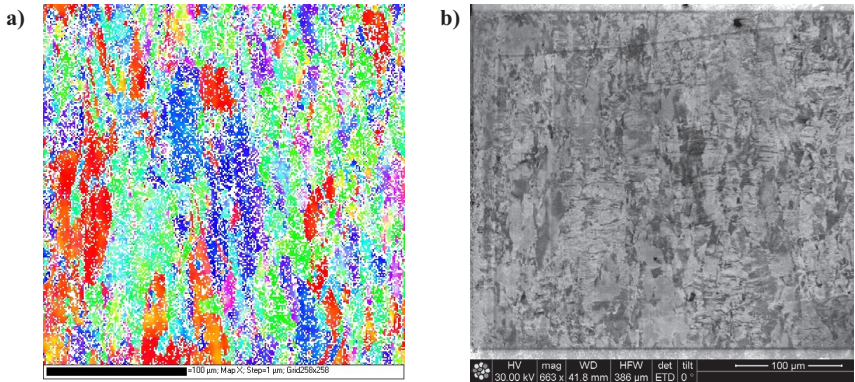


Fig. 5.12. Surface analysis of Cu-sample after HCF experiment: a) EBSD map of grains (mapping to 1st Euler-axis), b) SEM micrograph of grains (after 3.4×10^6 cycles of uniaxial reversed bending with amplitude of ± 164 MPa). In both micrographs the grains and their borders are not identified clearly.

5.5 Analysis of surface damage

To verify the evolution of micro-damage due to the cyclic loading, the samples were inspected before and during HCF experiments with ultraviolet laser scanning microscopy. At the end of HCF experiments, the surface of each grain was analyzed with SEM and EBSD for the occurrence of micro-damage. For further inspection of the damage, in some cases FIB cross sections were taken to assess the depth and extent of the damage inside the grain or in the neighboring grains.

At the beginning of the load cycling (or at low stress amplitudes) smooth straight markings were observed on the surface of some grains due to the extrusions and intrusions caused by the cyclic plastic strains in slip bands of the grains (Fig. 5.13). The surface markings were parallel to each other inside each grain, in agreement with the assumption stated previously that just one slip system is activated in HCF regime. With continuing cyclic deformation (and in some cases facilitated with increase in stress amplitude), the surface markings and corresponding protrusions evolved gradually in the form of surface micro-damage, representing the localization of plastic strains along PSBs (Fig. 5.14). Further cyclic loading enhances such micro-damage and leads to the initiation of micro-cracks inside the grain and parallel to the PSBs (Fig. 5.15 and Fig. 5.16). Therefore, grains exhibiting such kind of micro-damage are considered here as non-safe and prone to HCF failure [93-94]. During surface inspection of the samples, it is verified for each grain, if micro-damage has occurred or not.

In chapter 6, the results of surface inspection for each sample are illustrated and it is discussed to which extent the failure function was able to predict the occurrence of micro-damage in individual grains.

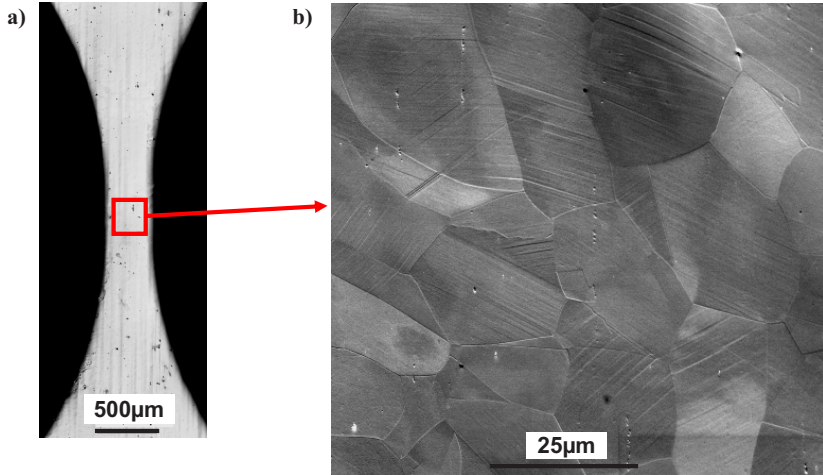


Fig. 5.13. Surface inspection of a Ni-sample (10^7 cycles; uniaxial reversed bending with an amplitude of ± 150 MPa): a) ultraviolet laser scanning micrograph of the sample [88], b) SEM micrograph of the surface showing straight and smooth markings (extrusions and intrusions).

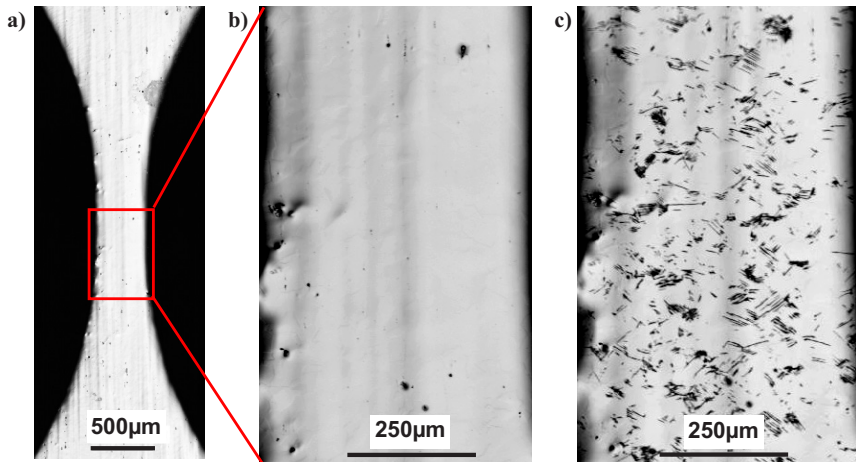


Fig. 5.14. Ultraviolet laser scanning micrographs from the surface of a Ni-sample [88]: a) and b) gauge section of the sample before HCF testing, c) micro-damage (extrusions and intrusions) occurred during HCF testing (4×10^6 cycles of uniaxial reversed bending with an amplitude of ± 200 MPa).

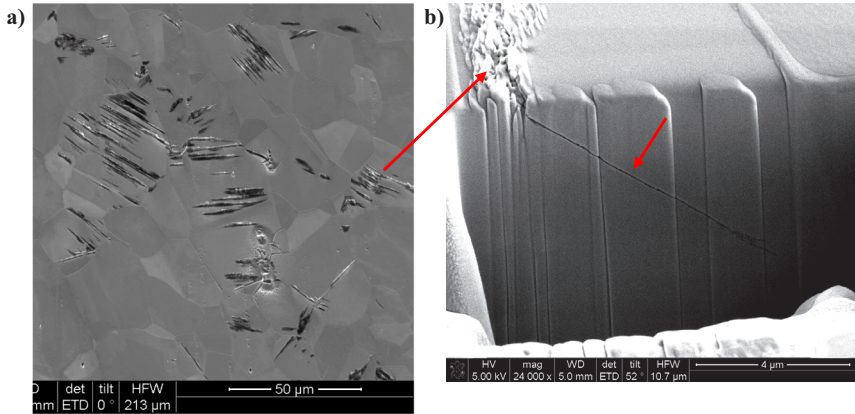


Fig. 5.15. Surface inspection of a Ni-sample after an HCF experiment (4×10^6 cycles of uniaxial reversed bending with an amplitude of ± 200 MPa): a) SEM micrograph of grains exhibiting micro-damage (extrusions and intrusions), b) FIB cross section of a damaged grain showing a micro-crack initiated from surface protrusions.

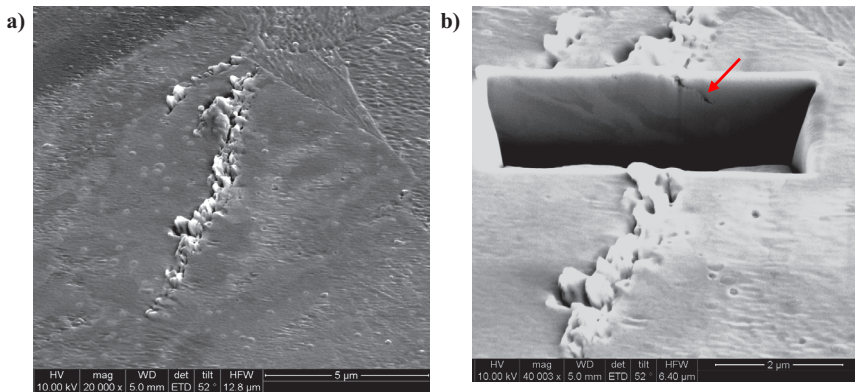


Fig. 5.16. Surface inspection of a Cu-sample after an HCF experiment (after 3.4×10^6 cycles of uniaxial reversed bending with an amplitude of ± 164 MPa): a) SEM micrograph of a grain exhibiting micro-damage (extrusions and intrusions), b) FIB cross section of the damaged grain showing a micro-crack initiated from surface protrusions. Reference of micrographs: [88].

5.6 Performing of HCF experiments under bending load

The idea behind the HCF experiments is to examine the occurrence of the failures in individual grains during and after the experiments, and compare those failures with the predictions made by the failure function (Eq. 51). Therefore, a proper range of the stress and number of load cycles to failure should be found, which lead to the failure of a few grains. In this regard, some preliminary experiments with different range of stresses and load cycles were performed to establish the S-N diagram of Ni in the HCF regime. Fig. 5.17 illustrates the S-N diagram of the Ni-samples with the design given in Fig. 5.8, covering the HCF regime and also extending into the very high cycle fatigue (VHCF) regime. The tests were performed with the custom-built test setup under uniaxial fully reversed bending (Fig. 5.3). The points shown in the S-N diagram do not correspond to the rupture of the whole sample (due to propagation of macroscopic cracks) but failure of some grains, which suffer localized plastic strains along PSBs, resulting in micro-cracks. Those plastic deformations cause changes in mechanical properties of the material, e.g. the elastic modulus or stiffness [86, 95], affecting subsequently the resonance frequency of the sample. In HCF experiments, the first micro-cracks could be revealed by FIB cross sections, after the resonance frequency of the sample was reduced about 0.2% from the initial value (before the HCF experiment), and the sample was thus identified as failed in the HCF experiment [86].

The S-N diagram in Fig. 5.17 presents similar behavior as data reported in literature, where there is no definite endurance limit at higher cycle numbers. The endurance limit is recognized, e.g. for ferrous materials, as a change in the slope of the S-N diagram from negative to zero (flat). For fcc metals, e.g. nickel, the S-N diagram does not have zero slope at long lives, nevertheless it exhibits a gradual flattening between 10^7 and 10^8 cycles, and it is common to speak of the endurance limit in this range of cycle numbers [96].

According to the S-N diagram (Fig. 5.17), stresses lower than 80 MPa correspond to the endurance limit, which is the working regime of the failure function. Since in this stress range theoretically no micro-damage is expected in the individual grains, it is difficult to verify the prediction power of the failure

function. Hence for HCF testing of micro-samples a stress range somewhat higher than the endurance limit was selected in order to have at least a few grains damaged during the fatigue experiment.

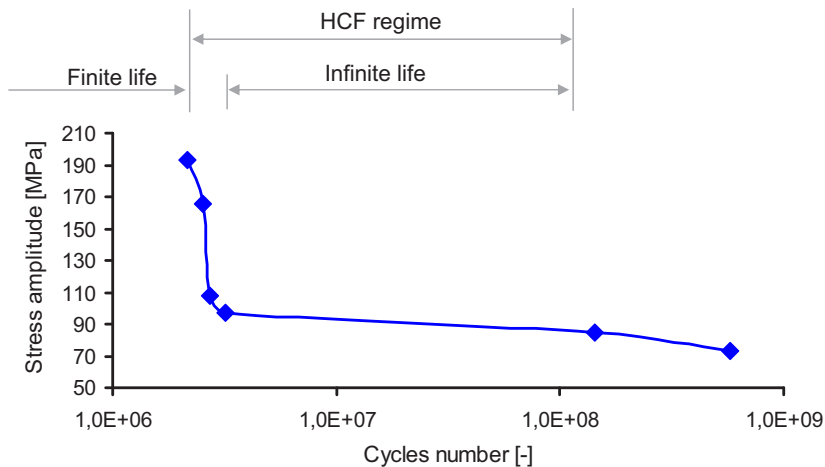


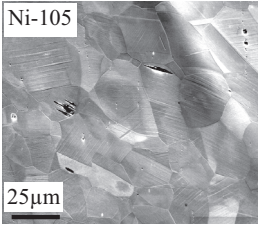
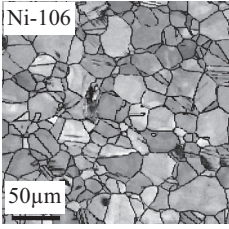
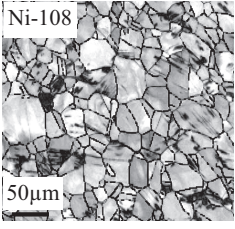
Fig. 5.17. S-N diagram of Ni-samples under uniaxial fully reversed bending. Reference for raw data used in the diagram: [88].

First, a uniaxial bending stress of ± 150 MPa was selected, and for subsequent Ni-samples the stress amplitude and test duration were varied to verify the influence of these parameters on the evolution of micro-damage and also to assess the prediction power of the failure function for different loading conditions. Table 5.1 summarizes the load conditions for five samples along with micro-graphs of surface damage after corresponding HCF experiments.

With increasing of the stress amplitude and test duration more micro-damage is observed on the surface of samples. In sample No. Ni-105, smooth straight surface markings are visible which are caused by extrusions and intrusions related to the dislocations in the slip bands. The surface markings are distributed over the whole surface area of the grains, and the plastic strain is not localized yet in PSBs (except in some rare cases). For samples No. Ni-106 and Ni-107, the stress amplitude was increased to ± 200 MPa, and micro-damage due to localized plastic strains along PSBs is observed in some grains even after 2×10^6

cycles. By keeping the same stress amplitude and extending the test duration to 4×10^6 cycles, the micro-damage evolved in more grains, as noticed in samples No. Ni-108 and Ni-109.

Table 5.1. Load conditions for HCF experiments of Ni-samples and surface micrographs (SEM, EBSD) of the samples after the test.

Sample No.	Ni-105	Ni-106 Ni-107	Ni-108 Ni-109
Stress amplitude [MPa]	Uniaxial fully reversed bending ± 150	Uniaxial fully reversed bending ± 200	Uniaxial fully reversed bending ± 200
Number of cycles	10^7	2×10^6	4×10^6
Surface micrograph			

In the next chapter, the surface inspection results of samples No. Ni-105, Ni-106, Ni-107, and Ni-108 will be discussed. Since sample No. Ni-109 has similar results as sample No. Ni-108, its results are not discussed in details.

Furthermore, the observed micro-damage will be compared with the predicted results of the failure function for each individual grain.

6 Comparison of theoretical and experimental results

In this chapter, the overall predictions of the HCF model, which grains will be damaged by fatigue, is discussed and backed up with results on fatigue micro-damage of selected individual grains. For that, the experimental results of four Ni-samples (as discussed in the last chapter) are used, and the failure function is calculated for each grain in the sample. Thus, we obtain a classification scheme for all of the analyzed grains in terms of predicted and observed fatigue micro-damage. The possible disagreements between theoretical and experimental results will be discussed for each sample, and based on the post-fatigue investigations the reasons for some of those misclassifications will be assessed.

In the first step, the failure function $g(\cdot)$ is calculated for all slip systems of each grain using Eq. 51. Grain size and grain orientation (Euler-angles) are extracted from EBSD data and taken as input parameters of the failure function. Material parameters of Ni are used according to Table 4.1. The minimum value of the failure function amongst all slip systems of each grain – representing the weakest slip system – is considered for a prediction of grain failure ($g < 0$) or no failure ($g \geq 0$). As a next step, the surface of the grains is inspected with SEM, EBSD, or FIB for presence of micro-damage during HCF experiment. Fig. 6.1 shows typical micrographs of grains with no HCF damage (left) or with HCF damage (right).

In this way, a classification can be made according to the scheme in Fig. 6.2, where two different regions are distinguished: the upper region belongs to the grains, for which the failure function does not predict any HCF damage ($g \geq 0$; safe domain or no failure), and the lower region corresponds to the grains, for which HCF damage is predicted ($g < 0$; failure domain). Depending on agreement or disagreement between predicted results of the failure function and the observed micro-damage, each region corresponds to two groups of grains: those which are correctly classified or those which are possibly misclassified.

Hence, the results for the classified grains can be organized in four different groups:

- 1) Correct prediction of no damage: the failure function has predicted no damage ($g \geq 0$), and the surface inspection with EBSD and SEM did not reveal any micro-damage.
- 2) Incorrect prediction of damage: the failure function has predicted damage ($g < 0$), but no micro-damage was observed during surface inspection.
- 3) Correct prediction of damage: the failure function has predicted damage ($g < 0$), and micro-damage was observed during surface inspection. Micro-damage in those grains was mostly due to extrusions and intrusions.
- 4) Incorrect prediction of no damage: the failure function has predicted no damage for them ($g \geq 0$), however micro-damage was observed during surface inspection.

In the next sections, the theoretical and experiments results of the four Ni-samples No. Ni-105 to Ni-108 are illustrated and the classification of the data according to the above mentioned procedure is performed.

First, the results of samples No. Ni-107 and Ni-106 are discussed, because these samples were both loaded in a moderate bending stress range of ± 200 MPa, causing a reasonable amount of micro-damage during the HCF experiment. Then, the results of samples No. Ni-105 and Ni-108 are discussed, which present a very low and a very high amount of micro-damage due to smaller load or higher number of fatigue cycles, respectively. With the various conditions of these samples, the prediction limits of the failure function for HCF failure shall be verified.

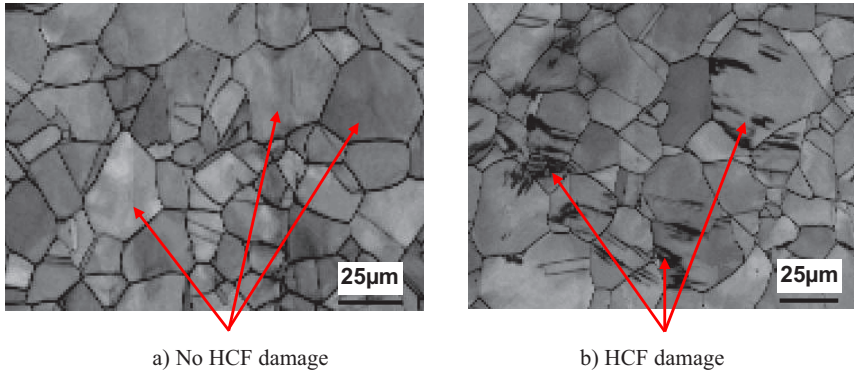


Fig. 6.1. EBSD micrographs of surface grains in sample No. Ni-107 after HCF experiment; a) no HCF damage observed, b) occurrence of HCF damage related to the extrusions and intrusions.

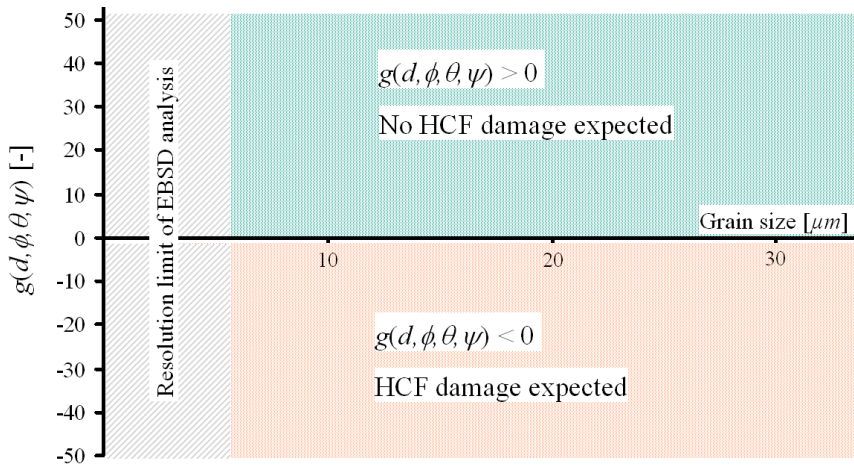


Fig. 6.2. Regions in the diagram of failure function versus grain size for prediction of HCF damage.

6.1 Results of sample No. Ni-107

This sample was exposed to 2×10^6 cycles of uniaxial fully reversed bending with stress amplitude of ± 200 MPa. After that, its surface was inspected with SEM and EBSD. Fig. 6.3 compares the surface of the sample before and after HCF testing; significant amount of micro-damage evolved during load cycling. The micro-damage observed on the surface of the grains is related to the extrusions and intrusions caused by localized plastic deformations along PSBs (Fig. 6.4).

A total number of 520 grains have been analyzed from the surface area scanned by EBSD. Grains smaller than $6 \mu\text{m}$ in diameter are not considered in this analysis due to the measurement limits of the EBSD method. After calculating the failure function for all slip systems of each grain and selection of the related value for the weakest slip system, the results are classified in four groups in the way as described before. In the following the results of each classification group are discussed.

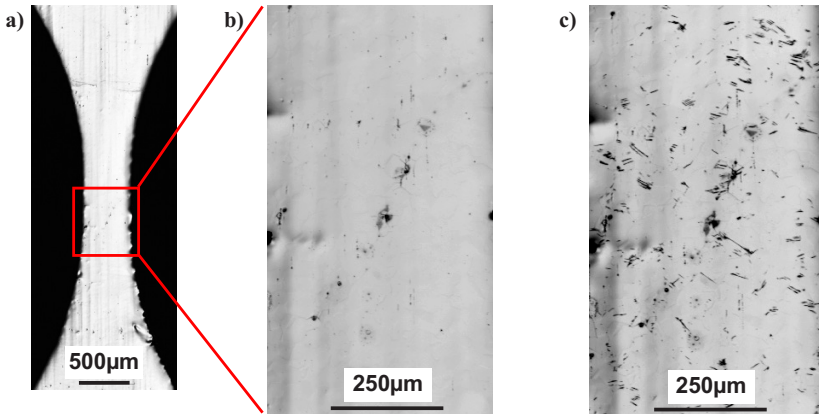


Fig. 6.3. Ultraviolet laser scanning micrographs from surface of the sample No. Ni-107 [88]: a) and b) gauge section of the sample before HCF testing, c) micro-damage that occurred during HCF testing (2×10^6 cycles of uniaxial reversed bending with an amplitude of ± 200 MPa).

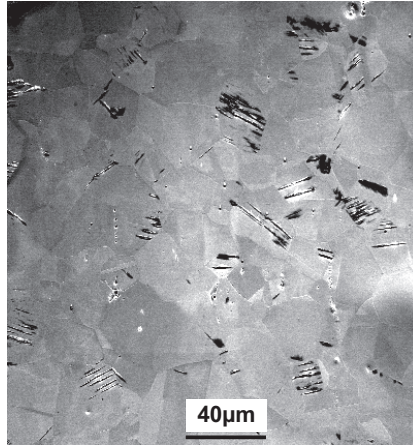


Fig. 6.4. SEM micrograph of the surface of sample No. Ni-107 (after 2×10^6 cycles of uniaxial bending with an amplitude of ± 200 MPa): micro-damage on the surface near the gauge section caused by extrusions and intrusions.

6.1.1 Correct prediction of no damage

The first classification group consists of those grains, for which the failure function has predicted no damage ($g \geq 0$), and the surface inspection with EBSD and SEM did not reveal any micro-damage. Fig. 6.5 shows the failure function versus grain size for the weakest slip system of all the grains classified in the first group. Each point of the diagram corresponds to an individual grain. Since it is a 2D-diagram, Euler-angles of the grains are not shown, although they are considered in the calculations. A SEM micrograph of one surface grain, which is typical for the grains in this group, is shown as inset in Fig. 6.5.

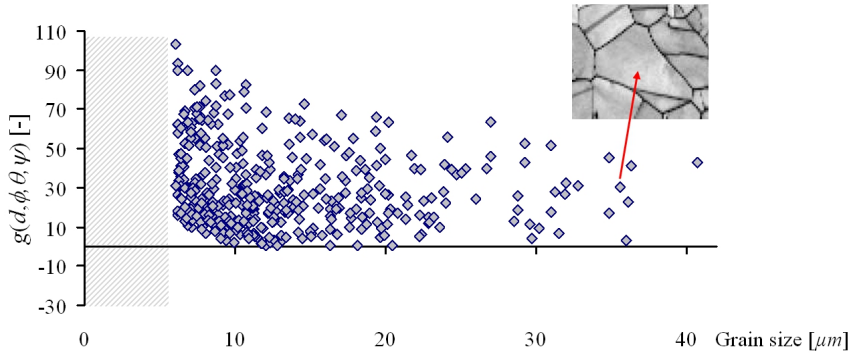


Fig. 6.5. Failure function versus grain size for the weakest slip system of each grain in the first classification group; correct prediction of no damage.

6.1.2 Incorrect prediction of damage

The second classification group consists of those grains, where the failure function has predicted damage ($g < 0$), but no micro-damage was observed during surface inspection. Failure function of those grains versus grain size is illustrated in Fig. 6.6.

To understand the reason of misclassification by incorrect prediction of failure, some of the grains belonging to this group were analyzed in detail. FIB cross sections were cut through the grains perpendicular to the surface in order to locate possible damage inside of the grain (not visible on the surface). The FIB cross sections revealed that in some cases neighboring grains with very similar Euler-angles were considered by the EBSD mapping program as one grain with larger size instead of two smaller neighboring grains. The resulting larger grain size leads to a lower (and possibly negative) value of the failure function and consequently to misclassification as damaged. This case is illustrated in Fig. 6.7, where the EBSD mapping together with the FIB cross section of a mapped grain is shown, confirming that it actually consists of at least three separate grains.

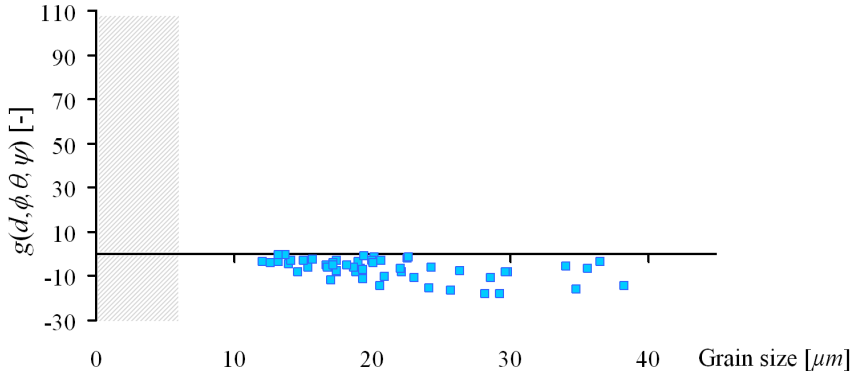


Fig. 6.6. Failure function versus grain size for the weakest slip system of each grain in the second classification group; incorrect prediction of damage.

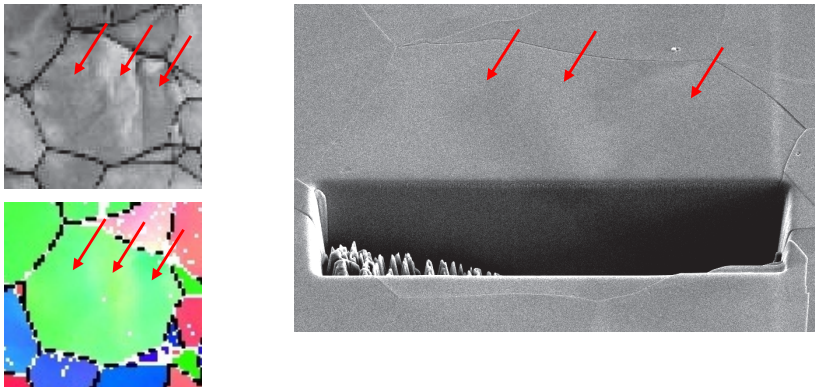


Fig. 6.7. EBSD mapping (left) and FIB cross section (right) of a grain belonging to the 2nd group of classification. No failure inside the grain or on the surface is visible. The mapped grain includes at least three separate grains (shown in dark and light gray colors).

6.1.3 Correct prediction of damage

The third classification group represents the grains, where the failure function has correctly predicted damage ($g < 0$), and micro-damage was in fact observed

during surface inspection. Micro-damage in those grains was caused predominantly by extrusions and intrusions. Fig. 6.8 shows the failure function versus grain size for the 3rd classification group of the grains.

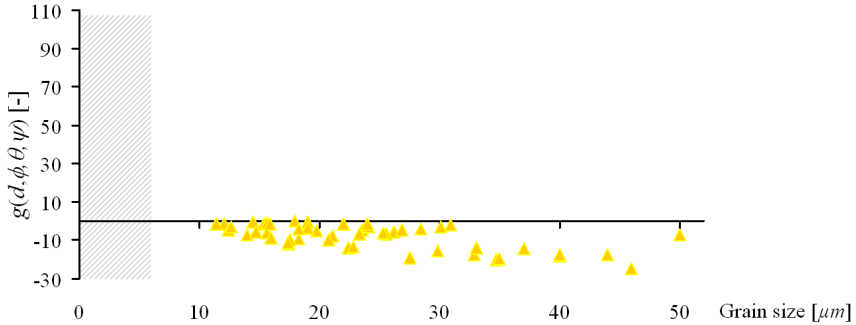


Fig. 6.8. Failure function versus grain size for the weakest slip system of each grain in the 3rd classification group; correct prediction of damage.

6.1.4 Incorrect prediction of no damage

The fourth classification group corresponds to those grains, where the failure function has predicted no damage ($g \geq 0$); while in fact micro-damage was observed during the surface inspection. Fig. 6.9 shows the failure function versus grain size for this classified group of grains. This kind of misclassification is most critical, since grains belonging to this group would be assessed in a non-conservative manner.

For most grains belonging to this group, the failure function has a small positive value and they are most probably misclassified due to the uncertainties in the material parameters or in the experimental characterization of the micro-structural properties. If, for example, a safety factor of only 10% is added to the applied value of the critical limit of the accumulated plastic shear strain Γ_c , then the failure function will be negative for all but one of those misclassified grains, so that there would be practically no misclassifications. For the single remaining grain, which is clearly misclassified (see Fig. 6.9), additional FIB and SEM analyses were performed. These analyses revealed that an adjacent grain exhibits also micro-damage, and the PSBs of both grains meet at the grain

boundary. Fig. 6.10.a shows the EBSD surface scan of both grains. The misclassified grain, with the larger grain size and in the middle of picture, includes some parallel PSBs, and the neighboring grain, the smaller one, has a PSB, which ends at the boundary between the two grains. Fig. 6.10.b and Fig. 6.10.c show the FIB cross sections of the misclassified grain and its neighboring grain, respectively.

Since the failure function evaluates each grain individually and does not model mechanical interaction between neighboring grains, those specific cases are outside the scope of the underlying failure function and are left to a more refined approach.

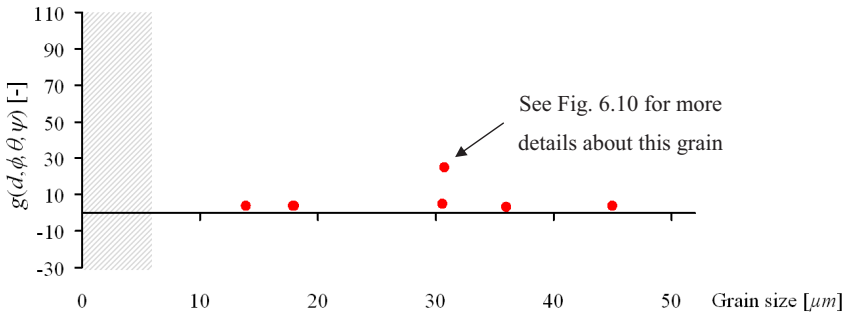


Fig. 6.9. Failure function versus grain size for the weakest slip system of each grain in 4th classification group; incorrect prediction of no damage.

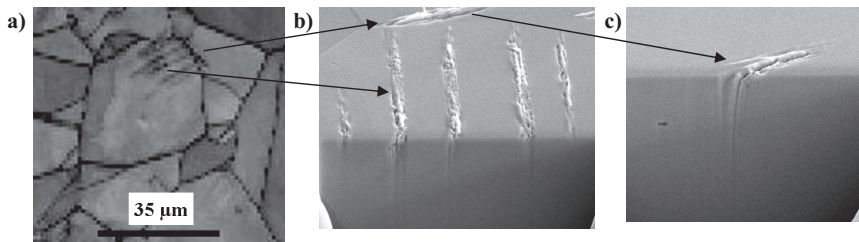


Fig. 6.10. a) EBSD micrograph of the misclassified grain and its neighbor grain, b) FIB cross section of the misclassified grain (incorrect prediction of no damage) including parallel PSBs, c) FIB cross section of the neighbor grain with a PSB ending at the grain boundary.

6.1.5 Summary of results for sample No. Ni-107

The results predicted by the failure function for all four classification groups are summarized in Fig. 6.11, representing results of the 520 grains. It is obvious from the diagram that with increasing grain size the failure probability increases; grains smaller than 10 μm were found not to have any damage. Conversely, for grains larger than 25 μm the relation of damaged grains to non-damaged ones increases. That the smaller grains have higher fatigue resistance is in line with previous work [10-12]. For grains smaller than 10 μm the failure function is very sensitive with respect to variations of the grain size, but for grains larger than 20 μm it becomes quite insensitive with respect to such variations, confirming the previous discussion of the parameter study.

Table 6.1 gives a summary on the predictive power of the failure function. About 90% of all investigated grains are correctly classified. In 10% of the grains, a false prediction of damage was made (classification group 2), and only 1% of grains were predicted incorrectly to have no damage (classification group 4).

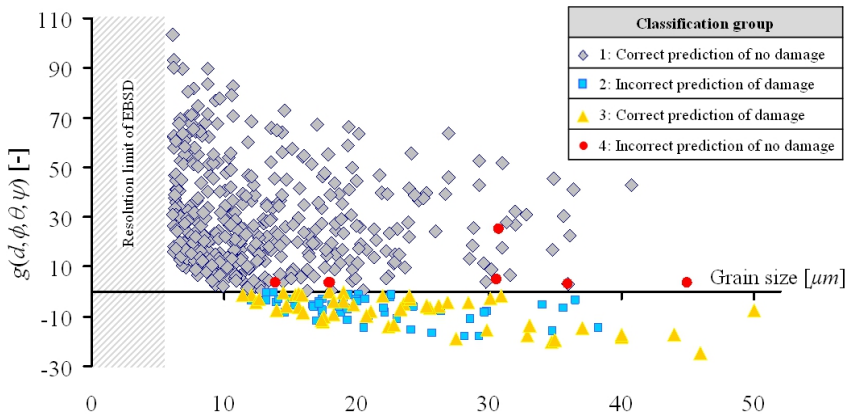


Fig. 6.11. Failure function versus grain size for the weakest slip system of grains of sample No. Ni-107 considering all four classification groups (totally 520 grains presented on the diagram).

Table 6.1. Comparison between predictions of failure function and observed damage in grains of sample No. Ni-107.

Classification group	Failure function	Surface inspection	Number of grains	Percentage of grains [%]
1 correct prediction of no damage	$g \geq 0$ undamaged	No damage visible	411	79
2 incorrect prediction of damage	$g < 0$ damaged	No damage visible	52	10
3 correct prediction of damage	$g < 0$ damaged	Damage visible	50	10
4 incorrect prediction of no damage	$g \geq 0$ undamaged	Damage visible	7	1

6.2 Results of sample No. Ni-106

This sample was tested under the same load conditions as sample No. Ni-107 (2×10^6 cycles of uniaxial fully reversed bending with a stress amplitude of ± 200 MPa), to verify the reproducibility of the results achieved by sample No. Ni-107 with a more comprehensive data base. After testing, the surface of the sample No. Ni-106 was inspected with SEM and EBSD, in the same way as for sample No. Ni-107. Fig. 6.12 shows the surface of the sample before and after HCF testing. The micro-damage related to extrusions and intrusions are shown to have evolved during the load cycling (Fig. 6.13).

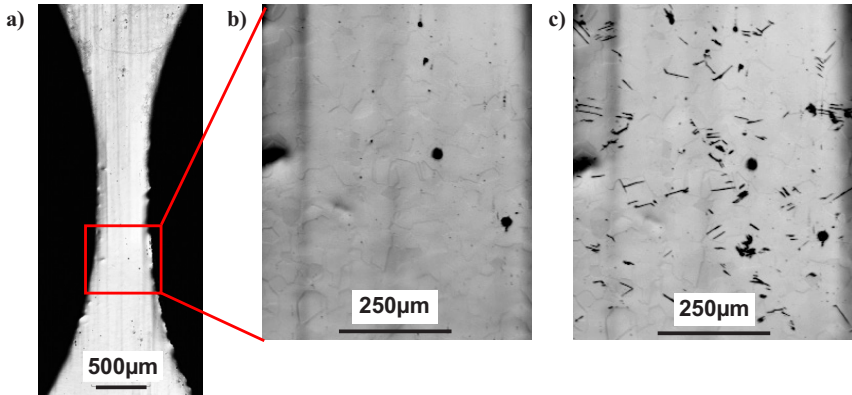


Fig. 6.12. Ultraviolet laser scanning micrographs from surface of the sample No. Ni-106 [88]: a) and b) gauge section of the sample before HCF testing, c) micro-damage that occurred during HCF testing (2×10^6 cycles of uniaxial reversed bending with an amplitude of ± 200 MPa).

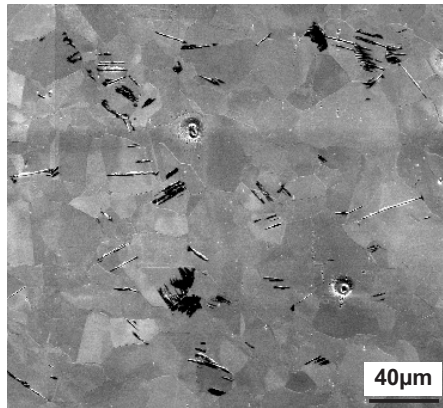


Fig. 6.13. SEM micrograph of the surface of sample No. Ni-106: micro-damage on the surface near the gauge section caused by extrusions and intrusions (after 2×10^6 cycles of uniaxial bending with an amplitude of ± 200 MPa).

The predicted results of failure function versus grain size are shown in Fig. 6.14 for the analyzed area with 220 grains. The classification of the results is performed as described before for sample No. Ni-107. The main characteristics

of the diagram are similar as for sample No. Ni-107; the dependency of the failure function on the grain size as well as the distribution of the grains in the different classification groups are comparable. Five grains were incorrectly predicted to have no damage (4th classification group): two of them have a very low positive value of the failure function, and the other three grains are scattered in a non-systematic way on the diagram.

Table 6.2 summarizes the results of the analyzed area of the sample No. Ni-106. About 80% of all investigated grains are correctly classified, and only 3% of grains were predicted incorrectly to have no damage.

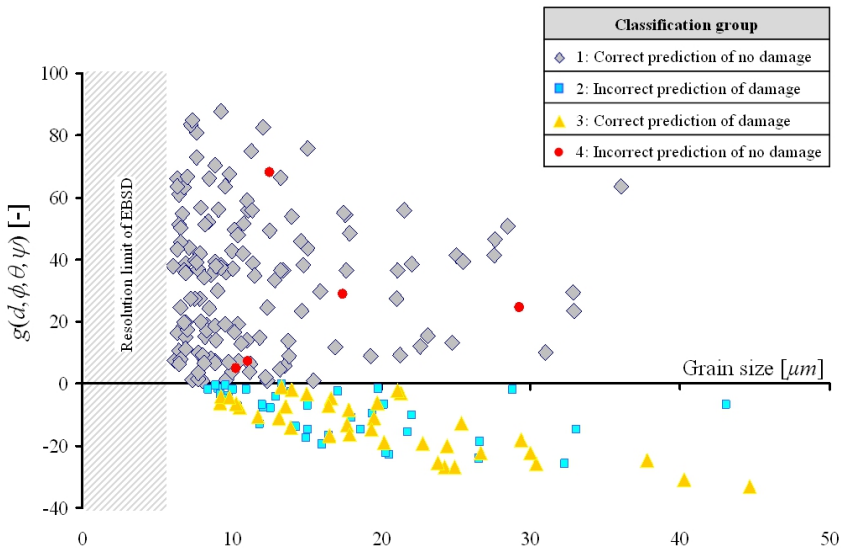


Fig. 6.14. Failure function versus grain size for the weakest slip system of the grains considering all four classification groups, sample No. Ni-106 (totally 220 grains presented on the diagram).

Table 6.2. Comparison between predictions of failure function and observed damage in grains of sample No. Ni-106.

Classification group	Failure function	Surface inspection	Number of grains	Percentage of grains [%]
1 correct prediction of no damage	$g \geq 0$ undamaged	No damage visible	139	63
2 incorrect prediction of damage	$g < 0$ damaged	No damage visible	39	17
3 correct prediction of damage	$g < 0$ damaged	Damage visible	37	17
4 incorrect prediction of no damage	$g \geq 0$ undamaged	Damage visible	5	3

6.3 Results of sample No. Ni-105

Initially, this sample was exposed to a stress amplitude of ± 150 MPa for 2×10^6 cycles and subsequently inspected by ultraviolet laser scanning microscopy. Since there was no micro-damage visible at the surface of the sample, the HCF test was continued (with the same stress range) up to 10^7 cycles. Fig. 6.15 shows a SEM micrograph of the surface grains after continued load cycling. Only in some rare cases, micro-damage is detected in grains. In most of the grains just smooth surface markings are observed which are due to the extrusions and intrusions caused by the plastic strains along the activated slip bands. These results reveal that in majority of grains the strain localization and surface roughening caused by PSBs have not taken place yet, since the stress amplitude was not sufficiently high. Fig. 6.16 gives a closer view of a grain, where surface roughening and micro-damage caused by PSBs are obvious.

The failure function was calculated for sample No. Ni-105 as described before. It was noticed that the failure function had a positive value for all analyzed grains ($g > 0$). This is in agreement with the investigation results of surface grains, where most of them are undamaged (except some rare cases). The accumulated plastic shear strain has not exceeded the critical limit Γ_c in the grains of this sample.

The predicted results of the failure function versus grain size are shown in Fig. 6.17 for the analyzed area with 417 grains. Table 6.3 summarizes the results of comparison between the predictions of failure function and the observed micro-damage for the sample No. Ni-105. About 99% of the grains have been classified correctly, and only 1% of grains were predicted incorrectly to have no damage. Since the micro-damage occurred between 2×10^6 and 10^7 load cycles, it indicates that by increasing the number of the load cycles, a few grains can be damaged. The influence of the number of load cycles on occurrence of new micro-damage is investigated in the next section for the sample No. Ni-108.

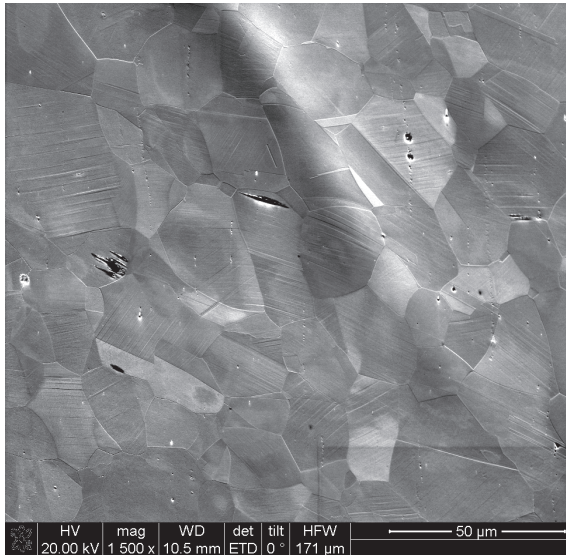


Fig. 6.15. SEM micrograph of surface grains: regular surface markings due to dislocations at slip bands and some rare PSB's, sample No. Ni-105 (after 10^7 cycles of uniaxial bending with an amplitude of ± 150 MPa).

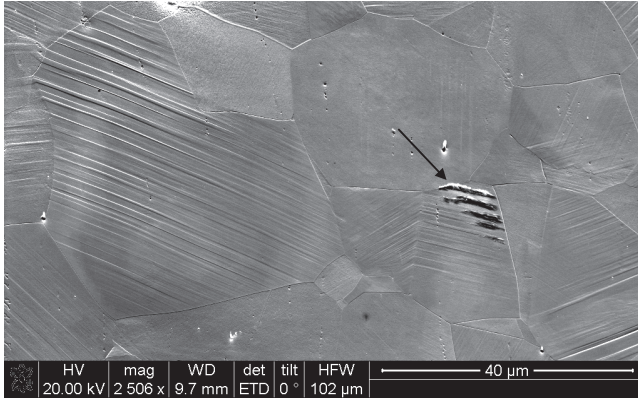


Fig. 6.16. Regular surface markings due to dislocations along slip bands. Formation of PSBs in one grain due to strain localization, sample No. Ni-105 (after 10^7 cycles of uniaxial bending with an amplitude of ± 150 MPa).

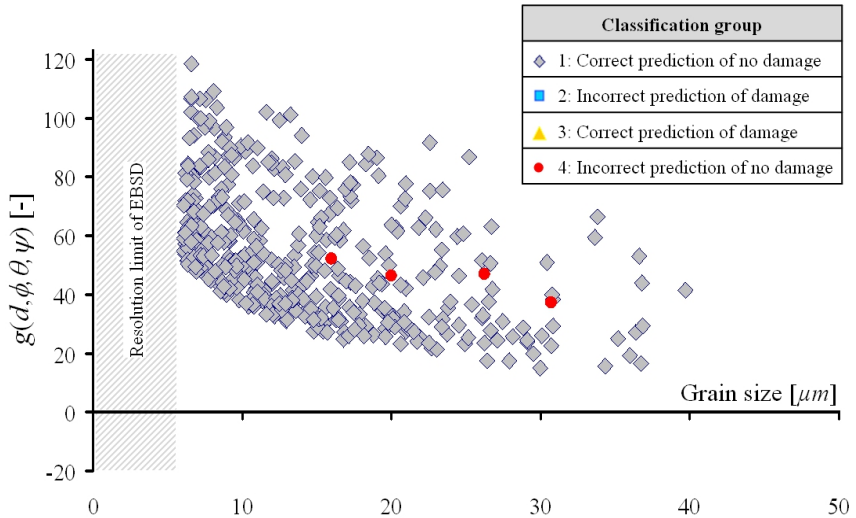


Fig. 6.17. Failure function versus grain size for the weakest slip system of grains considering all four classification groups, sample No. Ni-105 (totally 417 grains presented on the diagram).

Table 6.3. Comparison between predictions of failure function and observed micro-damage in sample No. Ni-105.

Classification group	Failure function	Surface inspection	Number of grains	Percentage of grains [%]
1 correct prediction of no damage	$g \geq 0$ undamaged	No damage visible	413	99
2 incorrect prediction of damage	$g < 0$ damaged	No damage visible	0	0
3 correct prediction of damage	$g < 0$ damaged	Damage visible	0	0
4 incorrect prediction of no damage	$g \geq 0$ undamaged	Damage visible	4	1

6.4 Results of sample No. Ni-108

In the results of the previous samples No. Ni-106 and Ni-107, it was already observed that at the stress amplitude of ± 200 MPa and after 2×10^6 load cycles a reasonable amount of micro-damage occurred. Now the question is what happens in the grains, if those samples are exposed to more load cycles (at the same stress amplitude)?

To answer this question, sample No. Ni-108 was exposed to the nominal stress amplitude of ± 200 MPa but for a longer testing duration of 4×10^6 cycles. So it can be verified experimentally, if after 2×10^6 load cycles the existing micro-damage evolves further, and if the micro-damage occurs in more grains. Furthermore the prediction power of the failure function can be evaluated specifically if the number of load cycles is increased.

Fig. 6.18 shows the SEM micrographs of the surface grains in sample No. Ni-108. Comparing the results to the samples discussed earlier, more grains are damaged in this sample by extrusions and intrusions. Furthermore the micro-damage is extended to a larger area of the grains. It indicates that keeping the nominal stress amplitude of ± 200 MPa and increasing the number of load cycles from 2×10^6 to 4×10^6 lead to the formation of more PSBs and further evolution of existing micro-damage.

For further analysis FIB cross sections were performed for a few damaged grains. In some cases micro-cracks have been initiated along PSBs (Fig. 6.19).

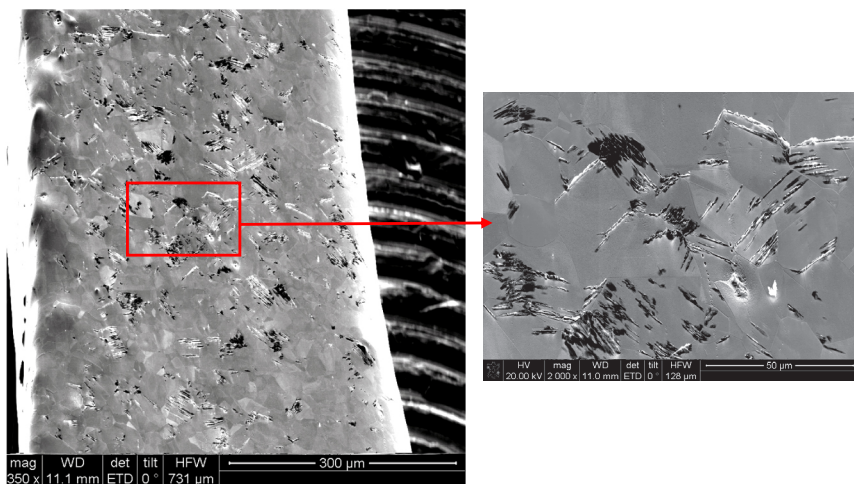


Fig. 6.18. SEM micrograph of the surface grains. Formation of PSBs and micro-damage is visible in many grains, sample No. Ni-108 (after 4×10^6 cycles of uniaxial bending with an amplitude of ± 200 MPa).

Fig. 6.20 illustrates the failure function versus grain size for the weakest slip system of grains considering all four classification groups. Totally 184 grains are analyzed and the classification results are summarized in Table 6.4.

Comparing to the previous samples, the percentage of the grains in the 3rd classification group is more than in the 2nd classification group, indicating that the damage can be observed more obviously in the grains of sample No. Ni-108.

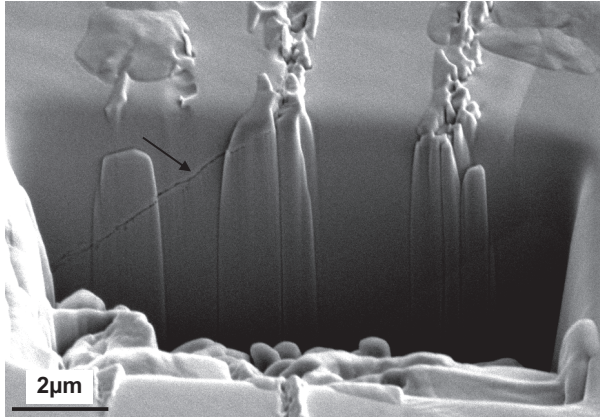


Fig. 6.19. FIB cross section: micro-crack initiated, sample No. Ni-108 (after 4×10^6 cycles of uniaxial bending with an amplitude of ± 200 MPa).

Considering the results of the 4th classification group, it is noticeable that the prediction power of the failure function has reduced for the mentioned load condition, where more grains are damaged, which were predicted not to be damaged. As described in sections 3.3 and 3.4, the grain fulfills the elastic shakedown and remains in hardening phase, if the accumulated plastic shear strain bounds to a limit. At the end of the hardening phase, the first PSBs are created and during the saturation phase the number of PSBs increases [97]. About 38% of the analyzed grains in sample No. Ni-108 present micro-damage related to PSBs. This indicates that these grains are not anymore in the hardening phase.

Two specific aspects for the sample No. Ni-108 are the higher stress amplitude (comparing to the sample No. Ni-105) and the increased number of load cycles (from 2×10^6 to 4×10^6 cycles). These aspects have led to the occurrence of more micro-damage and more pronounced mechanical interaction between damaged neighboring grains, which was already addressed as a cause of misclassification in the results of sample No. Ni-107. In such cases, the assumption, that in HCF regime each plastically deforming grain is surrounded by grains which show elastic behavior, is not as accurate as for previous samples.

Particularly at the beginning of the micro-damage evolution, the proposed failure function has a very good prediction power for the failure of grains in HCF due to micro-damage caused by dislocation movements along PSBs. By occurrence of more and severe micro-damage (at higher stress amplitudes and higher cycle numbers), the influence of damaged neighboring grains leads to the reduction of the prediction accuracy, indicating a limiting factor in application of the failure function.

As refining approach of the HCF model in future work, it is proposed to consider the influence of surrounding grains, which suffer plastic strains, e.g. by modification of the Lin-Taylor theorem applied in Eq. 16.

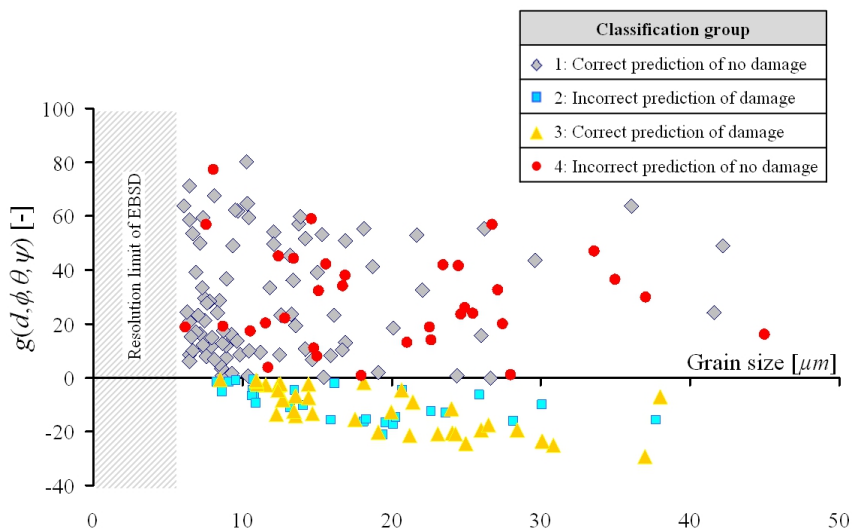


Fig. 6.20. Failure function versus grain size for the weakest slip system of grains considering all four classification groups, sample No. Ni-108 (totally 184 grains presented on the diagram).

Table 6.4. Comparison between predictions of failure function and observed damage in sample No. Ni-108.

Classification group	Failure function	Surface inspection	Number of grains	Percentage of grains [%]
1 correct prediction of no damage	$g \geq 0$ undamaged	No damage visible	87	47
2 incorrect prediction of damage	$g < 0$ damaged	No damage visible	27	15
3 correct prediction of damage	$g < 0$ damaged	Damage visible	36	20
4 incorrect prediction of no damage	$g \geq 0$ undamaged	Damage visible	34	18

7 Summary

A new micro-mechanical approach for the prediction of multiaxial HCF failure in individual grains of fcc metals was established. Since the fatigue damage is controlled by mechanisms at the grain level, the HCF model considers elasto-plastic behavior of metals at the grain level and influence of microstructural parameters – specifically the grain size and the grain orientation – on fatigue strength. The elaborated micro-mechanical model uses the plastic shear strain accumulated in the grains as a damage variable to predict the HCF failure. Thus, a link between microstructural parameters and macroscopic stresses is established. The HCF model is established particularly for the prediction of the HCF failure in small scale applications (length scales of 5-100 μm), e.g. micro-parts or MEMS. Unlike other fatigue criteria, it considers the initiation of HCF damage in individual grains and not the propagation of HCF crack at macroscopic scales or in the bulk material.

Based on the micro-mechanical model a failure function for prediction of HCF damage was established, and the relevant parameters of the function were identified. The failure function can be utilized for deterministic prediction of failure in individual grains, and also for probabilistic failure description in aggregates of grains with random properties. These two application fields were discussed extensively in the parameter study and sensitivity analysis.

It was revealed that the sensitivity of the failure probability with respect to the grain orientation (Euler-angles) is higher than with respect to the grain size. This is in agreement with previous work of Ziemann on thin films, which disclosed also high dependency of plastic deformation on the grain orientation [98].

The failure function shows that there is not a specific preferred slip system for HCF crack initiation, but the weakest slip system varies depending on the grain orientation and load condition.

To verify the correctness of the prediction results obtained by the HCF model, fatigue experiments were performed with a custom-built test setup on nickel micro-samples, and the predicted results were compared with occurrence of micro-damage for each grain on the specimen surface. The grain size and the grain orientation were measured on the surface of the samples by the EBSD analyses, as the main input variables of the failure function. Occurrence of

micro-damage (during HCF experiments) on surface grains was analyzed with SEM microscopy and FIB cross sections.

By comparison between prediction results and observed micro-damage, a classification scheme was obtained for several hundreds of individual analyzed grains. The overall agreement between predicted results of the failure function and observed micro-damage is fairly good (with low misclassification probability) and in line with the expected trend that for larger grains the failure probability is higher than for smaller ones. Generally, the classification works well for the overwhelming majority of the analyzed grains. Nevertheless, some grains were misclassified as undamaged, while some damage was observed.

It is argued that one of the reasons for these misclassifications is due to uncertainties in the applied material parameters or in the measured micro-structural properties. In a deterministic setting, the misclassifications can be avoided by adding safety factors when calculating the failure function. Within a probabilistic approach, the uncertainties can be addressed by a suitably chosen misclassification probability, similar to non-detection probability approaches in non-destructive inspection modeling [76].

Considering the fact that the failure function evaluates each grain individually, the other aspect addressed as a cause for misclassifications is the mechanical interaction between the neighboring grains, which is intensified by evolution of more and severe micro-damage (at higher stress amplitudes and higher cycle numbers). Such an effect reduces the prediction power of the failure function as a limiting factor. This case was outside the scope of the underlying failure function, however it can be considered in refining approaches of the failure function in future work.

In future work, the predictive power of the failure function needs to be verified using multiaxial HCF experiments and other fcc metals.

The HCF model presents promising results in prediction of fatigue failure at small scales, but its application for all individual grains of a component can be intricate. In special cases, it is easier to apply it, if the grains have a preferred orientation or size distribution due to the manufacturing processes. In those cases the texture of the microstructure can be estimated using data of similar samples, and there is no need to analyze the individual grains with EBSD. Such applications can be related for example to HCF prediction of bamboo-structured

micro-wires or thin films, which are used widely in microelectronics [91, 99, 110-111].

8 References

1. H. Mughrabi: Cyclic deformation and fatigue, some current problems, in H.J. McQueen, J.-P. Bailon, J.I. Dickson, J.J. Jonas and M.G. Akben (eds.), Proc. 7th Int. Conf. on the Strength of Metals and Alloys, Montreal, August 12-16, 1985, Vol. 3, Pergamon, Oxford, pp. 1-26 (1985).
2. H. Mughrabi: Fatigue, an everlasting materials problem- still en vogue, *Procedia Engineering* 2, pp. 3-26 (2010).
3. I.V. Papadopoulos, P. Davoli, C. Gorla, M. Filippini, A. Bernasconi: A comparative study of multiaxial high-cycle fatigue criteria for metals, *Int. J. Fatigue*, Vol. 19, No. 3, pp. 219-235 (1997).
4. A. Constantinescu, K. Dang Van, M.H. Maitournam: A unified approach for high and low cycle fatigue based on shakedown concepts, *Fatigue Fract Engng Mater Struct* 26, pp. 561-568 (2003).
5. P. Ballard, K. Dang Van, A. Deperrois, Y.V. Papadopoulos: High cycle fatigue and finite element analysis, *Fatigue Fract. Engng Mater. Struct.* Vol. 18, No. 3, pp. 397-411 (1995).
6. K. Dang Van: Fatigue analysis by the multiscale approach, *High Cycle Metal Fatigue, From Theory to Applications*, C.I.S.M. Courses and Lectures No. 392, Ed. K. Dang Van & I.V. Papadopoulos, Springer (1999).
7. E. Charkaluk, A. Constantinescu, H. Maïtournam, K. Dang Van: Revisiting the Dang Van criterion, *Procedia Engineering*, Vol. 1, pp. 143-146 (2009).
8. I.V. Papadopoulos: Long life fatigue under multiaxial loading, *International Journal of Fatigue* 23 (2001).

9. I.V. Papadopoulos: Multiscale fatigue limit criterion of metals, a mesoscopic scale approach, High Cycle Metal Fatigue, From Theory to Applications, C.I.S.M. Courses and Lectures No. 392, Ed. K. Dang Van & I.V. Papadopoulos, Springer (1999).
10. A.W. Thompson, W.A. Backofen: the effect of grain size on fatigue, ACTA METALLURGICA, Vol. 19 (1971).
11. P. Lukas, L. Kunz: Effect of grain size on the high cycle behaviour of polycrystalline copper, Materials Science and Engineering, 85, pp. 67-75 (1987).
12. T. Hanlon, Y.-N. Kwon, S. Suresh: Grain size effects on the fatigue response of nanocrystalline metals, Scripta Materialia 49, pp. 675-680 (2003).
13. G.J. Weng: A micromechanical theory of grain-size dependence in metal plasticity, J. Mech. Phys. Solids Vol. 31, No. 3, pp. 193-203 (1983).
14. D. Walgraef, E.C. Aifantis: Dislocation patterning in fatigued metals as a result of dynamic instabilities, Journal of Appl. Physics, Vol. 58, pp. 688-691 (1985).
15. C. Buque, J. Bretschneider, A. Schwab, C. Holste: Dislocation structures in cyclically deformed nickel polycrystals, Materials Science and Engineering A300, pp. 254-262 (2001).
16. R. Morrissey, C-H. Coh, D. L. McDowell: Microstructure-scale modeling of HCF deformation, Mechanics of Materials 35, pp. 295-311 (2003).
17. V.P. Bennett, D.L. McDowell: Polycrystal orientation distribution effects on microslip in high cycle fatigue, International Journal of Fatigue 25, pp. 25-39 (2003).

18. N.K. Arakere, G. Swanson: Effect of crystal orientation on fatigue failure of single crystal nickel base turbine blade superalloys, *Journal of Engineering for Gas Turbines and Power*, Transactions of the ASME, Vol. 124 (2002).
19. C. Buque: Persistent slip bands in cyclically deformed nickel polycrystals, *International Journal of Fatigue*, pp. 459-466 (2001).
20. S. Suresh: *Fatigue of Materials*, Cambridge University Press, 2nd Edition (1998).
21. G. Schott: *Werkstoffermüdung- Ermüdungsfestigkeit*, 4. Auflage, Dt. Verl. für Grundstoffindustrie (1997).
22. U. Zerbst, K. Mädler, H. Hintze: Fracture mechanics in railway applications- an overview, *Engineering Fracture Mechanics*, Vol. 72, pp. 163-194 (2005).
23. S. Beretta, A. Ghidini, F. Lombardo: Fracture mechanics and scale effects in the fatigue of railway axles, *Engineering Fracture Mechanics*, Vol. 72, pp. 195-208 (2005).
24. U. Zerbst, S. Beretta: Failure and damage tolerance aspects of railway components, *Engineering Failure Analysis*, Vol. 18, pp. 534-542 (2011).
25. J. Goodman: *Mechanics Applied to Engineering*, Longmans, Green and Co., London (1914).
26. J.E. Shigley, L.D. Mitchell: *Mechanical Engineering Design*, Fourth Edition, McGraw-Hill, New York, p. 273 (1983).
27. L.F. Coffin, A study of the effects of the cyclic thermal stresses on a ductile metal, *Transactions of ASME*, Vol. 76, pp. 931- 950 (1954).

28. S.S. Manson: Behaviour of materials under conditions of thermal stress. NACA TN-2933, National Advisory Committee for Aeronautics (1954).
29. T.H. Courtney: Mechanical behavior of materials, 2nd Edition, Waveland Press (2005).
30. J. Rösler, H. Harders, M. Bäker: Mechanisches Verhalten der Werkstoffe, 3. Auflage, Vieweg + Teubner (2008).
31. M. Klesnil, P. Lukas: Fatigue of metallic materials, 2nd rev. ed., Elsevier Amsterdam, pp. 35-49 (1992).
32. V. Monchiet, E. Charkaluk, D. Kondo: Plasticity-damage based micromechanical modelling in high cycle fatigue, C.R. Mecanique 334, pp.129-136 (2006).
33. F. Hofmann, G. Bertolino, A. Constantinescu, M. Ferjani: Numerical exploration of the Dang Van high cycle fatigue criterion: application to gradient effects, Journal of Mechanics of Materials and Structures, Volume 4, No. 2 (2009).
34. E. Kröner: Zur plastischen Verformung des Vielkristalls, Acta Metall. 99, pp. 155-161 (1961).
35. R. Hill: Elastic properties of reinforced solids: Some theoretical principles, J. Mech. Phys. Solids, Vol. 11, pp. 357-372 (1963).
36. Z. Hashin: Theory of mechanical behavior of heterogeneous media, Appl. Mech. Rev., Vol. 17, pp. 1-9 (1964).
37. S. Weyer: Mikromechanisches Modell zur Ermittlung effektiver Materialeigenschaften von geschädigten Polykristallen, PhD Thesis, IKM, Karlsruhe Institute of Technology (2001).

38. B-R. You, S-B Lee: A critical review on multiaxial fatigue assessments of metals, *Int. J. Fatigue*, Vol. 18, No. 4, pp. 235-244 (1996).
39. B. Li, L. Reis, M. de Freitas: Comparative study of multiaxial fatigue damage models for ductile structural steels and brittle materials, *International Journal of Fatigue*, Vol. 31, pp. 1895-1906 (2009), doi: 10.1016/j.ijfatigue.2009.01.006.
40. K.C. Liu, J.A. Wang: An energy method for predicting fatigue life, crack orientation, and crack growth under multiaxial loading conditions, *International Journal of Fatigue*, Vol. 23, pp. 129-134 (2001).
41. G. Sines: In metal fatigue (Eds. G. Sines and J.L. Waisman). McGraw-Hill, New York, pp. 145-169 (1959).
42. J. Lemaitre, J.-L. Chaboche: *Mechanics of solid materials*, Cambridge University Press, Cambridge (1990).
43. Y-Y. Wang, W-X. Yao: Evaluation and comparison of several multiaxial fatigue criteria, *International Journal of Fatigue*, Vol. 26, pp. 17-25 (2004).
44. H.J. Gough, H.V. Pollard: The strength of metals under combined alternating stress., *Proc. Inst. Mech. Engrs.*, Vol. 131, pp. 3-103 (1925).
45. H.J. Gough, H.V. Pollard: Properties of some materials for cast crankshafts, with special reference to combined alternating stresses, *Proc. Inst. Automobile Engrs.*, Vol. 31, pp. 821-893 (1937).
46. B. Crossland: Effect of large hydrostatic pressures on the torsional fatigue strength of an alloy steel, *Proc. Int. Conf. on Fatigue of Metals-I.M.E.-U.K.*, pp. 138-149 (1956).

47. H. Kakuno, Y. Kawada: A new criterion of fatigue strength of a round bar subjected to combined static and repeated bending and torsion, *Fatigue Fract. Engng Mater. Struct.*, Vol. 2, pp. 229-236 (1979).
48. W.N. Findley: A theory for the effect of mean stress on fatigue of metals under combined torsion and axial load or bending, *J. Eng. Ind., Trans. ASME*, Vol. 81, pp. 301-306 (1959).
49. T. Matake: An explanation on fatigue limit under combined stress, *Bull JSME*, Vol. 20, pp. 257-263 (1977).
50. D.L. McDiarmid: A general criterion for high cycle multiaxial fatigue failure, *Fatigue Fract. Engng Mater. Struct.*, Vol. 14, pp. 429-453 (1991).
51. E. Orowan: Theory of the fatigue of metals, *Proceedings of the Royal Academy A, London*, pp. 79-106 (1939).
52. K. Tanaka, T. Mura: A dislocation model for fatigue crack initiation, *Trans. ASME, Journal of Appl. Mech.*, Vol. 48, pp. 97-103 (1981).
53. H.J. Gough: Crystalline structure in relation to failure of metals - especially by fatigue. Eighth Edgar Marburg Lecture 33. *Proceedings ASTM* (1933).
54. J. Polák, J. Man: Mechanisms of extrusion and intrusion formation in fatigued crystalline materials, *Mat. Sci. Eng. A596*, pp. 15-24 (2013).
55. Z.S. Basinski, S.J. Basinski: Fundamental aspects of low amplitude cyclic deformation in face-centered cubic crystals. *Progress in Materials Science*, Vol. 36, pp. 89-148 (1992).
56. E. Schmid, W. Boas: *Kristallplastizität mit besonderer Berücksichtigung der Metalle (Struktur und Eigenschaften der Materie, Bd. XVII)*, Springer Berlin (1935).

57. V. Vitek, M. Mrovec, J.L. Bassani: Influence of non-glide stresses on plastic flow: from atomistic to continuum modeling, *Materials Science and Engineering A365*, pp. 31-37 (2004).
58. Z. Chen: Modelling the plastic deformation of iron, *Schriftenreihe des Instituts für Angewandte Materialien Band 15*, KIT (2013).
59. K. Ito, V. Vitek: Atomistic study of non-Schmid effects in the plastic yielding of bcc metals, *Philosophical Magazine A*, Vol. 81, Issue 5, pp. 1387-1407 (2001).
60. R. Gröger, A.G. Bailey, V. Vitek: Multiscale modeling of plastic deformation of molybdenum and tungsten: I. Atomistic studies of the core structure and glide of $1/2 \langle 111 \rangle$ screw dislocations at 0K. *Acta Materialia*, Vol. 56, pp. 5401-5411 (2008).
61. M.S. Duesbery: On non-glide stresses and their influence on the screw dislocation core in body-centred cubic metals. I. The Peierls stress. *Proceedings of the Royal Society of London, Series A*, Vol. 392, pp. 145-173 (1984).
62. F. Morel: A critical plane approach for life prediction of high cycle fatigue under multiaxial variable amplitude loading, *International Journal of Fatigue*. Vol. 22, pp. 101-119 (2000).
63. T.L. Anderson: *Fracture mechanics, fundamentals and applications*, second edition, CRC Press (1995).
64. C.H. Wang, M.W. Brown: Life prediction techniques for variable amplitude multiaxial fatigue – part 1: theories. *J. Eng. Mater. Technol.*, Vol. 118, pp. 367-370 (1996).
65. W.T. Koiter: General theorems for elastic-plastic solids, In: I.N. Sneddon and R. Hill (Eds.), *Progress in Solid Mechanics*, Vol. 4, North-Holland Publishing Co., Amsterdam, pp. 165-221 (1960).

66. J. Mandel, B. Halphen, J. Zarka: Adaptation d'une Structure Elastoplastique à Ecrouissage Cinématique, *Mech. Res. Commun.* 4, pp. 309-314 (1977).
67. G. Maier: On some issues in shakedown analysis, *J. Appl. Mech., AMSE* 68 (5), pp. 799-808 (2001).
68. Q. S. Nguyen: *Stability and nonlinear solid mechanics*, Wiley, Chichester (2000).
69. G. Sines, G. Ohgi: Fatigue criteria under combined stresses or strains, *J. Eng. Mater. Technol.*, Vol. 103, pp. 82-90 (1981), doi: 10.1115/1.3224995.
70. B. von Blanckenhagen, P. Gumbsch, E. Arzt: Dislocation sources in discrete dislocation simulations of thin-film plasticity and the Hall-Petch relation, *Modelling Simul. Mater. Sci. Eng.*, Vol. 9, pp. 157-169 (2001).
71. M. Kato: Hall-Petch relationship and dislocation model for deformation of ultrafine-grained and nanocrystalline metals, *Materials Transactions*, Vol. 55, No. 1, pp. 19-24 (2014), doi:10.2320/matertrans.MA201310.
72. E. W. Weisstein: Euler Angles, from MathWorld a Wolfram web resource, <http://mathworld.wolfram.com/EulerAngles.html> (last visited: 15 Mar. 2015).
73. <http://www.oxford-instruments.com/products/microanalysis/ebstd/ebstd-post-processing-software> (last visited: 18 Sept. 2015).
74. A.J. Schwartz, M. Kumar, B.L. Adams, D.P. Field (Eds.): *Electron backscatter diffraction in materials science*, 2nd ed., Springer (2009).
75. O. Engler, V. Randle: *Introduction to texture analysis: microtexture, microtexture, and orientation mapping*, 2nd ed., CRC Press (2010).

-
76. H. Riesch-Oppermann, A. Brückner-Foit: First- and Second-Order approximations of failure probabilistic in probabilistic fracture mechanics, *Reliability Engineering and System Safety* 23, pp. 183-194 (1988).
 77. A. Steckmeyer, M. Sauzay, A. Weidner, E. Hieckmann: Micromechanical modelling of the cyclic stress-strain behaviour of nickel polycrystals, *International Journal of Fatigue* 40, pp. 154-167 (2012).
 78. A.W. Thompson: Yielding in nickel as a function of grain or cell size, *Acta Metall.*, Vol. 23, pp. 1337-1342 (1975).
 79. H. Mughrabi, F. Ackermann, K. Herz: Persistent slip bands in fatigued face-centered and body-centered cubic metals, in: J.T. Fong (Ed.): *Fatigue Mechanisms*, ASTM STP 675, pp. 69-105 (1979).
 80. D.J. Morrison, V. Chopra, J.W. Jones: Effects of grain size on cyclic strain localization in polycrystalline nickel, *Scripta METALLURGICA et MATERIALIA*, Vol. 25, pp. 1299-1304 (1991).
 81. D.J. Morrison, J.C. Moosbrugger: Effects of grain size on cyclic plasticity and fatigue initiation in nickel, *Int. J. Fatigue*, Vol. 19, pp. 51-59 (1997).
 82. H. Riesch-Oppermann, A. Brückner-Foit: Probabilistic fracture mechanics applied to high temperature reliability, *Nuclear Engineering and Design* 128, pp. 193-200 (1991).
 83. L. Cizelj, H. Riesch-Oppermann: ZERBERUS- the code for reliability analysis of crack containing structures, KfK 5019, Kernforschungszentrum Karlsruhe, Institut für Materialforschung (1992).
 84. <http://www.wolfram.com/mathematica> (last visited: 15 Mar. 2015).

85. T. Straub, T. Kennerknecht, P. Robin, M. Tort, G. Kieffer, Y. Lapusta, C. Eberl: Small-scale multiaxial fatigue experiments in the very high cycle regime, Proceedings of the 5th international conference on very high cycle fatigue, Vol. 5, pp. 473-478 (2011).
86. T. Straub, M.F. Berwind, T. Kennerknecht, Y. Lapusta, C. Eberl: Small-scale multiaxial setup for damage detection into the very high cycle fatigue regime, Experimental Mechanics, Vol. 55, pp. 1285-1299 (2015), doi: 10.1007/s11340-015-0027-z.
87. T. Kennerknecht, T. Straub, M. Funk, F.A. Çetinel, M. Härtelt, C. Eberl: Zuverlässigkeit von mikroungeformten und nanostrukturierten Materialien unter Berücksichtigung der besonderen Anforderungen an Mikrobauteile, KIT scientific reports 7591, Kolloquium Mikroproduktion und Abschlusskolloquium SFB 499 (2011).
88. T. Straub: Private communication.
89. J. Sörensen: Untersuchungen zur Vereinfachung der Kerbformoptimierung, FZKA 7397 (2008).
90. C. Mattheck: Teacher tree: The evolution of notch shape optimization from complex to simple, Engineering Fracture Mechanics, Vol. 73, Issue 12, pp. 1732-1742 (2006), doi: 10.1016/j.engfracmech.2006.02.007.
91. B. Czerny, I. Paul, G. Khatibi, M. Thoben: Experimental and analytical study of geometry effects on the fatigue life of Al bond wire interconnects, Microelectronics Reliability, Vol. 53, pp. 1558-1562 (2013).
92. B. Czerny, G. Khatibi, B. Weiss, T. Licht: A fast test technique for life time estimation of ultrasonically welded Cu–Cu interconnects, Microelectronics Reliability, Vol. 50, pp. 1641-1644 (2010).

93. R. Eslami, H. Riesch-Oppermann, O. Kraft: Prediction of multiaxial high cycle fatigue at small scales based on a micro-mechanical model, *International Journal of Fatigue*, Vol. 83, pp. 66-74 (2016), doi: 10.1016/j.ijfatigue.2015.03.029.
94. R. Eslami, H. Riesch-Oppermann, O. Kraft: A micro-mechanical model for multiaxial high cycle fatigue at small scales, XVII International Colloquium on Mechanical Fatigue of Metals (ICMFM17), *Procedia Engineering*, Vol. 74, pp. 57-63 (2014), doi: 10.1016/j.proeng.2014.06.224.
95. M. Yang, Y. Akiyama, T. Sasaki: Evaluation of change in material properties due to plastic deformation, *Journal of Materials Processing Technology*, Vol. 151, pp. 232-236 (2004).
96. J.C. Grosskreutz: Fatigue mechanisms in the sub-creep range, in: *metal fatigue damage: mechanism, detection, avoidance, and repair*, ASTM STP 495, Ed. S.S. Manson, pp. 5-60 (1971).
97. F. Morel: A fatigue life prediction method based on a mesoscopic approach in constant amplitude multiaxial loading, *Fatigue & Fracture of Engineering Materials & Structures*, Vol. 21, pp. 241-256 (1998).
98. M. Ziemann: Experimentelle Untersuchung der Materialermüdung in zyklisch belasteten Kupferdünnschichten, Diplomarbeit an der Fakultät für Physik der Ludwig-Maximilians-Universität München (2012).
99. M. Ohring: *Materials science of thin films. Deposition and structure*, Academic Press, 2nd edition (2001).
100. F. Bridier, D.L. McDowell, P. Villechaise, J. Mendez: Crystal plasticity modeling of slip activity in Ti-6Al-4V under high cycle fatigue loading, *International Journal of Plasticity*, Vol. 25, pp. 1066-1082 (2009).

101. B. Jiang, G.J. Weng: A composite model for the grain-size dependence of yield stress of nanograined materials, *Metallurgical and Materials Transactions A*, Volume 34, pp. 765-772 (2003).
102. T.H. Lin, Y.M. Ito: Mechanics of a fatigue crack nucleation mechanism, *Journal of the Mechanics and Physics of Solids*, Vol. 17, pp. 515-523 (1969).
103. H. Mughrabi: Damage mechanisms and fatigue lives: From the low to the very high cycle regime, *Procedia Engineering* 55, pp. 636-644 (2013).
104. G. Sines: Behavior of metals under complex static and alternating stresses, in: G. Sines, J.L. Waisman (Eds.), *Metal Fatigue*, McGraw-Hill, New York, pp. 145-159 (1959).
105. Y.S. Garud: A new approach to the evaluation of fatigue under multiaxial loadings, *Journal of Engineering Materials and Technology*, Vol. 103, pp. 118-125 (1981).
106. R. Schwaiger, O. Kraft: Size effects in the fatigue behavior of thin Ag films, *Acta Materialia*, Vol. 51, pp. 195-206 (2003).
107. D. Wang, C.A. Volkert, O. Kraft: Effect of length scale on fatigue life and damage formation in thin Cu films. *Materials Science and Engineering A*, Vol. 493, pp. 267-273 (2008), doi:10.1016/j.msea.2007.06.092.
108. H. Mughrabi: Microstructural mechanisms of cyclic deformation, fatigue crack initiation and early crack growth, *Phil. Trans. R. Soc. A373* (2015), <http://dx.doi.org/10.1098/rsta.2014.0132>.
109. U. Essmann, U. Gösele, H. Mughrabi: A model of extrusions and intrusions in fatigued metals I. Point-defect production and the growth of extrusions, *Philosophical Magazine A*, Vol. 44, pp. 405-426 (1981), doi: 10.1080/01418618108239541.

110. G. Khatibi, A. Betzwar-Kotas, V. Gröger, B. Weiss: A study of the mechanical and fatigue properties of metallic microwires, *Fatigue Fract Engng Mater Struct*, Vol. 28, pp. 723-733 (2005), doi: 10.1111/j.1460-2695.2005.00898.x.
111. M. Ziemann, Y. Chen, O. Kraft, E. Bayerschen, S. Wulfinghoff, C. Kirchlechner, N. Tamura, T. Böhlke, M. Walter, P.A. Gruber: Deformation patterns in cross-sections of twisted bamboo-structured Au microwires. *Acta Materialia*, Vol. 97, pp. 216-222 (2015), doi: 10.1016/j.actamat.2015.06.012.

Appendix A1: Euler-angles and rotation matrices

The orientation of a rigid body in three-dimensional space can be described by three independent parameters. For definition of these parameters there are different methods, amongst them the Euler-angles are very well-known. According to Euler rotation theorem, any rotation may be described using three angles. If the rotations are written in terms of corresponding matrices D , C , and B , then a general rotation A can be decomposed into three subsequent rotations D , C , and B according to [72]¹¹:

$$A = BCD \tag{52}$$

The three angles describing these three rotations are the Euler-angles, denoted as (ϕ, θ, ψ) . Out of the several conventions for definition of Euler-angles (depending on the axes about which the individual rotations are performed), the so-called x-convention is used here (Fig. A1.1).

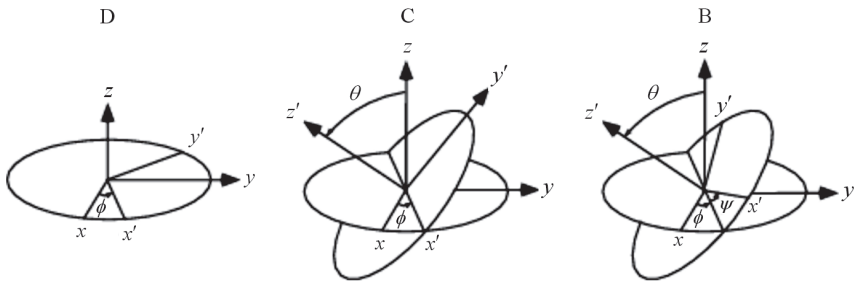


Fig. A1.1. Illustration of three Euler-angles and associated rotation matrices. Reference of the figure is: [72], with some small modifications.

¹¹ This appendix is written mainly based on reference [72]. Readers are referred to this reference for some more details on this topic.

The first rotation about the z-axis is presented with the angle ϕ and is associated to the rotation matrix D. The second rotation with an angle θ is about the initial x-axis (which is already rotated to the x'-axis), and shown with the matrix C. The last rotation is with an angle ψ about the initial z-axis (which is rotated already to the z'-axis), and presented by matrix B. The rotation matrices are given by [72]:

$$B = \begin{bmatrix} \cos\psi & \sin\psi & 0 \\ -\sin\psi & \cos\psi & 0 \\ 0 & 0 & 1 \end{bmatrix} \quad (53)$$

$$C = \begin{bmatrix} 1 & 0 & 0 \\ 0 & \cos\theta & \sin\theta \\ 0 & -\sin\theta & \cos\theta \end{bmatrix} \quad (54)$$

$$D = \begin{bmatrix} \cos\phi & \sin\phi & 0 \\ -\sin\phi & \cos\phi & 0 \\ 0 & 0 & 1 \end{bmatrix} \quad (55)$$

In this work the components of the inverse matrix A^{-1} were needed to find the orientation of the grains with respect to the global coordinates system. According to Eq. 52 to 55, the components of A^{-1} read as:

$$a_{11}^{-1} = \cos\psi \cos\phi - \cos\theta \sin\phi \sin\psi \quad (56)$$

$$a_{12}^{-1} = -\sin\psi \cos\phi - \cos\theta \sin\phi \cos\psi \quad (57)$$

$$a_{13}^{-1} = \sin\theta \sin\phi \quad (58)$$

$$a_{21}^{-1} = \cos\psi \sin\phi + \cos\theta \cos\phi \sin\psi \quad (59)$$

$$a_{22}^{-1} = -\sin\psi \sin\phi + \cos\theta \cos\phi \cos\psi \quad (60)$$

$$a_{23}^{-1} = -\sin \theta \cos \phi \quad (61)$$

$$a_{31}^{-1} = \sin \psi \sin \theta \quad (62)$$

$$a_{32}^{-1} = \cos \psi \sin \theta \quad (63)$$

$$a_{33}^{-1} = \cos \theta \quad (64)$$

Appendix A2: tensile triangle method

To avoid stress concentration at the sharp corners of the components (e.g. shoulder fillets) or notches, there are different methods to optimize the geometry at such locations. One of the well-known approaches is the tensile triangle method, which is inspired by nature and proposed by Mattheck [90]. This method was applied in design optimization of the micro-samples (refer to chapter 5) [89]¹².

Different steps of this method for optimization of shoulder fillets are illustrated in Fig. A2.1. Starting with a design having a sharp corner (with right angle), three different triangles are mapped to this corner. The first and largest triangle, having two 45° angles, covers the sharp corner as a chamfer. So two design points are identified: point 1 is located on the shoulder (the clamped side), and point 2 is located on the gauge section. The midpoint of the hypotenuse is marked as point 3. A circle with center at point 2 and a radius equal to the distance between points 2 and 3 will cross the gauge section at point 4. The second triangle is defined by point 2, 3, and 4. The midpoint of the hypotenuse is marked as point 5 and the third triangle is defined in similar way as the second one, defining the point 6 locating on the gauge section. After combining the three mentioned triangles as a single area, three lines will remain, numbered from 1 to 3 (Fig. A2.1.b). These lines define the new contour of the corner; however, there are still sharp corners at the interface of the triangles (point 3 and 5), which should be rounded with possibly largest radii tangential to the outer contour of the triangles. Beginning from the midpoint of line 2, the rounding radii are determined. The rounding radii should be tangential to each other at this point, in order to have the largest radii. Now a perpendicular is drawn to the line 2 at its midpoint. The second perpendicular is drawn to the line 1 in the way that point 3 has the same distance d to these two perpendiculars. The intersection point of the two perpendiculars defines the center of the arc, tangential to the lines 1 and 2. The radius of the arc is equal to the distance

¹² This appendix is written mainly based on reference [89]. Readers are referred to this reference for some more details on this topic.

between intersection points of the two perpendiculars and the midpoint of line 2. This arc is the first fillet created by the tensile triangle method. By repeating the procedure for line 2 and 3 in similar way, a fillet can be drawn between these two lines to round the corner at point 5. Furthermore, a third fillet needs to be drawn to round the corner at point 6. Finally, the sharp corner between clamped and gauge sections is substituted with fillets, which are joined together tangentially [89].

To achieve the optimized results, it is needed in some cases to adjust the distance of the point 1 to the initial sharp corner (with right angle) and repeat the procedure. Increasing of this distance leads to the increasing in the fillet radii and therefore a better optimization regarding stress concentration.

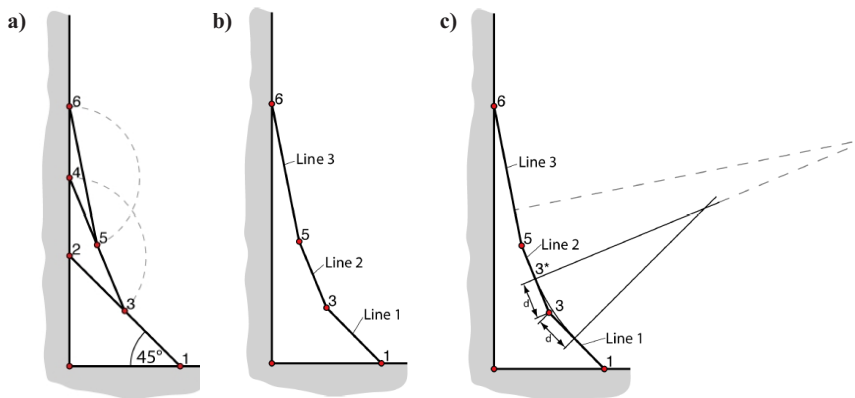


Fig. A2.1: Steps of tensile triangle method for rounding of shoulder corners: a) definition of design points, b) revised contour, c) helping lines for fillet radius [89].

Schriftenreihe des Instituts für Angewandte Materialien

ISSN 2192-9963

Die Bände sind unter www.ksp.kit.edu als PDF frei verfügbar
oder als Druckausgabe bestellbar.

- Band 1 Prachai Norajitra
Divertor Development for a Future Fusion Power Plant. 2011
ISBN 978-3-86644-738-7
- Band 2 Jürgen Prokop
Entwicklung von Spritzgießsonderverfahren zur Herstellung von Mikrobauteilen durch galvanische Replikation. 2011
ISBN 978-3-86644-755-4
- Band 3 Theo Fett
New contributions to R-curves and bridging stresses – Applications of weight functions. 2012
ISBN 978-3-86644-836-0
- Band 4 Jérôme Acker
Einfluss des Alkali/Niob-Verhältnisses und der Kupferdotierung auf das Sinterverhalten, die Strukturbildung und die Mikrostruktur von bleifreier Piezokeramik ($K_{0,5}Na_{0,5}$)NbO₃. 2012
ISBN 978-3-86644-867-4
- Band 5 Holger Schwaab
Nichtlineare Modellierung von Ferroelektrika unter Berücksichtigung der elektrischen Leitfähigkeit. 2012
ISBN 978-3-86644-869-8
- Band 6 Christian Dethloff
Modeling of Helium Bubble Nucleation and Growth in Neutron Irradiated RAFM Steels. 2012
ISBN 978-3-86644-901-5
- Band 7 Jens Reiser
Duktilisierung von Wolfram. Synthese, Analyse und Charakterisierung von Wolframlaminaten aus Wolframfolie. 2012
ISBN 978-3-86644-902-2
- Band 8 Andreas Sedlmayr
Experimental Investigations of Deformation Pathways in Nanowires. 2012
ISBN 978-3-86644-905-3

- Band 9 Matthias Friedrich Funk
Microstructural stability of nanostructured fcc metals during cyclic deformation and fatigue. 2012
ISBN 978-3-86644-918-3
- Band 10 Maximilian Schwenk
**Entwicklung und Validierung eines numerischen Simulationsmodells zur Beschreibung der induktiven Ein- und Zweifrequenzrandschicht-
härtung am Beispiel von vergütetem 42CrMo4.** 2012
ISBN 978-3-86644-929-9
- Band 11 Matthias Merzkirch
**Verformungs- und Schädigungsverhalten der verbundstranggepressten,
federstahldrahtverstärkten Aluminiumlegierung EN AW-6082.** 2012
ISBN 978-3-86644-933-6
- Band 12 Thilo Hammers
**Wärmebehandlung und Recken von verbundstranggepressten
Luftfahrtprofilen.** 2013
ISBN 978-3-86644-947-3
- Band 13 Jochen Lohmiller
**Investigation of deformation mechanisms in nanocrystalline
metals and alloys by in situ synchrotron X-ray diffraction.** 2013
ISBN 978-3-86644-962-6
- Band 14 Simone Schreijäg
**Microstructure and Mechanical Behavior of
Deep Drawing DC04 Steel at Different Length Scales.** 2013
ISBN 978-3-86644-967-1
- Band 15 Zhiming Chen
Modelling the plastic deformation of iron. 2013
ISBN 978-3-86644-968-8
- Band 16 Abdullah Fatih Çetinel
**Oberflächendefektausheilung und Festigkeitssteigerung von nieder-
druckspritzgegossenen Mikrobiegebalken aus Zirkoniumdioxid.** 2013
ISBN 978-3-86644-976-3
- Band 17 Thomas Weber
**Entwicklung und Optimierung von gradierten Wolfram/
EUROFER97-Verbindungen für Divertorkomponenten.** 2013
ISBN 978-3-86644-993-0
- Band 18 Melanie Senn
**Optimale Prozessführung mit merkmalsbasierter
Zustandsverfolgung.** 2013
ISBN 978-3-7315-0004-9

- Band 19 Christian Mennerich
Phase-field modeling of multi-domain evolution in ferromagnetic shape memory alloys and of polycrystalline thin film growth. 2013
ISBN 978-3-7315-0009-4
- Band 20 Spyridon Korres
On-Line Topographic Measurements of Lubricated Metallic Sliding Surfaces. 2013
ISBN 978-3-7315-0017-9
- Band 21 Abhik Narayan Choudhury
Quantitative phase-field model for phase transformations in multi-component alloys. 2013
ISBN 978-3-7315-0020-9
- Band 22 Oliver Ulrich
Isothermes und thermisch-mechanisches Ermüdungsverhalten von Verbundwerkstoffen mit Durchdringungsgefüge (Preform-MMCs). 2013
ISBN 978-3-7315-0024-7
- Band 23 Sofie Burger
High Cycle Fatigue of Al and Cu Thin Films by a Novel High-Throughput Method. 2013
ISBN 978-3-7315-0025-4
- Band 24 Michael Teutsch
Entwicklung von elektrochemisch abgeschiedenem LIGA-Ni-Al für Hochtemperatur-MEMS-Anwendungen. 2013
ISBN 978-3-7315-0026-1
- Band 25 Wolfgang Rheinheimer
Zur Grenzflächenanisotropie von SrTiO₃. 2013
ISBN 978-3-7315-0027-8
- Band 26 Ying Chen
Deformation Behavior of Thin Metallic Wires under Tensile and Torsional Loadings. 2013
ISBN 978-3-7315-0049-0
- Band 27 Sascha Haller
Gestaltfindung: Untersuchungen zur Kraftkegelmethode. 2013
ISBN 978-3-7315-0050-6
- Band 28 Stefan Dietrich
Mechanisches Verhalten von GFK-PUR-Sandwichstrukturen unter quasistatischer und dynamischer Beanspruchung. 2016
ISBN 978-3-7315-0074-2

- Band 29 Gunnar Picht
Einfluss der Korngröße auf ferroelektrische Eigenschaften dotierter $\text{Pb}(\text{Zr}_{1-x}\text{Ti}_x)\text{O}_3$ Materialien. 2013
ISBN 978-3-7315-0106-0
- Band 30 Esther Held
Eigenspannungsanalyse an Schichtverbunden mittels inkrementeller Bohrlochmethode. 2013
ISBN 978-3-7315-0127-5
- Band 31 Pei He
On the structure-property correlation and the evolution of Nanofeatures in 12-13.5% Cr oxide dispersion strengthened ferritic steels. 2014
ISBN 978-3-7315-0141-1
- Band 32 Jan Hoffmann
Ferritische ODS-Stähle – Herstellung, Umformung und Strukturanalyse. 2014
ISBN 978-3-7315-0157-2
- Band 33 Wiebke Sittel
Entwicklung und Optimierung des Diffusionsschweißens von ODS Legierungen. 2014
ISBN 978-3-7315-0182-4
- Band 34 Osama Khalil
Isothermes Kurzzeitermüdungsverhalten der hoch-warmfesten Aluminium-Knetlegierung 2618A (AlCu2Mg1,5Ni). 2014
ISBN 978-3-7315-0208-1
- Band 35 Magalie Huttin
Phase-field modeling of the influence of mechanical stresses on charging and discharging processes in lithium ion batteries. 2014
ISBN 978-3-7315-0213-5
- Band 36 Christoph Hage
Grundlegende Aspekte des 2K-Metallpulverspritzgießens. 2014
ISBN 978-3-7315-0217-3
- Band 37 Bartłomiej Albiński
Instrumentierte Eindringprüfung bei Hochtemperatur für die Charakterisierung bestrahlter Materialien. 2014
ISBN 978-3-7315-0221-0
- Band 38 Tim Feser
Untersuchungen zum Einlaufverhalten binärer alpha-Messinglegierungen unter Ölschmierung in Abhängigkeit des Zinkgehaltes. 2014
ISBN 978-3-7315-0224-1

- Band 39 Jörg Ettrich
Fluid Flow and Heat Transfer in Cellular Solids. 2014
ISBN 978-3-7315-0241-8
- Band 40 Melanie Syha
Microstructure evolution in strontium titanate Investigated by means of grain growth simulations and x-ray diffraction contrast tomography experiments. 2014
ISBN 978-3-7315-0242-5
- Band 41 Thomas Haas
Mechanische Zuverlässigkeit von gedruckten und gasförmig abgeschiedenen Schichten auf flexiblem Substrat. 2014
ISBN 978-3-7315-0250-0
- Band 42 Aron Kneer
Numerische Untersuchung des Wärmeübertragungsverhaltens in unterschiedlichen porösen Medien. 2014
ISBN 978-3-7315-0252-4
- Band 43 Manuel Feuchter
Investigations on Joule heating applications by multiphysical continuum simulations in nanoscale systems. 2014
ISBN 978-3-7315-0261-6
- Band 44 Alexander Vondrous
Grain growth behavior and efficient large scale simulations of recrystallization with the phase-field method. 2014
ISBN 978-3-7315-0280-7
- Band 45 Tobias Kennerknecht
Fatigue of Micro Molded Materials – Aluminum Bronze and Yttria Stabilized Zirconia. 2014
ISBN 978-3-7315-0293-7
- Band 46 Christopher Scherr
Elektrochemisches Verhalten von Lithium-Schwefel-Zellen mit unterschiedlicher Kathodenstruktur. 2015
ISBN 978-3-7315-0296-8
- Band 47 Konstantin Frölich
Der Decal-Prozess zur Herstellung katalysatorbeschichteter Membranen für PEM-Brennstoffzellen. 2015
ISBN 978-3-7315-0334-7
- Band 48 Benedikt Haspel
Werkstoffanalytische Betrachtung der Eigenschaften von mittels neuartiger RTM-Fertigungsprozesse hergestellten glasfaserverstärkten Polymerverbunden. 2015
ISBN 978-3-7315-0337-8

- Band 49 Marco Berghoff
Skalenübergreifende Modellierung und Optimierung vom atomistischen kristallinen Phasenfeldmodell bis zur mesoskopischen Phasenfeldmethode. 2015
ISBN 978-3-7315-0416-0
- Band 50 Michael Selzer
Mechanische und Strömungsmechanische Topologieoptimierung mit der Phasenfeldmethode. 2016
ISBN 978-3-7315-0431-3
- Band 51 Michael Mahler
Entwicklung einer Auswertemethode für bruchmechanische Versuche an kleinen Proben auf der Basis eines Kohäsivzonenmodells. 2016
ISBN 978-3-7315-0441-2
- Band 52 Christoph Bohnert
Numerische Untersuchung des Verformungs- und Bruchverhaltens von einkristallinem Wolfram auf mikroskopischer Ebene. 2016
ISBN 978-3-7315-0444-3
- Band 53 Stefan Guth
Schädigung und Lebensdauer von Nickelbasislegierungen unter thermisch-mechanischer Ermüdungsbeanspruchung bei verschiedenen Phasenlagen. 2016
ISBN 978-3-7315-0445-0
- Band 54 Markus Klinsmann
The Effects of Internal Stress and Lithium Transport on Fracture in Storage Materials in Lithium-Ion Batteries. 2016
ISBN 978-3-7315-0455-9
- Band 55 Thomas Straub
Experimental Investigation of Crack Initiation in Face-Centered Cubic Materials in the High and Very High Cycle Fatigue Regime. 2016
ISBN 978-3-7315-0471-9
- Band 56 Maren Lepple
Kupfer- und Eisenoxide als Konversions-Elektrodenmaterialien für Lithium-Ionen-Batterien: Thermodynamische und Elektrochemische Untersuchungen. 2016
ISBN 978-3-7315-0482-5

- Band 57 Stefan Andreas Slaby
Charakterisierung und Bewertung der Zug- und Ermüdungseigenschaften von Mikropulverspritzgegossenem und konventionell hergestelltem Material. 2017
ISBN 978-3-7315-0484-9
- Band 58 Kumar Ankit
Phase-field modeling of microstructural pattern formation in alloys and geological veins. 2016
ISBN 978-3-7315-0491-7
- Band 59 Kuo Zhang
Characterization and Modeling of the Ratcheting Behavior of the Ferritic-Martensitic Steel P91. 2017
ISBN 978-3-7315-0503-7
- Band 60 Jens Bauer
Mechanische Metamaterialien – Hohe Festigkeit und niedrige Dichte durch Mikroarchitektur und Materialdesign. 2017
ISBN 978-3-7315-0506-8
- Band 61 Fabian Lemke
Untersuchung des Sinterverhaltens von SrTiO₃ unter Berücksichtigung der Defektchemie. 2016
ISBN 978-3-7315-0510-5
- Band 62 Johannes Kümmel
Detaillierte Analyse der Aufbauschneidenbildung bei der Trockenzerspannung von Stahl C45E mit Berücksichtigung des Werkzeugverschleißes. 2016
ISBN 978-3-7315-0518-1
- Band 63 László Hagymási
Modellierung der Stoffübertragung beim Niederdruckcarbonitrieren mit Ammoniak und Acetylen. 2016
ISBN 978-3-7315-0568-6
- Band 64 Reza Eslami
A novel micro-mechanical model for prediction of multiaxial high cycle fatigue at small scales. 2017
ISBN 978-3-7315-0583-9

KARLSRUHER INSTITUT FÜR TECHNOLOGIE (KIT)
SCHRIFTENREIHE DES INSTITUTS FÜR ANGEWANDTE MATERIALIEN

The grain microstructure and damage mechanisms at the grain level are the key factors that influence fatigue of metals at small scales. This is addressed in this work by establishing a new micro-mechanical model for prediction of multiaxial high cycle fatigue (HCF) at a length scale of 5-100 μm . The HCF model considers elasto-plastic behavior of metals at the grain level and microstructural parameters, specifically the grain size and the grain orientation. The HCF model can be applied either as a deterministic failure criterion for individual grains, or as a failure function in probabilistic studies on aggregates of grains. For model verification, the predicted results of the failure function are compared with the observed micro-damage in individual grains of nickel micro-samples. For that the grain size and the grain orientation are measured on the surface of the samples by EBSD, as the main input variables of the failure function. It is shown that the overall predictive power of the HCF model is fairly good. However, some misclassifications occur as some grains are damaged, which are predicted to be safe. Post-fatigue investigations on individual grains reveal in some cases the reasons for those misclassifications.

ISSN 2192-9963
ISBN 978-3-7315-0583-9

